NORTHWESTERN UNIVERSITY

Plasmonic Nanoantennas for Ultrafast Opto-mechanical Sensing

A DISSERTATION

SUBMITTED TO THE GRADUATE SCHOOL

IN PARTIAL FULFILLMENT OF THE REQUIREMENTS

for the degree

DOCTOR OF PHILOSOPHY

Field of Mechanical Engineering

By

Xiang Chen

EVANSTON, ILLINOIS

June 2017

ABSTRACT

Plasmonic Nanoantennas for Ultrafast Opto-mechanical Sensing

Xiang Chen

With the advances in electronics and communication devices over the last several decades, radio-frequency antennas have miniaturized from externally mounted “rabbit ears” on our grandma’s televisions to devices small enough to be concealed within the body of the cellphone itself, corresponding to the carrier frequencies used from on the order of hundreds of MHz to a few GHz. Optical nanoantennas, also called plasmonic nanoantennas, just like their radio-frequency equivalents, efficiently couples the energy of light - an electromagnetic wave oscillating at THz frequencies to a confined region within their feed gap of subwavelength dimension, far beyond the classical diffraction limit. The resonant optical interaction of metallic nanoantennas in their near-field produces strong electromagnetic field confinement, and the gap-width dependent optical scattering intensity opens a regime in sensing applications on the nanoscale. In this thesis, we first explore the optical interaction between two optical antennas- a metallic apertureless near-field optical microscope (a-NSOM) tip and a metal-coated nanomechanical resonator (NMR) over nanoscale distance that vary in a harmonic or transient fashion to demonstrate local measurement of mechanical vibrations in NMRs with nanoscale spatial resolution and nanosecond temporal resolution. In the measurement, a plasmonic nanofocusing element is integrated with the a-NSOM probe for efficient concentration of propagating

surface plasmon polaritons (SPPs) at the apex of probe tip, and efficient confinement of light in the gap between the probe-tip and surface of the NMR. Using this technique, we measured the surface vibrations of suspended metal-coated silicon NMRs with a minimum detectable root-mean-squared displacement sensitivity of 0.3pm/$\sqrt{Hz}$. In addition, the plasmonic aNSOM technique is used for local measurement of motion in a NMR actuated by a harmonic photothermal source to demonstrate all-optical actuation and detection of mechanical vibrations in micro- and nanostructures with sub-wavelength lateral spatial resolution.

Owing to the strong concentration of light at the plasmonic probe, significant heating of the tip and a sample positioned in the optical near-field is expected. We subsequently investigated the local heating produced by the plasmonic nanofocusing probe under steady state conditions using the tip-enhanced Raman approach. This study has implications for exploring the plasmonic nanofocusing probe in heat assisted nanofabrication and fundamental studies of nanoscale heat transport in materials.

In order to push forward the temporal resolution of our technique to picosecond scale, corresponding to the measured frequencies exceeding 100GHz, the pump probe technique is then incorporated with the a-NSOM probe for detection of ultrahigh frequency phonon or acoustic vibrations in isolated nanostructures. This newly developed technique allows us to investigate mechanical vibrations in laterally patterned gold nanodots on glass substrates followed by transient optical excitation. With this technique, quantitative

information on a single nanostructure with high temporal and spatial resolution can be obtained.

Finally, using the optical field concentration of plasmonic nanoantennas as inspiration, a novel class of pillar nanoantennas (P-NAs) is designed, and their plasmon response is utilized for polarization selective detection of complex acoustic phonon vibration modes. This study have important implications in the development of, high speed opto-acoustic modulators, reconfigurable nanomechanical plasmonic metastructures, and ultrafast transducers for detection of acoustic vibrations.

Acknowledgements

First, I want to thank my advisor, Dr. Oluwaseyi Balogun, not only did he guide my research, he also gave me the opportunity and freedom to explore lots of my challenging and unconventional ideas. Through his steadfast support for the project, I could stay motivated and focused on my topic, and for this I am immeasurably grateful. In addition, I would like to thank Prof. Krishnaswamy Sridhar, for providing me access to his femtosecond laser system during the last two years. I would also like to thank the members of my doctoral committee: Prof. Espinosa Horacio and Prof. Cheng Sun, for their time serving on my committee and reviewing my thesis without hesitation. Additional thanks goes to my colleagues and collaborators: Kenan Li, Ankun Yang, Li Zhang, Matt Ford, Phillip Ann, Hong-Cin Liu, Baojie Lu, Jialun Han, Jiadong Deng, Xiangfan Chen, Xiaochen Ren, Dr Tomoda Motonobu, Biqing Dong for willingly offering academic assistance as well as sharing their experience with me. My time spent at Northwestern University has been the best of my life, and I am thankful to my roomies: Siyu Chen, Xiuyuan Xie for enjoying life besides research. Finally, I show my deepest gratitude to my parents for their support and motivation for my thesis. They always want to visit me and travel around US together with me.

Table of Contents

Chapter 1 Introduction

1.1 Background and Motivation

Microelectronics have changed our society and daily life in ways that no one could have fathomed when Gordon Moore published his visionary paper in the late 1960s [1]. For the past five decades, the number of transistors in a single microelectronic chip has exponentially increased by continuous reduction in the feature size. However, the improvement of the product quality and yield is hampered by the fact that nondestructive metrology has not kept pace with the advances in fabrication techniques. As such, there is a critical need for nondestructive techniques capable of dimensional characterization of microelectronic elements and the associated thin film interconnects with critical

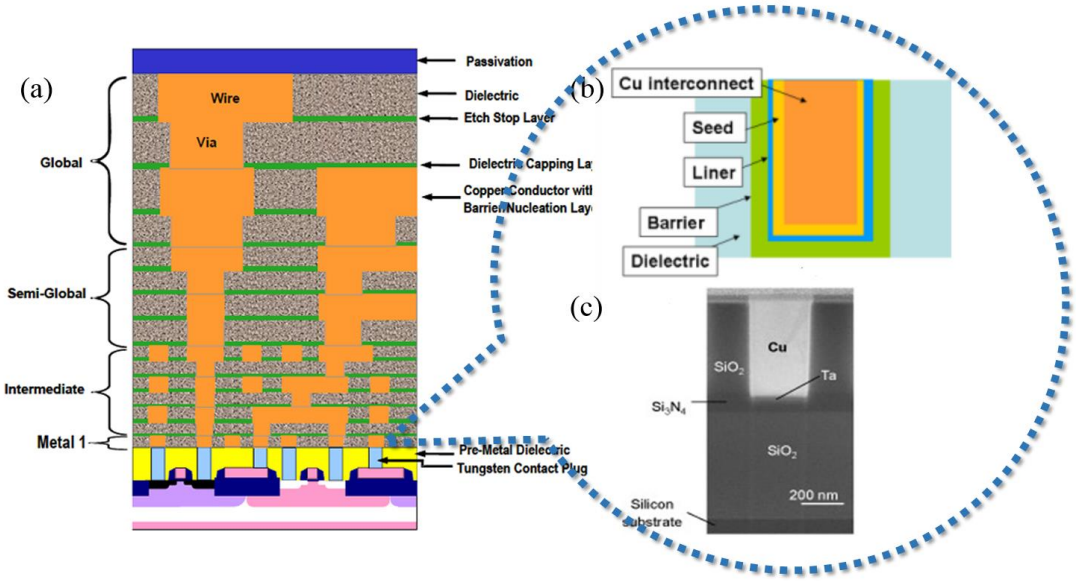

Figure 1.1 (a) Schematic cross-section of copper (orange) interconnect features in current semiconductor chips, (b) detailed schematic cross-section of a single copper interconnect channel, and (c) scanning electron microscopy image of a single cooper interconnect structure.

dimensions in the range of 1-100nm, for identifying integrated circuit failures, such as, delaminations in interconnect layers and nanoscale voids in bonded interfaces. An example of copper interconnect features in current semiconductor chips is shown in Fig 1.1(a) and (b), and a representative scanning electron microscopy image of single copper interconnect channel is shown in Fig 1(c). Copper interconnects are normally fabricated using the dual damascene approach, where inter-level-dielectric(ILD) is first deposited and patterned to define trenches, and then metal is deposited to fill the patterned oxide trenches, and finally polished to the desired thickness. If the interconnect structures are under polished, residual copper will short out the circuitry resulting in defective dies, conversely, over polishing increases the line resistance, negatively impacting the performance of device. As such, it is critical to nondestructively monitor the thickness of copper interconnects. To date, a variety of nondestructive metrology are used to monitor polishing processes including ultrafast photoacoustic (PA) and photothermal (PT) techniques [2, 3] that measure embedded metal thickness, and high resolution scanning probe microscopy (SPM) that measures the relative step height differences between structures such as copper pads and line arrays. For ultrafast PA and PT techniques, using ultrafast laser sources, which produce laser pulses with time durations in the tens to hundreds of femtosecond range, hypersonic acoustic waves are generated and detected. These techniques are well suited for nondestructive testing of sub-micrometer film thickness and investigation of photo-induced coherent phonon vibrations [4-6] in nanostructures. However, in the dense narrow

copper line arrays that are required for current and next generation devices, due to the diffraction limit, the measurement spot size may cover several copper lines/dielectric pairs, leading to spatial averaging of acoustic signals from individual components. For SPM techniques, the resolution is not limited by the classic diffraction theory, only by the size of the probe-sample interaction volume, which can be as small as few nanometers. So far, a variety of new techniques are integrated with SPM technique, such as, atomic force spectroscopy (AFS) [7, 8], atomic force acoustic microscopy (AFAM) [9, 10], ultrasonic force microscopy (UFM) [11-13], near-field scanning optical microscopy (NSOM) [14-16]. providing not only the topography of the samples, but also their optical, magnetic, electrical and mechanical properties. Even though the SPM based techniques are able to take measurements with sub-100nm lateral spatial resolution, the temporal resolution is still limited, making it difficult to obtain the dynamic information of the samples.

Recent progress in plasmonics has opened a new gateway to reduce the cross sections of propagating optical modes far beyond the diffraction limit, to efficiently deliver optical energy to nanoscale objects, and to concentrate this energy within spatial regions with dimensions as small as a few nanometers [17-19]. Long before scientists have pursued interest in investigation of light interaction with nanometer sized metallic objects, artists in ancient Rome leveraged the resonant absorption and scattering properties of gold (Au) and silver (Ag) nanoparticles embedded in glass to generate brilliant colors in their artefacts and artwork such as, the Roman Lycurgus cup that appears green or red when viewed (Fig

1.2)[20]. Beyond aesthetics, systematic study of modern plamonics dates back in the works of Gustav Mie (1980) and Rufus Ritchie (1957) on small metal particles and flat metal surfaces. Today's application of plasmonics include the utilization of metal nanostructures

Figure 1.2 Ancient Roman Lycurgus cups

used as nano-anttenna optical probes in biology and chemistry [21-23], implementation of strong near-field enhancement in tip enhanced Raman spectroscopy (TERS) [24] or Surface enhanced Raman Spectroscopy (SERS) [25] and the development of metamaterial to manipulate light propagation [26]. The central feature of nanoplasmonics is the confinement of optical fields into deep subwavelength volumes and the most popular geometries are antenna based structures, including bowtie nanoantennas [27], nanorod dimer [28] and pillar bowtie nanoantennas [29], that exploit the resonant enhancement of charge density oscillations to funnel freely propagating electromagnetic waves into

nanometer-sized gap regions. The optical field enhancements by greater than three order of magnitude can be engineered in the gap region and these sub-diffraction “hot spots” are particularly useful in the field of nonlinear optics. The basic theory behind the antennas effect can be formulated by coupling point dipoles, in which the plasmon resonance of individual dipolar particle can be converted to a coupled mode by placing a second particle nearby. Due to evanescently decaying field around each of these particles, the coupled dipole system is very sensitive to the gap distance change perturbed by motion of each particle. Furthermore, from a theoretical point of view, coupled dipole model can be used to describe the electromagnetic interaction of a metallic probe-tip and a sample surface within the near-field interaction region in near-field scanning optical microscope (NSOM) technique.

In this thesis, we investigate coupled dipoles system perturbed by displacing two plasmonic elements (one is the aNSOM probe and another is the metallic sample) in each other’s near field, where, 1. the probe and sample vibrate in harmonic motion, 2. the probe vibrates in harmonic motion and the sample exhibits ring down vibrations, and 3. the probe tip is in contact with a sample vibrating in frequencies in the tens of GHz range. The main achievement of this work is the development and characterization of an ultrafast aNSOM approach that allows for detection of ultrafast laser generated phonon vibrations with nanoscale lateral spatial resolution and picosecond time resolution. This newly developed technique: Piecosecond Ultrasonic Near-field Optical Microscopy (PUNOM), will open a

new avenue for reliable nondestructive metrology for failure analysis in nanoelectronics, quantitative investisgation of mechanical properties of individual nanostructured thin film and acoustic imaging of buried nanoscale defects and voids. On a broader scope, the ability to detect acoustic waves with a high temporal resolution and high spatial resolution using the PUNOM technique can provide a platform for investigation of heat transport and coherent phonons in confined geometries.

To date, the SPM based techniques have commonly employed single point probes for serial detection, which is generally slow in acquiring images of physical quantities. However, on-line monitoring of copper interconnect deposition process requires fast positioning a probe on copper interconnect with width ranging from less than 100nm to several micrometers. Recent advances in scanning probe microscopy has exhibited extreme imaging speed without loss of resolution. For example, with the FastScan system (Bruker), it is possible to achieve immediate atomic force microscopy images with the expected high resolution and survey a sample scanning at >125Hz to find the region of interest. Unfortunately, the scanning probe used in FastScan system is made of diamond, while metallic probes made of gold or silver used in most NSOM system are easy to get blunted due to fast scanning speed. An alternative approach to improving the imaging speed is to employ an array of plasmonic nanoantennas placed in the near field region of the sample surface, where each individual nanoantenna will serve as a "hot spot" to capture the local properties of the sample. The plasmonic nanoantenna array is especially useful for optical trapping and

manipulation in the biology sciences [30-32], where it has become a ubiquitous tool to study single-molecule biophysical systems, mechanical properties of DNA, and single viruses, bacteria, and cells. In the last chapter of this thesis, I will describe my recent efforts to develop arrays of plasmonic nanoantennas and the investigation of their ultrafast acoustic vibration properties. Incorporating ultrafast PA and PT technique with plasmonic nanoantenna arrays, where individual nanoantenna serves a point sensor and the whole arrays serves as a sensor array, will allow for tracking dynamic motion at multiple points on a sample surface using confined optical cavities.

1.2 Photoacoustic Materials Characterization and Imaging

Photoacoustic (PA) methods are high sensitivity, non-contact inspection techniques used for materials characterization and nondestructive evaluation [33-35]. These methods rely on the thermoelastic generation of elastic waves by a laser source. Figure 1.3 shows a schematic of the processes involved. A pulsed excitation laser locally illuminates the surface of a material, where the laser energy is absorbed leading to localized heating. The heating produced by the laser creates a local and transient thermoelastic expansion and the resulting confined stresses radiate energy into material as coherent elastic waves. These elastic waves (also called acoustic waves) propagate as bulk longitudinal and shear waves in an infinite solid. In finite solids, the presence of boundaries lead to coupling of the longitudinal and shear waves to wave-guide modes (Lamb modes) and surface acoustic

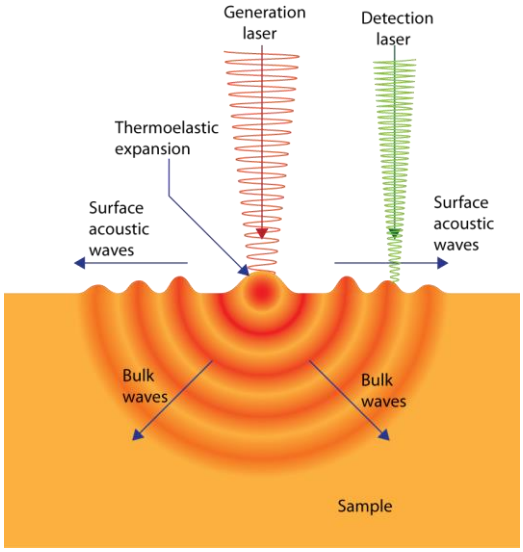

Figure 1.3 Schematic of pulsed laser generation and detection of acoustic waves

waves. As the elastic waves propagate through the specimen, their amplitude decrease due to material attenuation, scattering from structural or material inhomegeneities in the specimen, and geometric spreading. Furthermore, the propagation velocity of these waves is material dependent, being directly related to the elastic properties and density. As such, measurement of the amplitude and velocity of the laser generated elastic waves provides a means for characterizing the elastic properties, microstructure, and composition of materials. In addition, the interaction of elastic waves with surface and sub-surface objects in a material creates diffracted waves. Mapping the spatial variation of the diffracted field provides a means to reconstruct the shape and location of the objects. In PA methods, elastic waves are detected using diffraction or deflection based optical probes. In interferometric

methods, a probe beam reflected from a vibrating sample surface is phase-modulated by the surface displacement. The phase-modulated probe beam is then demodulated by interfering with a reference beam, which converts the phase modulation to an intensity change that can be recorded by a photodetector. In optical lever approaches, a position-sensitive photodetector is used to detect the rotation of a probe beam reflected by a moving surface. The lateral spatial resolution of PA technique, which is dictated by the spot size of light, is limited by diffraction to half of the probe wavelength.

1.3 Picosecond Ultrasonics-Ultrafast PA Method

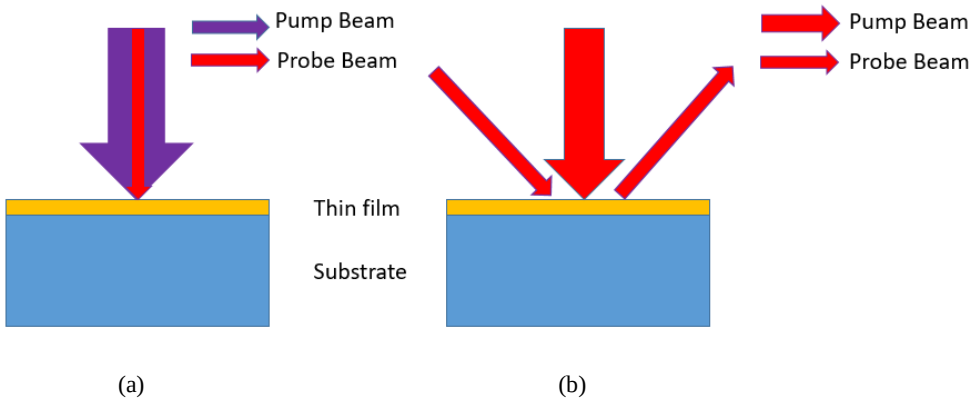

Figure 1.4 Generation and detection of bulk acoustic waves using the picosecond ultrasonic technique

Picosecond ultrasonics technique, which is also referred to as pump probe technique, is a type of laser based PA method, where ultrahigh frequency acoustic waves are generated by ultrafast laser pulses with time duration in the tens to hundreds of femtoseconds range. It is a common tool used to measure the transient thermal and acoustic properties of different

materials, such as metal, semiconductors, nano-particles and thin films with sub-micron thickness on time scales not easily accessible by other means. Picosecond ultrasonics is a rather popular technique for numerous studies in solid state physics and microelectronics. In this technique, the excitation laser creates a bulk compressional (or longitudinal wave) in the film, which reflects from the film-substrate interface and is detected by reflecting a time-delayed probe laser pulse at the free surface of the film, and measuring the intensity change of the reflected probe. The intensity change results from strain induced modulation of the optical reflectivity of the sample surface associated with the acoustic wave arrival. The time evolution of the sample surface displacement or strain is recorded at different time delays between the pump and probe pulse lasers. In order to separate the probe pulse from the pump pulse, two methods are used: frequency separation (Fig 1.4 (a)) where the wavelength of the probe pulse is different from that of the pump pulse, and spatial separation (Fig 1.4 (b)) where the collection angle of the probe pulse suppresses the receiving of the pump pulse. Figure 1.5 shows a representative waveform for picosecond ultrasonic response in approximately 30nm aluminum film on silicon substrate. Before the pump laser pulse arrives at the specimen surface, the probe laser pulse measures no relative change in the optical reflectivity. When the path length of pump and probe laser pulses is exactly the same (corresponding to 0 time delay), both laser pulses hit the specimen at the same time and an initial reflectivity jump is observed. This reflectivity jump is caused by the increased temperature and strain. Superimposed on the smooth decay of the reflectivity,

which is caused by the slowly decreasing temperature in the thin film, are acoustic wave reflections that induced dynamic strains close to the sample surface that perturb the surface optical reflectivity. These vibrations are caused by thermoelasticeffects and the vibration frequency can be used to calculate the film thickness if the Young's Modulus of the sample is known. The short wavelength of the generated acoustic pulses is ideal for characterization of nanostructured thin film materials, however, the spot size of the probe laser pulse is limited by diffraction limit when using a conventional dielectric lens. The large probe spot size makes it difficult to make measurements on single nanostructures or to resolve nanoscale lateral variations in the acoustic wave response within the film. The latter may result from scattering from buried nanoscale interfaces or defects.

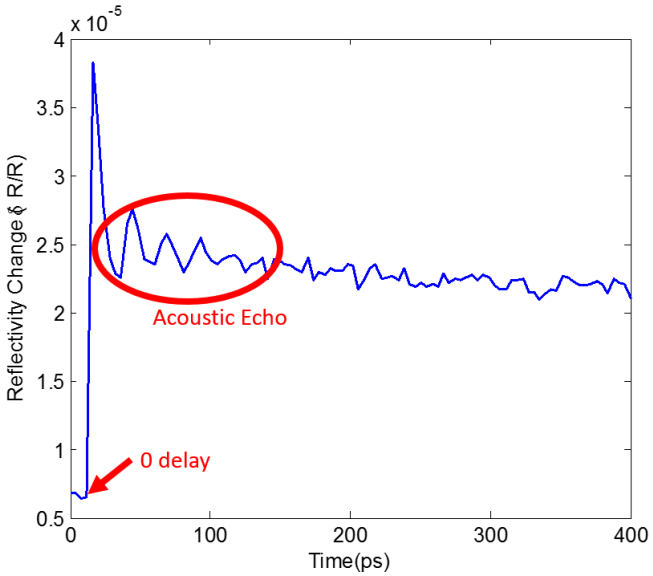

Figure 1.5 Experimental waveform showing acoustic resonance excited by an ultrafast laser in 30nm aluminum thin film on silicon substrate.

1.4 Near-field Scanning Optical Microscopy

Traditional optics operate in the far-field, using a system of optical elements such as mirrors or lenses that collect light scattered from an objective and creating an image of the object on a viewing device. If the object is smaller than the light wavelength, the diffraction angle can be pretty broad, resulting in a small portion of rays reaching the plane of viewing device. Even if the far field rays are all collected, the spatial resolution or smallest distinguishable distance between two features that can be obtained with traditional light microscopes is still limited by the Rayleigh criterion, depending on the light wavelength (λ) and numerical aperture (NA) of the collection optic according to $\Delta x = 1.22\lambda/NA$. For example, using a visible light source with $\lambda = 532nm$ and a microscope objective lens with NA = 0.65, a spot size of approximately 800 nm can be achieved. In order to overcome the diffraction limit on the spatial resolution, collection of the evanescent components of light in the near-field is necessary since these evanescent components decay fast around the sample surface. As such, a variety of near-field optical techniques have been developed, that fall under two broad categories namely, aperture type NSOM and apertureless NSOM (a-NSOM). The illustrations in figure 1.6 represent basic configurations of aperture type NSOM and apertureless NSOM. In aperture NSOM, a small aperture, such as an Al coated fiber tip is scanned in close proximity to the sample surface and resolutions of 50-100nm can be achieved. Because of the small aperture, only a small portion of light can be collected, yielding a low throughput. In apertureless NSOM, a very sharp sub-diffraction

limited tip is placed on sample surface with nanometer gap distance. As sketched in figure

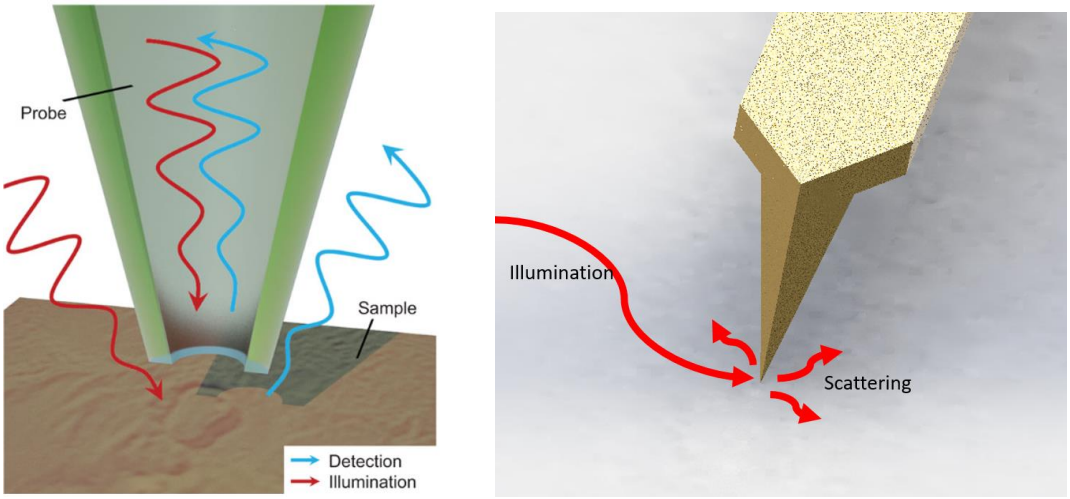

(a) (b)

Figure 1.6 Illustration figures of (a) aperture NSOM and (b) apertureless NSOM

1.6 (b), an illuminating beam is focused onto the probing tip. The usually chosen metallic tip acts as an antenna, concentrating the incident light at the apex of the tip. As such, silver and gold are two commonly used material to fabricate a-NSOM probe-tip, since they have resonant frequencies in the visible or infrared wavelength. The scattered light from the probe-tip and sample interaction is used to create an optical image of the sample. The spatial resolution of a-NSOM is not dependent on the wavelength of the illumination light; instead, it is determined by the size of the probe tip which can be as small as few nanometers. The illumination of the scattering probe tip, however, causes a large background signal by scattering from both the probe shaft and the sample surface. The background can be suppressed by modulating the tip at a fixed frequency and demodulating

the scattered intensity at harmonics of the frequency in the far-field. The latter arises due to the nonlinear dependence of the scattering intensity with the probe-tip separation.

1.5 Plasmonic Nanofocusing Approach

Efficient delivery and concentration of optical energy within spatial regions with dimensions as small as a few nanometers has been achieved in recent years [36]. These development largely rely on the use of surface plasmon polaritons (SPPs) – electromagnetic waves formed by collective oscillations of free carriers at the surface of a metal. A special phenomenon occurs when SPPs with a particular polarization propagate along tapered structures. Both the phase and group velocities of SPPs gradually vanish toward the apex, resulting in adiabatic energy concentration and a strong local field enhancement [37, 38]. Despite some constraints on coupling efficiency of far field light to propagation SPPs and energy dissipation through SPPs propagation to the apex, such adiabatic nanofocusing technique allows for true three-dimensional focusing into an excitation volume as smaller as few nanometers, far beyond the diffraction limit when using a conventional dielectric lens. Integration of the plasmonic nanofocusing approach with scanning probe microscopy (SPM) has inspired a variety of novel applications in nano-optics. For example, Diyar et al. reported on using grating-coupled adiabatically-focused apertureless near-field scanning optical microscopy (a-NSOM) for background-free imaging of single metallic nanoparticles with deep subwavelength resolution [39]. The

same group then studied photoelectron emission from the apex of a sharp gold nano-taper illuminated via grating coupling and demonstrated an increase of electron yield over that of direct apex illumination [40]. Samuel et al. extended the application of adiabatic plasmon nanofocusing for tip-enhanced Raman scattering (TERS) to study surface molecules with enhanced contrast [41]. They also coupled femtosecond laser pulses with a nanofocusing probe to demonstrate simultaneous nanometer spatial confinement and femtosecond temporal control of an optical excitation [42]. Here we present our plasmonic nanofocusing approach that uses a metallized AFM probe for efficient confinement of light to a nanoscale spot size at the probe-tip. Figure 1.7 shows a basic illustration of the technique as it pertains to acoustic wave or vibration detection. In the figure, a silver coated AFM probe is used. The probe laser is used to excite propagating SPPs on the shaft of an AFM probe through a diffraction grating on the tapered facets of the probe. The SPPs propagate adiabatically towards the probe tip where they are localized and converted to localized plasmons (LSPs). For a fixed frequency, the wavelength of an SPP is smaller than that of light in free space, and when an SPP is coupled to an adiabatically tapered waveguide (i.e., the waveguide curvature is slow as compared to the SPP wavelength) like

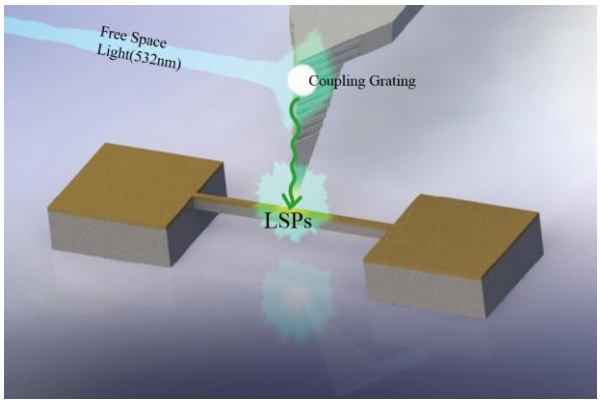

(a)

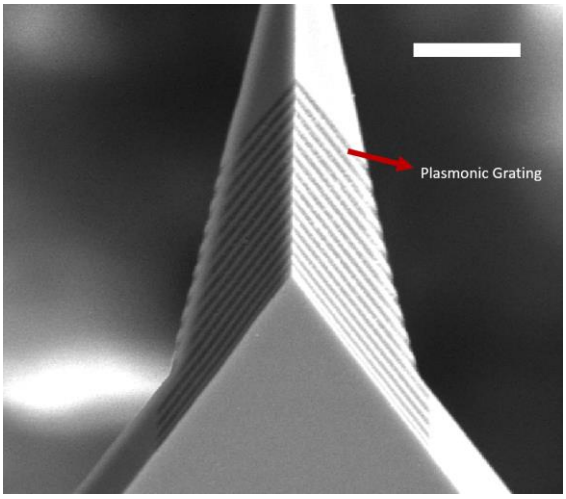

(b)

Figure 1.7 (a) Schematic of plasmonic nanofocusing probe for transduction of local surface displacements (b) SEM image of a plasmonic nanofocusing probe. The scale bar is $5\mu m$

on the facets of an AFM probe, the SPP propagate freely towards the probe-tip with minimal reflections, forming a highly localized optical source. The decay length of the probe-tip SPPs in the dielectric medium (air) is shorter than the light wavelength. As such, to couple the SPPs to the sample, the separation distance between the probe-tip and sample has to be maintained within the decay length.

1.6 Overview of Dissertation

Recent advances in plasmonics have enabled unprecedented control of light matter interaction, making it possible to concentrate optical energy within spatial regions with dimensions as small as a few nanometers. For example, the resonant interaction of two optically interacting metal particles with nanometer spacing couples far field radiation to localized plasmon modes. Changes in the gap width between two particles due to the acoustic wave or mechanical vibration induced displacement, or changes in the sample dielectric properties due to thermal or mechanical strain, lead to modulation in the intensity or the plasmon resonance of the scattered light measured in the far-field. Based on these approaches, we investigate the near-field optical interaction in tip-sample system, enabling the detection of mechanical motion in nanomechanical resonator and acoustic wave measurements on individual nanostructures. On the other hand, rapid progress in picosecond ultrasonics techniques opens a new gateway to elucidate the scenario of hypersonic acoustic waves propagation in nanostructures with ultrahigh temporal resolution. The next part of this work incorporates an a-NSOM probe into picosecond ultrasonic techniques for detection of ultrafast laser generated ultrafast vibrations in nanostructures with frequency components exceeding 100GHz with nanoscale spatial resolution and picosecond time resolution, which will open a new avenue for reliable nondestructive metrology for failure analysis in nanoelectronics, quantitatively investisgation of mechanical properties of individual nanostructured thin film and acoustic

imaging of buried nanoscale defects and voids. Finally, I report of the development of plasmonic nanoantenna arrays, where each element serves as a nanometer sized optical sensor. This plasmonic antenna array can be further developed as ultrafast transducers for investigation of physical scenario such as heat transport and phonon propagation in nanostructures with extremely high spatial and temporal resolution.

In chapter 2, a simple spring-mass-damper model is employed to investigate the interaction of two dipoles perturbed by displacing two plasmonic elements in each other's near field. Using this simple analytical model, a relationship between the plasmon resonance and the spacing between the plasmonic elements is established that provides a fundamental framework for the work done in this thesis.

In chapter 3, we explore apertureless near-field optical microscopy (a-NSOM) to demonstrate local measurement of mechanical vibrations in an isolated metal-coated silicon nanowire with high spatial and temporal resolution. The experimental illustration are shown in figure 1.8. We demonstrate spatial-temporal measurement of multiple flexural vibration modes in two orthogonal directions in the nanowire. Measurement of these modes would allow for characterization of the elastic modulus along the orthogonal crystallographic directions and processing induced residual stress.

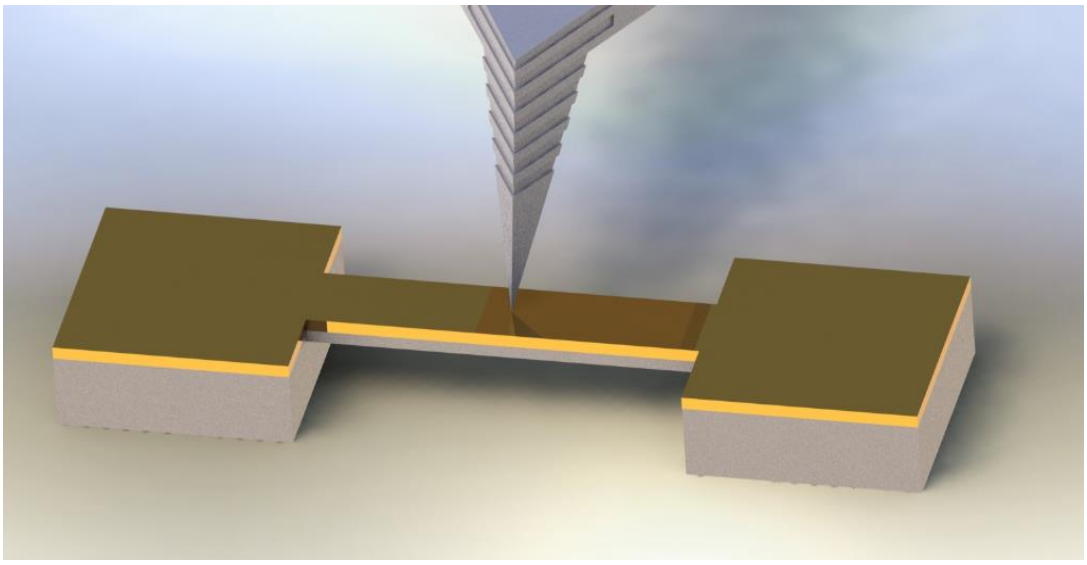

Figure 1.8 Apertureless near-field optical microscopy experiment.

Chapter 4 explores scanning probe microscopy (SPM) to demonstrate local measurement of motion in an isolated, metal-coated silicon nanomechanical resonator actuated by a harmonic photothermal source. We present a heterodyne demodulation approach to suppress unwanted background scattering and resolve the mode shapes of the first and second eigen bending modes of the resonator. The measurement technique allows for an all-optical actuation and detection of mechanical vibrations in micro- and nanostructures with sub-wavelength lateral spatial resolution. Furthermore, the measurement technique allows for actuation of the resonator over a broad frequency range, and measurement of the steady state displacement with high frequency resolution and signal-to-noise ratio.

In previous chapters, the nanofocusing scheme are explored in near-field transduction of

nanomechanical vibrations. Owing to the strong concentration of light at the probe, significant heating of the tip and a sample positioned in the optical near-field is expected. In chapter 5, we investigate the local heating produced by the plasmonic nanofocusing probe under steady state conditions using the tip-enhanced Raman approach. In addition, a finite element model is explored to study the coupling of free propagating light to LSPs and to predict the temperature rise expected in a half space heated by the local optical probe. This study has implications for exploring the plasmonic nanofocusing probe in heat assisted nanofabrication and fundamental studies of nanoscale heat transport in materials.

Chapter 6 develops a new technique, in which an aNSOM probe is incorporated with ultrafast time-resolved pump-probe technique. The newly developed technique allows us to investigate mechanical vibrations in laterally patterned gold nanodots on glass substrates resulting from transient optical excitation by a femtosecond pump laser. This technique provides unprecedented access to short spatial scales (nanometers) and time scales (picoseconds) to enable the investigation of optomechanical interactions, particularly in plasmonic structures at the nanoscale, and the potential to advance the development of coupled plasmonic and phononic devices in the future.

In chapter 7, a novel class of pillar nanoantennas (P-NAs) is designed, and their plasmonic response is utilized to selectively detect complex phonon modes below the diffraction limit

though the coupling mechanism between plasmon and phonon modes.

This work can be exploited for applications such as ultratrace chemical detection, ultrafast transducers and ultrasensitive optical detectors.

Finally, Chapter 8 provides a summary of the technological developments achieved thorugh this project. In addition, some suggestions are provided for future research directions that can be pursued leveraging the achievements of this project

Chapter 2 Theory of Plasmon Based Sensing

The study of optical phenomena related to the resonant electromagnetic response of metal nanostructures is termed plasmonics. At the fundamental level, most of the physics of the interaction of light with metal subwavelength nanostructures is based on the frequency dependence of the metal's complex dielectric function. In this chapter, I will begin with a classic model: Lorentz-Drude model, which gives rise to the fundamental optical properties of metals and dielectrics. Then I will investigate important solutions of Maxwell's equations for, 1. the electromagnetic interaction at a plane metal-dielectric interface, and 2. noble metal nanostructures that exhibit resonant behavior. Finally, I will develop a coupled dipole model to represent light interaction between two nanosized metallic particles separated by a distance which is much smaller than the wavelength of light, and reveal how the coupled plasmonic resonance changes with respect to the particle size and their separating distance. This analytical model is also suitable for describing the optical interaction between a metallic probe and a planar sample surface since the sample surface can be treated as an image dipole.

2.1 Basics

The interaction of metals with electromagnetic fields can be completely described within the framework of the classical Maxwell's equations, with express the relationship between the electric (**E**) and the magnetic (**H**) fields:

$$\nabla \cdot \mathbf{D} = \rho \tag{2.1}$$

$$\nabla \cdot \mathbf{B} = 0 \tag{2.2}$$

$$\nabla \times \mathbf{E} = -\partial \mathbf{B}/\partial t \tag{2.3}$$

$$\nabla \times \mathbf{H} = \mathbf{J} + \partial \mathbf{D}/\partial t \tag{2.4}$$

Where **D** is the electric displacement, **B** is magnetic induction, **J** is the current density and ρ is the external charge density, respectively. The constitutive relation provides a relationship between the electric and magnetic fields and the electric displacement (**D**) and magnetic induction (**B**):

$$\mathbf{D} = \epsilon_0 \mathbf{E} + \mathbf{P} \tag{2.5}$$

$$\mathbf{B} = \mu \mathbf{H} \tag{2.6}$$

Where $\varepsilon = \varepsilon_0 \varepsilon_r$ and $\mu = \mu_0 \mu_r$ are the electric permittivity and magnetic permeability of the material, respectively. ε_0 is the vacuum permittivity, μ_0 is the vacuum permeability and ε_r , μ_r are the material-dependent relative permittivity and permeability. The polarization of the medium **P** is given by $\mathbf{P} = \epsilon_0 \chi_e \mathbf{E}$ where χ_e is the dielectric susceptibility of the medium.

2.2 Lorentz-Drude Model for light-Matter Interaction

The optical properties of subwavelength metal nanostructures can be described over a large frequency range using the Lorentz-Drude model [43] where a polarizable atom containing a single negative electron bound to a positive nucleus. This electron starts to oscillate in

the presence of an electromagnetic field $\mathbf{E}(t) = \mathbf{E}_0 \exp(-i\omega t)$. The electron is displaced from its equilibrium position via the applied electric field, which gives rise to the force $\mathbf{F} = -q\mathbf{E}_0$. As the external excitation field oscillates with a frequency ω, the oscillatory response of the electron induces an atomic dipole that can be modeled as a simple spring-mass-damper system with expression as,

$$\ddot{x} + \gamma\dot{x} + \omega_0^2 x = -\frac{q}{m_e}\mathbf{E}_0 \tag{2.7}$$

Where m_e is the effective mass of the bound electron, γ is a damping constant and ω_0^2 is the resonant frequency. The steady displacement amplitude is given by,

$$x = \frac{(\frac{q}{m_e})\mathbf{E}_0}{\omega^2 - \omega_0^2 - i\omega\gamma} \tag{2.8}$$

The electronic dipole moment is related to the displacement amplitude by $\mathbf{p} = qx$. Suppose there are N electrons, the cumulative effect of all the individual dipoles results in a microscopic polarization P given by,

$$\mathbf{P} = N\mathbf{p} = \frac{Nq^2}{m_e(\omega^2 - \omega_0^2 - i\omega\gamma)}\mathbf{E}_0 \tag{2.9}$$

The relation between the dielectric constant ε and the macroscopic polarization $\mathbf{P}$ can be expressed as,

$$\varepsilon = 1 + \frac{|\mathbf{P}|}{\varepsilon_0|\mathbf{E}|} \tag{2.10}$$

Taking into account the solution **P** thus yields the complex, frequency dependent optical properties

$$\varepsilon(\omega) = \varepsilon' + \varepsilon'' \tag{2.11}$$

$$\varepsilon'(\omega) = 1 + \frac{\omega_p^2(\omega^2 - \omega_0^2)}{(\omega^2 - \omega_0^2)^2 + \omega^2\gamma^2} \tag{2.12}$$

$$\varepsilon''(\omega) = \frac{\omega_p^2\omega\gamma}{(\omega^2 - \omega_0^2)^2 + \omega^2\gamma^2} \tag{2.13}$$

Where $\omega_p = \sqrt{NNq^2/(\varepsilon_0 m_e)}$ is the volume plasma frequency. The resonant frequency, plasma frequency, and damping constant are all material dependent parameters that control the optical response.

In metals, the spring-mass-damper equation contains no restoring force since free electrons are not bound to the nucleus. In this case, the resonant frequency ω_0^2 is zero, corresponding to a mass-damper system. Setting ω_0^2 to zero in equation (2.12) and (2.13), yields the Drude model for the dielectric constants given by,

$$\varepsilon'(\omega) = 1 - \frac{\omega_p^2}{\omega^2 + \gamma^2} \tag{2.14}$$

$$\varepsilon''(\omega) = \frac{\omega_p^2\gamma}{\omega(\omega^2 + \gamma^2)} \tag{2.15}$$

Here the damping term is proportional to $\gamma = v_F/l$, where v_F is the Fermi velocity and l is the electrons mean free path between scattering events.

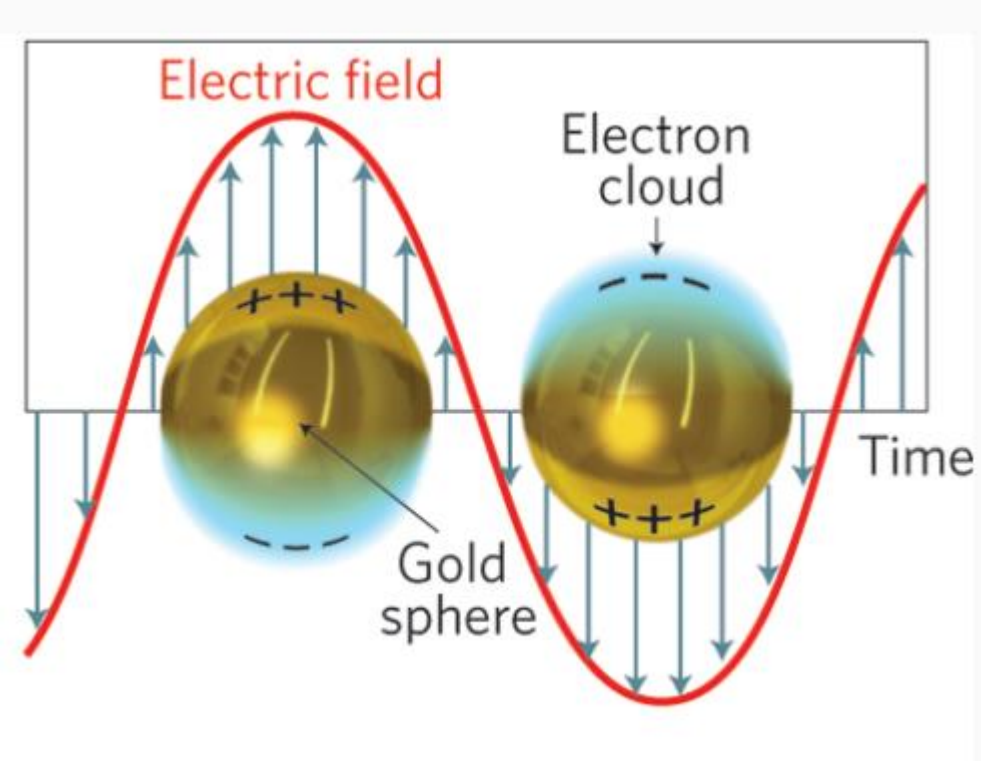

Figure 2.1 Localized surface plasmon resonances

2.3 Localized Surface Plasmon Resonances (LSPRs)

Localized surface plasmons (LSPs), also known as surface plasmons on metal nanoparticles are non-propagating plasmon excitations on metallic nanostructures. Qualitatively, LSPs can be analyzed by Lorentz-Drude Model, where the free-electron gas in a metallic particle is perturbed by an incident electric field. For subwavelength particles ($d \ll \lambda$), the incident field of wavelength λ fully penetrates the nanoparticle and causes a uniform displacement of the negative electron gas from the positive nucleus, thereby establishing a quasi-static dipole moment in the particles (Figure 2.1). The quantitative analysis of LSPRs can be performed in case of a small spherical particle of radius a

illuminated by a plane wave electric field described $\mathbf{E} = \mathbf{E_0}\exp(i\omega t)$. The surrounding medium is assumed to be isotropic with dielectric constant ε_d, and the optical properties of the metal particle is described by the complex dielectric constat ε_m. For this case, Eqns. 2.1 to 2.4 reduces to the Laplace equation: $\nabla^2\Phi = 0$, where Φ is a scalar potential related to the electric field distribution by, $E = -\nabla\Phi$. The solution to the Laplace's equation yields the electric field outside the particle, which consists of the incident and scattered wave components described by the equation below in spherical coordinates,

$$E(r,\theta) = E_0(cos\theta\hat{e}_r - sin\theta\hat{e}_\theta) + \frac{\varepsilon_m(\omega)-\varepsilon_d}{\varepsilon_m(\omega)+2\varepsilon_d}\frac{a^3}{r^3}E_0(2cos\theta\hat{e}_r + sin\theta\hat{e}_\theta) \qquad (2.16)$$

where $\hat{e}_r$ and $\hat{e}_\theta$ are unit vectors along the radial and azimuthal directions. The first term in the equation represents the incident field and the second term is the scattered field, which resembles the electric field of a point dipole with a dipole moment of [43],

$$\mathbf{P} = \varepsilon_0\varepsilon_d\alpha\mathbf{E_0} \qquad (2.17)$$

and the term α represents the frequency dependent polarizability given by,

$$\alpha(\omega) = 4\pi a^3\frac{\varepsilon_m(\omega)-\varepsilon_d}{\varepsilon_m(\omega)+2\varepsilon_d} \qquad (2.18)$$

The real part of the polarizability has a maximum when the real part of $\varepsilon_m(\omega)$ is equal to -2ε_d, representing the localized surface plasmon resonance condition, and it has strong implications on the amplitude of the electric field scattered from and absorbed by the polarized particle. Two important quantities that characterize the optical properties of a plasmonic particle are the scattering and absorption cross sections, which describe the rate at which optical energy is scattered or absorbed by the particle. The amplitude of the

scattered field from the particle is related to the scattering cross-section. Suppose the total power of the absorbed power P_{abs} and scattered power P_{scat} by the particle are given by,

$$P_{abs} = \iint_{\partial V} Re|E_{tot} \times H^*{}_{tot}| \,.\, ds \tag{2.19}$$

$$P_{scat} = \iint_{\partial V} Re|E_s \times H^*{}_s| \,.\, d \tag{2.20}$$

In the above expressions *Re* represents the real part, E_{tot} and $H_{tot}$are the total electric and magnetic fields, E_s and H_s are the scattered electric and magnetic fields, and the integrals are taken over a surface s enclosing a volume ∂V around the particle. The absorption cross sections is given by the ratio of P_{scat} and the incident power I_o,

$$\frac{P_{abs}}{I_0} = \sigma_{abs} = \frac{k}{\varepsilon_0} \mathrm{Im}\big(\alpha(\omega)\big) \tag{2.21}$$

and the scattering cross section is given bym

$$\frac{P_{scat}}{I_0} = \sigma_{scatt} = \frac{k^4}{6\pi\varepsilon_0^2} |\alpha(\omega)| \tag{2.22}$$

In these expressions *k* is the wavenumber. The absorption and scattering cross sections are maximum when the localized surface plasmon resonance condition is satisfied.

2.4 Coupled Dipole Model

In section 2.3, the electromagnetic wave interaction with a single particle is formulated by describing the scattered field from the particle as a dipole. Consider the interaction of an

incident electromagnetic wave with two metal particles. In this case, we will treat these particles as point dipoles separated by a distance d that is much smaller than the wavelength of the incident wave. The total dipole moment of the system of particles is equal to the vectorial sum of the dipole moments of each particle,

$$\mathbf{P} = \mathbf{P_1} + \mathbf{P_2} \tag{2.23}$$

Following the formulation in section 2.3, the dipole moment for each particle is given by,

$$\mathbf{P} = \boldsymbol{\alpha} \cdot \mathbf{E} \tag{2.24}$$

Where $\boldsymbol{\alpha}$ is the 3×3 polarizability tensor,. The radiated electric field from a point dipole at position $\mathbf{r_0}$ can obtained through the Green dyadic approach [43], and is given by,

$$\mathbf{E}_{dipole}(\mathbf{r}) = \frac{k^2}{4\pi\varepsilon_0 r} e^{ikr} \left((\hat{\boldsymbol{r}} \times \mathbf{p}) \times \hat{\boldsymbol{r}} + (3\hat{\boldsymbol{r}}(\hat{\boldsymbol{r}} \cdot \mathbf{p}) - \mathbf{p}) \left(\frac{1}{(kr)^2} - \frac{i}{kr} \right) \right) \tag{2.25}$$

In free space, where $\mathrm{r} = |\mathbf{r} - \mathbf{r_0}|$ and $k = \omega/\mathrm{c}$, and c wave speed. Within the near-field, a distance from each dipole that is much smaller than the wavelength, the dipole field reduces to,

$$\boldsymbol{E}_{dipole} = \frac{\boldsymbol{p}}{2\pi\varepsilon_0 d^3} \tag{2.26}$$

For each particle, an applied electric field produces an induced oscillatory dipole that can be modeled as a simple spring-mass-damper system according to Lorentz-Drude Model i.e,

$$\ddot{\boldsymbol{p}} + \gamma\dot{\boldsymbol{p}} + \omega_0^2\boldsymbol{p} = -f\mathbf{E}_0 \tag{2.27}$$

Where p is induced dipole moment, γ is the internal dissipation rate, ω_0^2 the resonance

frequency, and f the oscillator strength The total electric field E_{tot} on each particle consists of the incident field and the electric field radiated by the dipole, i.e.,

$$\boldsymbol{E}_{total} = \boldsymbol{E}_0 + \frac{\boldsymbol{p}}{2\pi\varepsilon_0 d^3} \tag{2.28}$$

Plugging Eqn. (2.28) into (2.27) yields the equation of motion for the dipole moment for each particle given by,

$$\ddot{\boldsymbol{p}} + \gamma\dot{\boldsymbol{p}} + \omega_0^2\boldsymbol{p} = -f\left(E_0 + \frac{\boldsymbol{p}}{2\pi\varepsilon_0 d^3}\right) \tag{2.29}$$

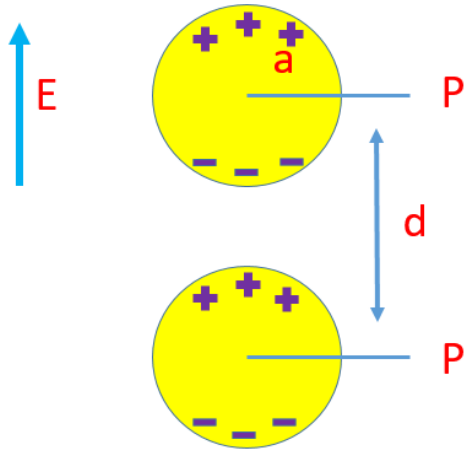

Figure 2.2 Coupling of two dipoles with a distance d.

and the steady solution of the equation of motion is,

$$\boldsymbol{p} = \frac{f\boldsymbol{E_0}}{\omega_{es}^2 - \omega^2 + i\omega\gamma} = \alpha\boldsymbol{E_0} \tag{2.30}$$

where $\omega_{es}^2 = \omega_0^2 - \frac{f}{2\pi\varepsilon_0 d^3}$, corresponding to the coupled dipole-dipole resonance frequency. The dipole-dipole polarizability is not given by,

$$\alpha(\omega) = \frac{f}{\omega_{es}^2 - \omega^2 + i\omega\gamma} \tag{2.31}$$

It is important to note that the coupling between the electric fields of the two dipoles lead

to a shift in its local resonance frequency from ω_0 to ω_{es}. In order to estimate the magnitude of the resonance frequency shift and the effect of a change in the separation distance between the particles on ω_{es}, we can match Eqn. (2.31) to (2.18) and obtain f and ω_{es}, to be,

$$f = 4\pi a^3 \omega_0^2 \tag{2.32}$$

$$\omega_{es}^2 = \omega_0^2 \left(1 - \frac{2a^3}{d^3}\right) \tag{2.33}$$

In these derivations, we assume that each dipole represents a polarizable metal sphere of radius a, and the dielectric constant $\varepsilon_m(\omega)$ follows the Drude model in Eqns. (2.14) and (2.15). Equation (2.31) shows that the coupled dipole resonance frequency increases with separation distance between the particles. The resonance frequency also depends on the particle radius.

2.4.1 *Resonance wavelength shift vs particles separation distance and particle size.*

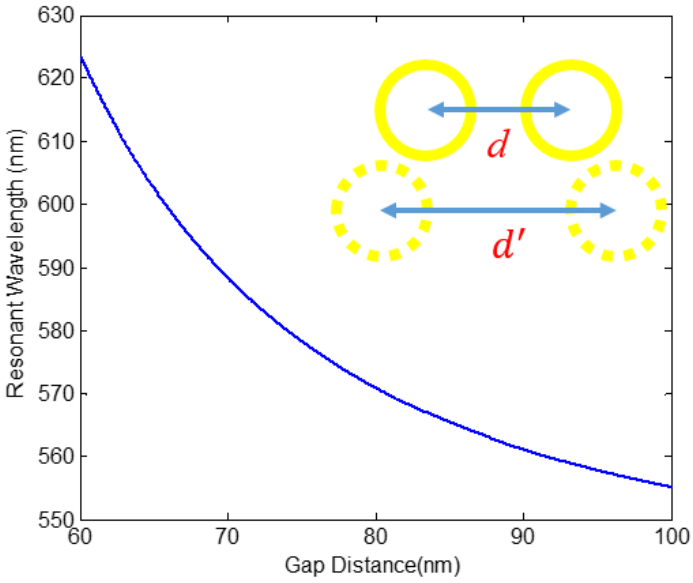

(a)

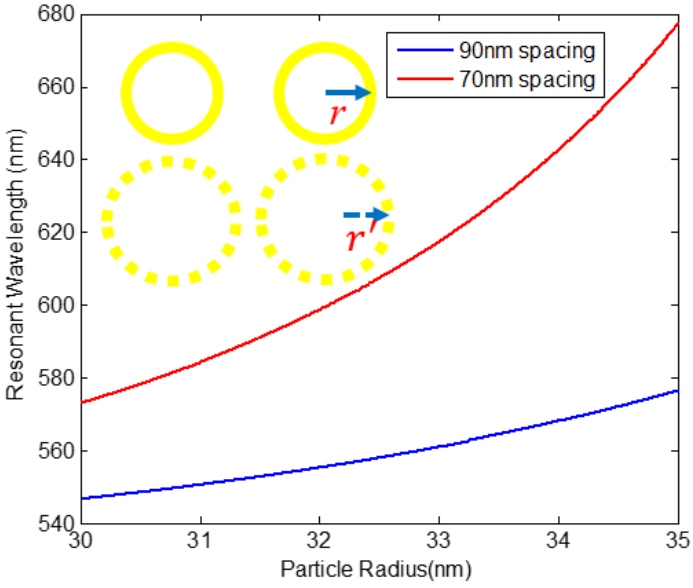

(b)

Figure 2.3 Dependence of resonance wavelength on (a) particle-particle spacing and (b) particle radius.

In this section, the expression for the resonance frequency obtained for the coupled dipoles

are used to examine the dependence of the resonance frequency on the dipole separation distance and particle radius. For example, using a 30nm spherical gold nanoparticle has a localized surface plasmon resonance wavelength of close to 540nm [25]. Consider two gold spherical particles with the same radius of 30nm separated by by a distance of 100 nm, Eqn. (2.33) can be used to calculate the coupled resonance frequency (ω_{es}), and the corresponding wavelength by, $2\pi c/\omega_{es}$= 558 nm. Figure 2.3(a) shows how the resonance wavelength depends on the gap between the particles. Decreasing the gap spacing produces a redshift (increase in wavelength or decrease in frequency) of the single particle plasmon resonance frequency. The limit of the dipole-dipole model is when the two particles touch each other, corresponding to a 60 nm spacing between the particle centers, , in which case, the resonance wavelength becomes 624 nm. It is important to note that for closer gap spacing, the simple dipole approximation for the near-field of the dipole may not be valid since higher order multipole terms are needed to accurately represent the electric field of the dipole. Nevertheless, the dipole provides a phenomelogical framework to interpret the influence of an acoustic modulation of the gap spacing on the plasmon resonance frequency. The resonance frequency of the dipole-dipole resonance also depends on the particle size. The particle size can be modulated by acoustic vibrations in the same way that the gap distance can be perturbed by the motion of the particles. In this case, the plasmon resonance frequency will depend on the internal mechanical modes (breathing and extensional modes) of the each particle Figure 2.3(b) shows the dependence of ω_{es} on the particle radius, for

a fixed gap spacings of 70nm. Increasing the particle radius from 30nm to 35nm produces a redshift in the plasmon resonance from 572nm to 678nm, almost a 100 nm shift in wavelength, which is surprisingly large. For a larger gap spacing of 90nm, the corresponding wavelength shift is reduced to 30nm over the same range of particle radii. The sensitivity of the coupled dipoles to changes in the particle radius increases with decreasing gap separation.

2.5 Surface Plasmon Polaritons (SPPs)

Surface plasmons are electromagnetic excitations that propagate along a metal dielectric interface and decay evanescently away from the surface, as shown in figure 2.4. For the derivation of these excitation, we have to separately solve the Maxwell's equations for the metal and dielectric parts. With the conditions of continuity of the normal and transversal field components on the interface, we can obtain the wave number of SPPs, given by

$$k_{sp} = k_0 \sqrt{\frac{\varepsilon_d \varepsilon_m}{\varepsilon_d + \varepsilon_m}} \tag{2.34}$$

Where k_0 is the wavenumber of free space light, ε_d and ε_m are the dielectric constant of dielectric layer and metal layer. The penetration depth of the field into the dielectric is typically on the order of half of the wavelength in the medium, whereas in the metal, it is determined by the skin depth. Under the assumption that ε_d in the dielectric is approximately constant and using the Drude model for ε_m in metal, we obtains a dispersion relation as given in figure 2.1 (b). It is realized that the momentum of SPPs is

larger than that of free space light at the same excitation frequency. In order to excite

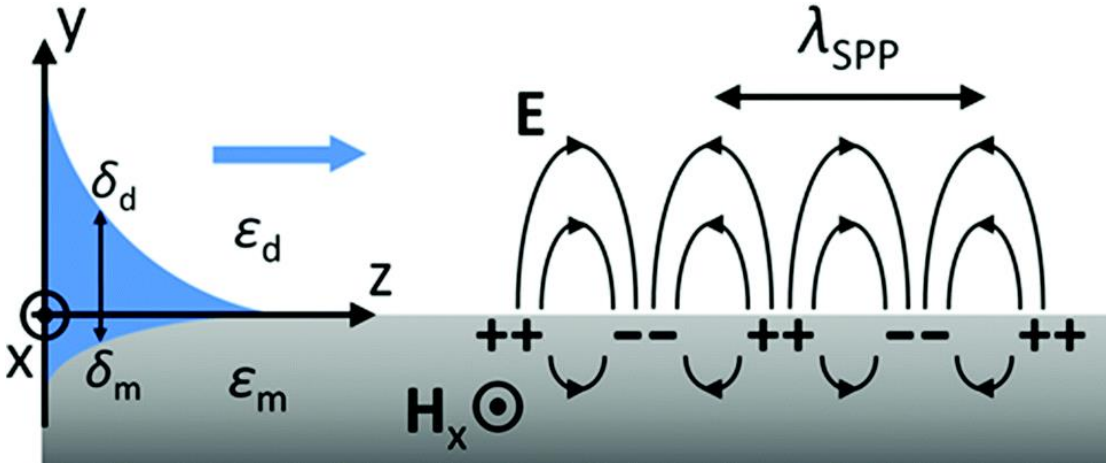

(a)

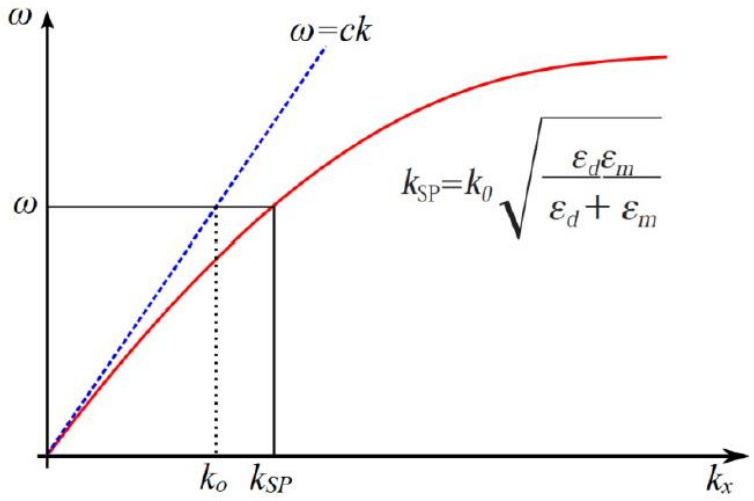

(b)

Figure 2.4 Surface plasmon polaritons. (a) Surface plasmon mode travels at the interface between dielectric and metal. (b) Dispersion relation of surface plasmons compared to light in vacuum

surface plasmon polaritons, we have to fulfill the momentum conservation. The mismatch in wavenumber can be overcomed by using diffraction effects at a grating pattern on the metal surface, which provides additional momentum to bridge the momentum mismatch

between free space light and SPPs. Our plasmonic nano-focusing probe is designed by leveraging grating coupling technique to couple far field light to propagating SPPs on the shaft of the probe. Due to tapered geometry of the probe, the SPPs will propagate towards the probe apex and concentrate the energy to a “hot spot”, creating a focused light source in nanoscale volume.

Chapter 3 Local Mapping of Nanomechanical Vibrations Using Local Modulation of Near-field Optical Interaction

3.1 Introduction

The resonant interaction of light with metallic nanostructures in the visible spectrum has generated significant interest in the literature due to generation of surface plasmon polaritons (SPPs), which can lead to enhanced local optical scattering and absorption, nonlinear optical effects, all of which have the potential for single-molecular detection sensitivity. In addition, nanoscale structures provide a combination of small active masses and size dependent mechanical properties [44, 45], which can change through adsorption of binding analytes or perturbations in the external force or pressure. Numerous authors have proposed to explore these properties in resonance based nanomechanical detection of virus and protein and gas molecules [45], and for study of quantum limited processes [46]. Nanoscale structures also provide promising opportunities for integrating optical and mechanical degrees of freedom, for instance, by using elastic deformation to modulate the propagation of SPPs in nanoplasmonic waveguides [47], and using the spatially confined heating produced by absorption of local surface plasmons for photothermal actuation of elastic deformations [48, 49] in nanostructures and control of thermal transport at the nanoscale [50, 51]. Ultimately, the success of these application

areas depends on the ability to study and understand the interaction of light with nanostructures at the nanoscale, and to address the mechanical properties of nanostructures, which is challenging using conventional optical techniques. For example, SPP propagation cannot be visualized using far-field optical techniques due to the momentum mismatch between free space light and SPPs, and the amplitude of SPPs is confined to nanoscale distances from a sample surface due to their evanescent nature.

This chapter explores the resonant optical interaction of two metallic nanostructures in the near-field to produce strong electromagnetic field confinement, and to probe the gap-width dependent optical scattering intensity for detection of resonant mechanical vibrations. We explore the transient modulations of the local optical interaction for local measurement of the ring down mechanical vibrations in two orthogonal directions in a chromium coated silicon nanowire actuated by a pulsed photothermal source. Through measurement of multiple vibration resonance frequencies, the elastic moduli of the silicon nanowire along the [100] and [110] directions and processing induced residual stress are obtained by relating the frequencies to continuum mechanics theory. Measurement of transient mechanical vibrations may be important for studying Brownian structural dynamics of nanoscale structures, which conventional scanning probe techniques cannot track due to their limited bandwidth.

The apertureless near-field optical microscopy (a-NSOM) technique is particularly suitable for the measurement, since it allows for controlling the optical near-field interaction between the metallic tip of an oscillating atomic force microscope (AFM) and a sample

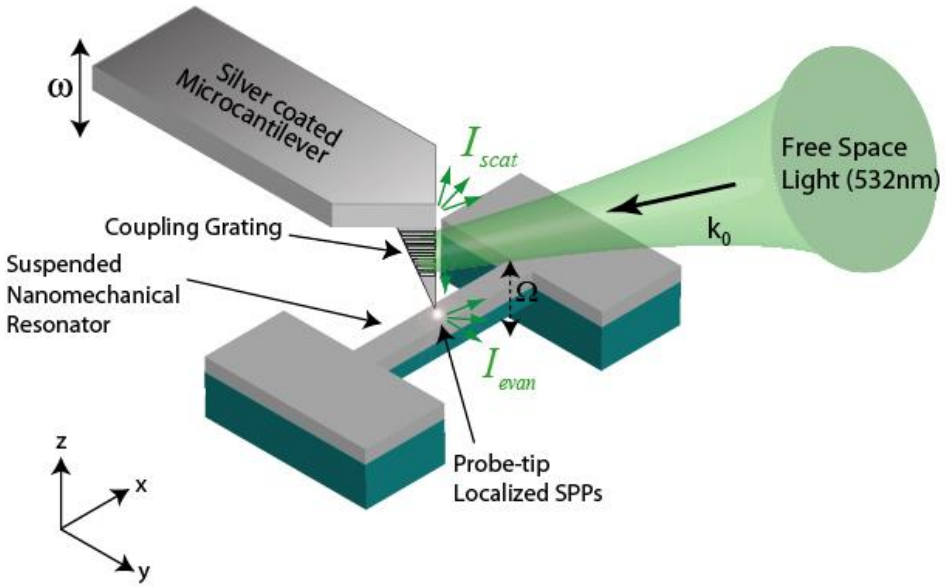

Figure 3.1 Schematic diagram of the a-NSOM probe incorporating a plasmonic grating for generation of localized plasmons at the probe-tip. The *y* and *z* axes of the silicon nanomechanical resonator are oriented along the [110] and

with sub-nanometer accuracy. We enhance the local tip-sample optical interaction by coupling free space light in the visible spectrum (wavelength (λ) = 532nm) to localized surface plasmons (LSPs) at the metal tip. A schematic of the a-NSOM system is shown in Fig. 3.1. The diffraction grating on the silver coated AFM cantilever is used to couple free space light to propagating SPPs by matching the momenta. The excited SPPs are progressively converted to localized surface plasmons (LSPs) at the AFM probe-tip. The probing LSPs extends through a distance of close to one probe-tip radius ($a \sim 20\text{nm} << \lambda$)

in any direction, which sets the distance of the near-field optical interaction between the probe-tip and the sample. The near-field interaction between the probe-tip and the sample is resonantly enhanced by SPPs excited in the chromium coated silicon nanowire by the visible light source. We present experimental results that show the distance-dependent modulation of the near-field optical interaction under harmonic and transient conditions. In order to facilitate the measurements, we introduce a double frequency modulation scheme to isolate the weak near-field optical interaction measured against the large background scattering from the sides of the sample and the AFM probe. This work provides a promising step towards leveraging plasmon propagation for optical probing of dynamic elastic deformation in isolated nanowires with nanoscale lateral spatial resolution and high temporal resolution. In the future, by incorporating ultrafast lasers with the a-NSOM probe, new capabilities for investigating and manipulating acoustic phonon propagation in nanostructures, and studying the interaction of propagating plasmon polaritons and phonons can be realized.

3.2 Plasmonic Nanofocusing Probe

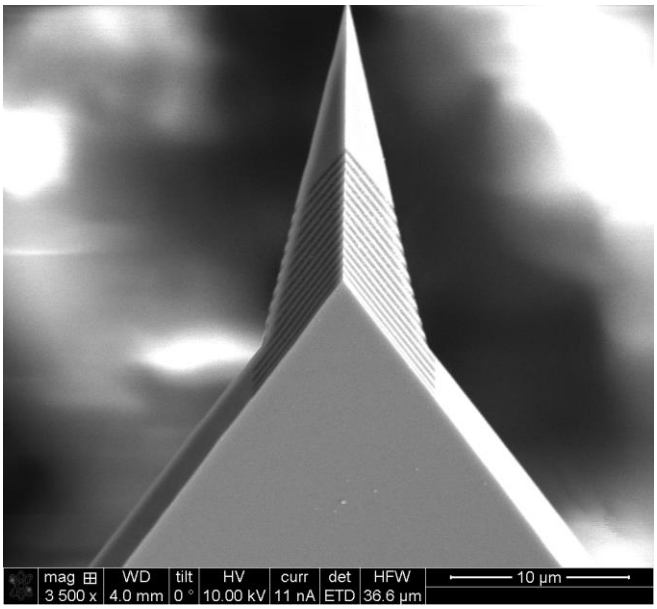

Figure 3.2 SEM image of fabricated plasmonic nanofocusing probe

The plasmonic nanofocusing probe, shown in the scanning electron microscope (SEM) images in Figure 3.2, is fabricated from a commercial silicon AFM scanning probe (VIT_P, NT-MDT). The probe is coated with a 200 nm thick silver film using e-beam deposition, and a one-dimensional SPP coupling grating is fabricated on the front facets of the shaft by focused ion beam (FIB) milling. The diffraction grating couples far field illumination light to SPPs, which propagates along the tapered surface and are focused at the probe-tip. Based on our experimental experience, oxidized silver film dramatically reduces the coupling efficiency due to small scattering particles as shown in figure 3.3 (a). In addition, short propagation distance between the probe-tip and coupling grating, shown in figure 3.3 (b) decreases nanofocusing efficiency.

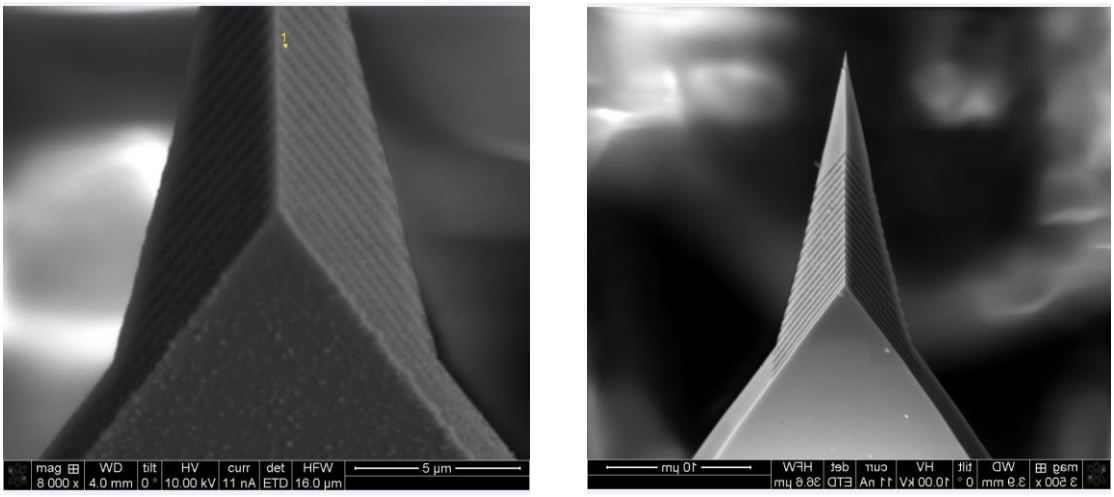

(a) (b)

Figure 3.3 SEM image of (a) oxidized silver film and (b) plasmonic probe with short SPPs propagation distance between the probe-tip and coupling grating.

3.3 Experimental Setup

A schematic of the a-NSOM system is shown in Fig. 3.4 In the figure, a coherent *p*-polarized (along the *x*-*z* plane) frequency doubled neodymium yttrium aluminum garnet (Nd:YAG) laser at 532nm is focused through a 10x microscope objective on the coupling grating at an oblique incidence angle of 15^0 with respect to the normal line on the micro-cantilever facet. The optical power of the illumination laser is limited to less than 0.5mW to prevent damaging the coated film. The first order diffraction of the grating provides the momentum needed to couple the laser source to propagating SPPs in the silver film. The excited SPPs propagate along the tapered surface of the cantilever probe and are focused at the probe-tip producing localized surface plasmons (LSPs). In our previous work[7], we

estimated that the intensity of the LSPs is confined to a spot size of less than 34nm at the maximum (FWHM) intensity level at the probe-tip. The AFM cantilever oscillates at its resonance frequency, $\omega = 330$ kHz with an amplitude of 10nm, and a constant cantilever deflection is maintained using a closed-loop feedback system, such that the average distance between the probe-tip and the sample is always constant during our experiments. The scattered light from the probe-tip and sample interaction region is collected by the 10x microscope objective and directed to a high-speed avalanche photodetector (APD), where

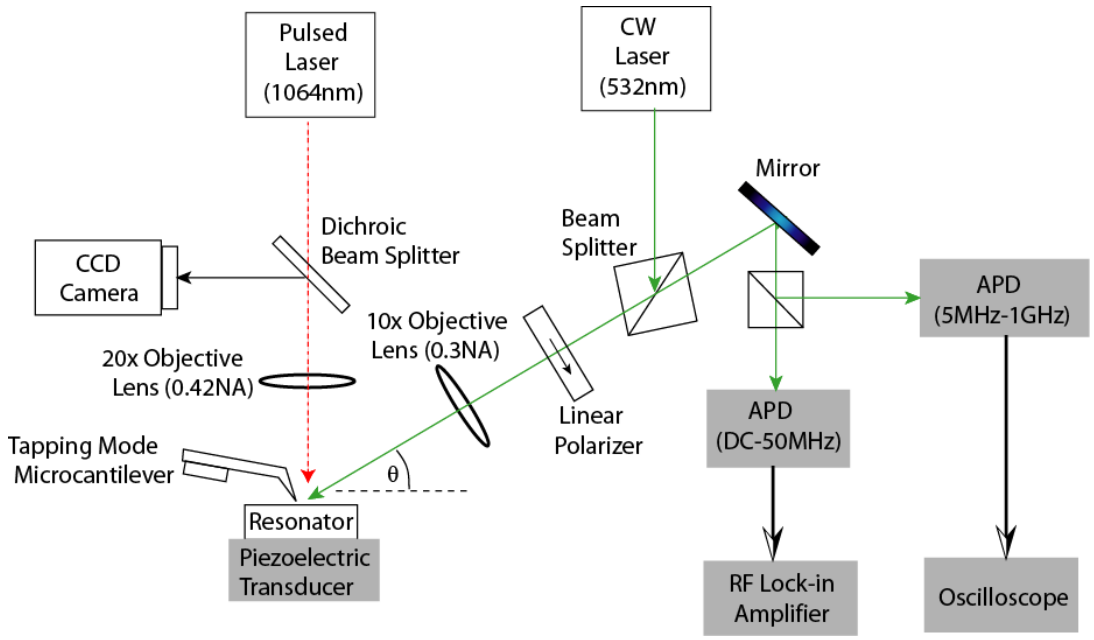

Figure 3.4 Schematic of experimental setup used to actuate and detect flexural nanomechanical vibrations. The following labels are used, CW- continuous wave laser and APD – avalanche photodetector.

the intensity of the near-field interaction is monitored. The scattered electric field, E_{sa}, varies nonlinearly with separation distance between the probe-tip and the sample and the magnitude of the interaction can be approximated using a quasi-static dipole model [64].

The model yields the following analytical expression for the scattered field, $E_{sca} \propto \alpha_{eff} E_i$, where

$$\alpha_{eff} = \frac{\alpha(1+\beta)}{16\pi(a+z)^3} \tag{3.1}$$

is the effective polarizability of the metal tip-sample system, which is comprised of the tip dipole and a mirror dipole in the sample, α is the polarizability of the tip, which has a radius of a, β is a sample's response function related to the sample's dielectric constant ϵ by $\beta = (\epsilon - 1)/(\epsilon + 1)$. The tip-sample distance is denoted by z and E_i is the electric field of the incident field. The modulation of z due to the oscillation of the AFM cantilever at ω leads to a corresponding modulation of E_{sca} at several harmonic frequencies $n\omega$ (n = 1,2,3,…). Typically, the scattered light intensity recorded by the APD is demodulated at higher harmonic frequencies ($n \geq 2$) in order to eliminate unwanted background contributions from light scattering from the sample and the sides of the cantilever. In the measurement system, the harmonic component of the near-field intensity is monitored in a lock-in amplifier, using the electrical voltage output from the APD as the input signal.

3.4 Sample Fabrication

The samples used in this study are doubly clamped bilayer nanomechanical resonators fabricated using electron-beam lithography, electron-beam deposition, and reactive ion etching. Details of the fabrication processes have been discussed elsewhere [52]. The

original dimension of the fabricated nanomechanical resonator are as follows: length = 9.5μm, width = 1.2 μm, and total thickness of 220nm comprised of silicon with thickness

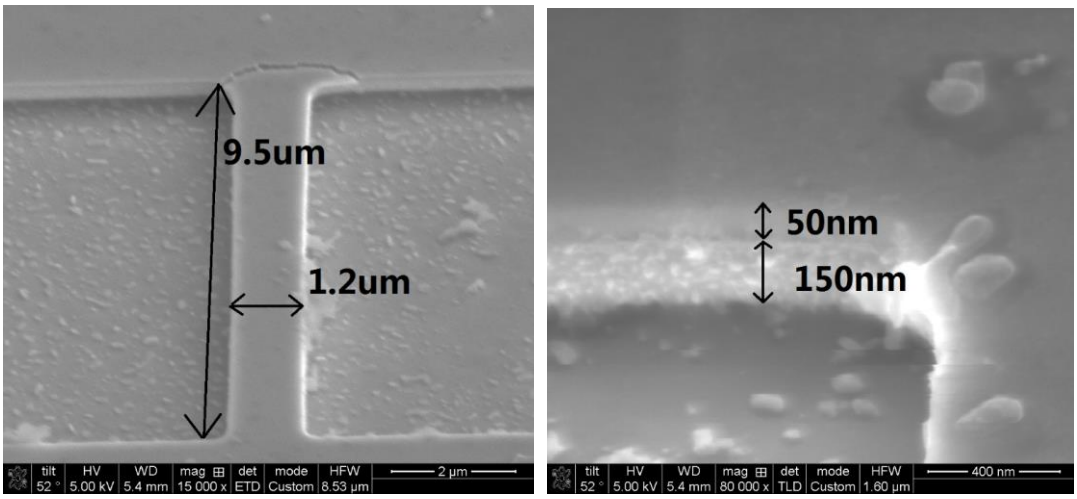

(a) (b)

Figure 3.5 SEM image of the original nanomechanical resonator. (a) top view shows the length and width and (b) side view shows the thickness of chromium coating and silicon resonator.

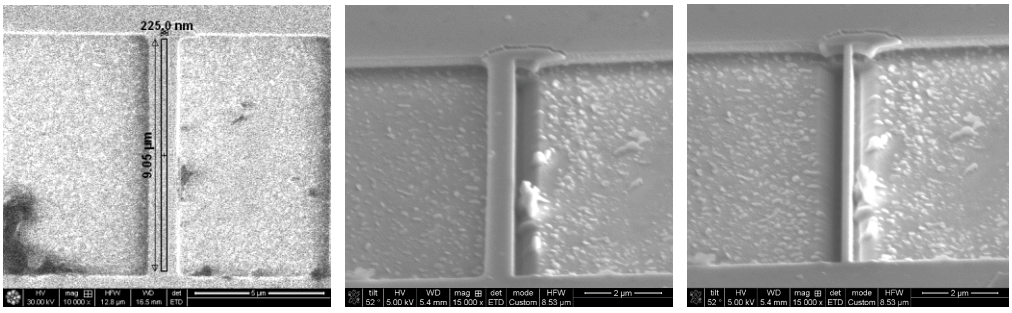

(a) (b) (c)

Figure 3.6 SEM images showing the process of FIB milling

of 150nm and a 50nm thick chromium, shown in figure 3.5 The chromium coating on the silicon resonator is used to couple free space light to SPPs, leading to enhancement of the scattered light from tip-sample interaction region, which is used for transducing the motion

of the resonator. The width of the resonator is further reduced to approximately 270nm by focused ion beam milling using a 30keV (48 pico- amperes) Ga^+ ion source. Figure 3.6 shows the process of FIB milling of the nanowire, where the width of the sample can be visualized during fabrication. The fabricated nanowire is shown in figure 3.7, which has

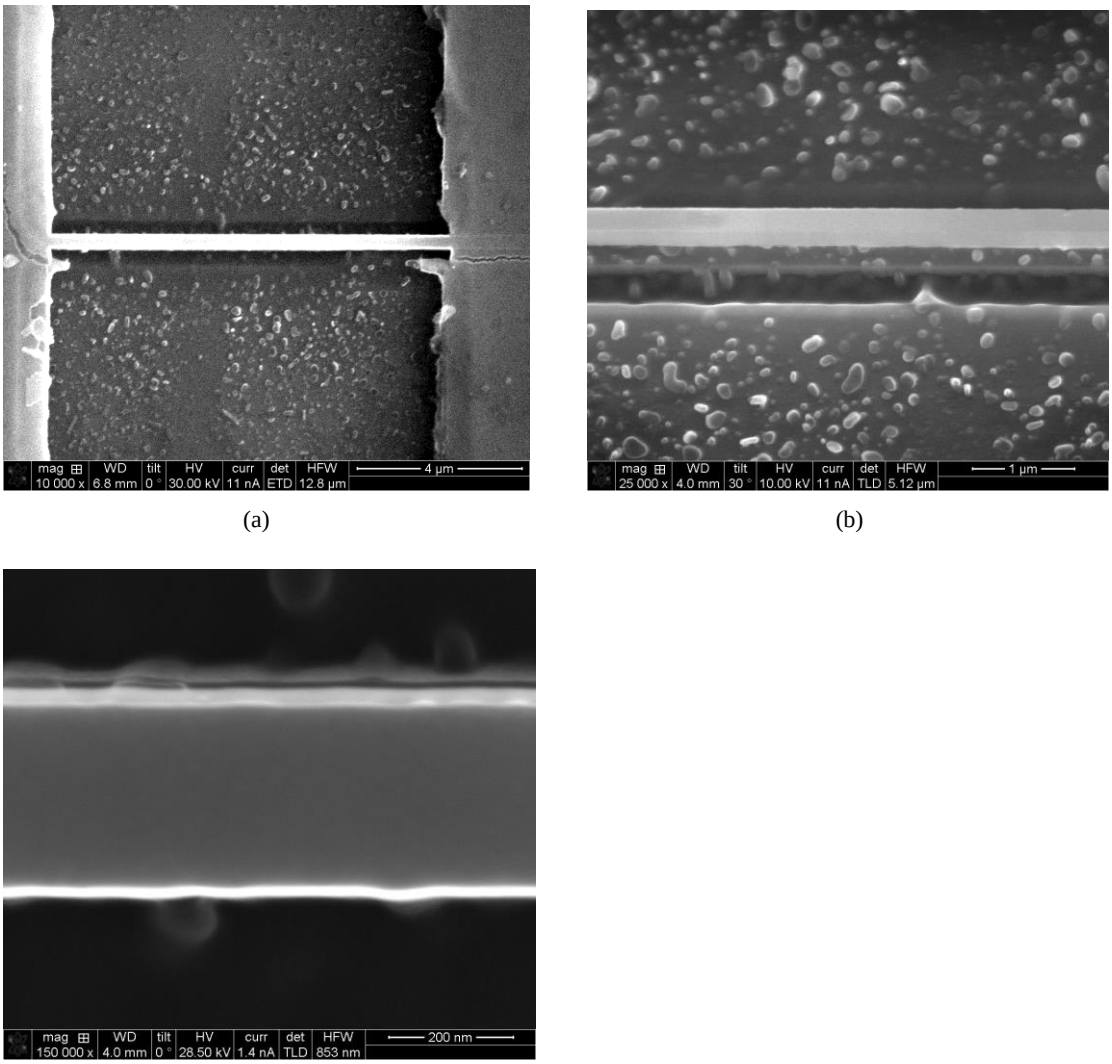

(a) (b)

(c)

Figure 3.7 Scanning electron microscopy images of the fabricated chromium coated silicon nanowire showing (a) its length and clamps, (b) side, and (c) top views.

an asymmetric rectangular cross section, where the width and thickness are slightly different.

3.5 Distance Dependence of Tip-Sample Near-field Interaction

First, we study the distance-dependence of near-field interaction between two oscillating

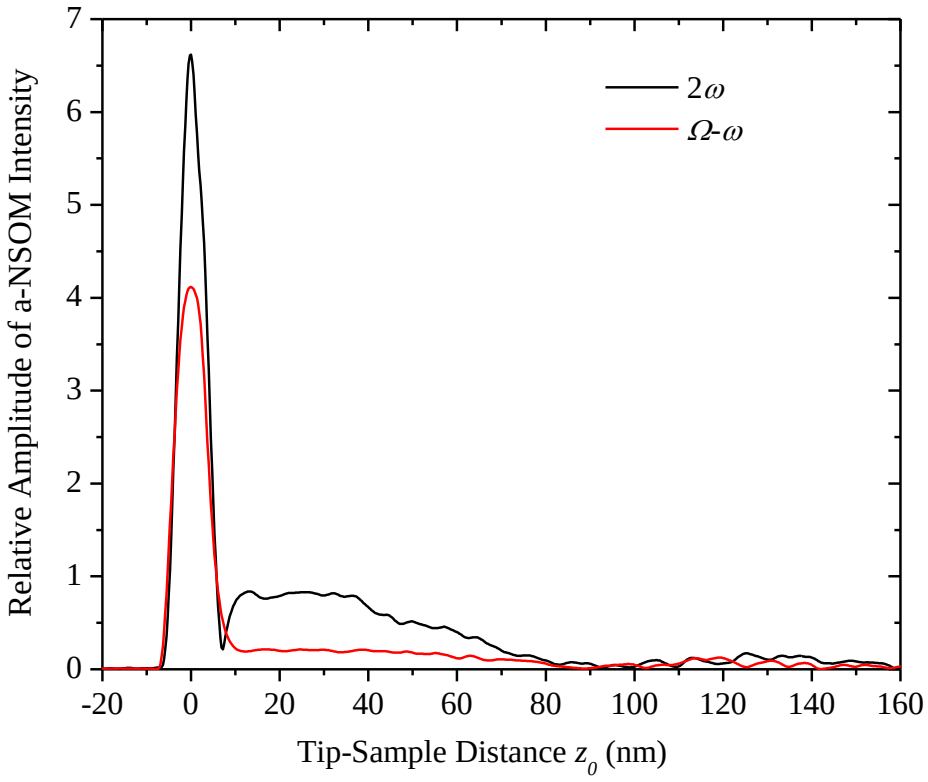

Figure 3.8 Response of the a-NSOM at demodulation frequencies, 2ω and $\omega - \Omega$, during the probe-tip sample approach. The probe-tip makes intermittent contact with the sample a $z_0 = 0$.

nanostructures. The sample is oscillated at its fundamental vertical flexural resonance frequency $\Omega = 24$MHz by a piezoelectric transducer bonded to the sample substrate and driven with an electronic signal generator. Consequently, the tip-sample distance is

modulated following, $z(t) = z_0 + A_1 \cos 2\pi\omega t + A_2 \cos 2\pi\Omega t$, where A_1 ~10nm and A_2 ~1nm are the oscillation amplitude of the AFM cantilever and the sample respectively, and z_0 is the average distance between the probe-tip and sample. The nanowire oscillates in the *x*-*z* plane, with the flexural displacement along the *z* direction. The oscillation of the tip and sample leads to modulation of the scattered intensity at frequencies, $n\omega, m\Omega,$ (n, m = 1,2,3..), and at the sum and difference of these frequencies. For the measurement, a portion of the drive voltages to the AFM cantilever and the sample piezoelectric transducer are combined in an electrical mixer and the difference frequency output from the mixer is fed into the lock-in amplifier as a reference input. The amplitude of the lock-in amplifier output is monitored using a measurement a time constant of 100μs. Figure 3.8 compares the measured light intensity at the first harmonic of the oscillation frequency of the cantilever and the difference frequency $\omega - \Omega$, as the tip approaches the center of the nanowire. In the measurement, z_0 is varied continuously, while the oscillation amplitudes, A_1 and A_2 are kept constant until the beginning of the tapping mode regime. The measured intensity at the difference frequency reduces to the noise floor at larger distances over which the unwanted background is expected to persist, while the demodulated intensity at 2ω shows a larger secondary lobe at distances between 10nm and 80nm, due to the interference of the near-field and the un-modulated portion of the background [53]. The probe-tip approach distance is zero when z_0 becomes equal to A_1 for the 2ω data, and A_1+A_2, for the $\omega - \Omega$ data. At this position, the tip makes intermittent contact with the

sample during its oscillation cycle and the intensity plots go through a maximum. Further decrease in the approach distance puts the tip further in contact with the sample, which leads to a decrease in the measured intensity due to the limited oscillation amplitude of the AFM cantilever. We note that demodulation of the scattered light intensity at $\omega - \Omega$ provides local sensitivity to the local optical field on the nanowire and suppression of unwanted background, provided that average probe-tip sample distance is maintained within 10nm of the sample surface.

3.6 Spatial Mapping of Vibration Mode Shape

To further demonstrate the versatility of the difference frequency approach, we map the fundamental mode shape of the nanowire by raster scanning the sample over a 10μm x 10μm area, and recording the intensity of the scattered light at $\omega - \Omega$. Figure 3.9 shows pseudo color maps of the topography and the measured tip-sample scattering intensity, where the vertical axis is limited to the scan distance of 1.6μm. The intensity image shows enhanced light scattering around the edges of the nanowire, where the incident light is coupled to SPPs. Closer examination of the sample topography and a-NSOM images reveals differences in the beam width. In order to investigate these differences, cross-sectional line scans of the a-NSOM intensity and the topography taken across the width of the nanowire are plotted in Fig. 3.9(c). Several height-induced artifacts are observed in the topography data that correlates with the intensity peaks in the a-NSOM intensity data. The

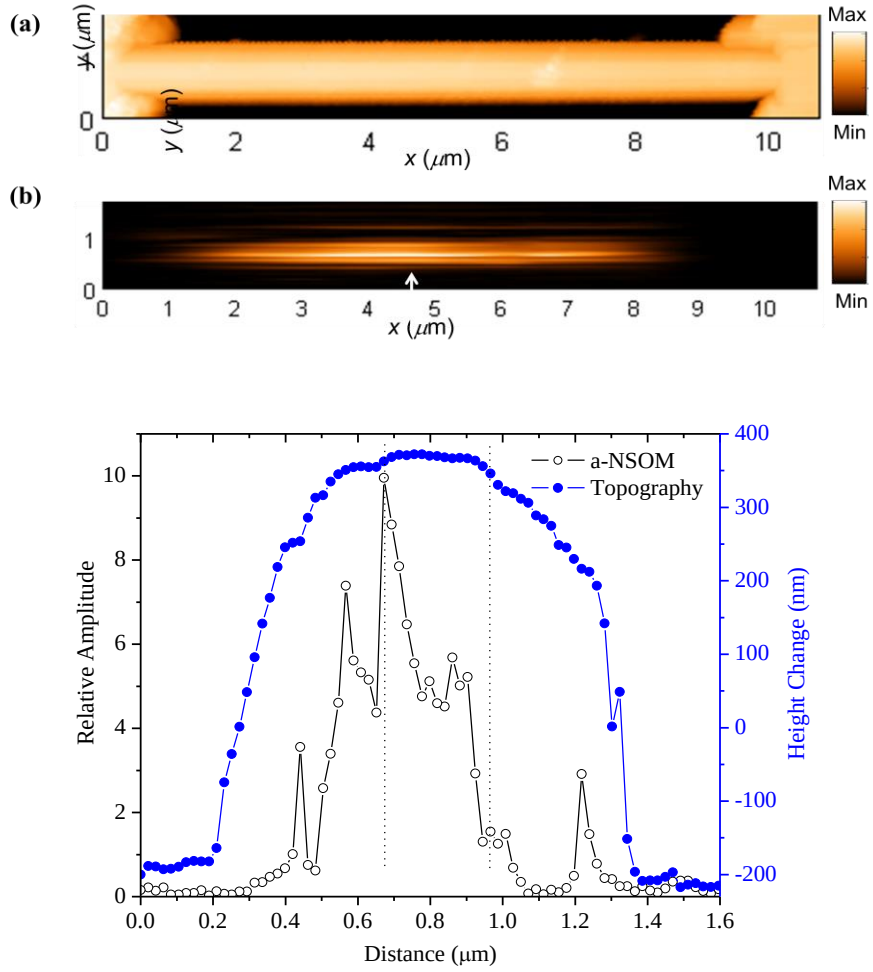

(c)

Figure 3.9 Topography (a) and a-NSOM (b) images of the suspended nanowire. (c) shows cross sectional line scans of the topography and a-NSOM intensity taken along the *y* direction across the middle of the nanowire. The arrow in the figure indicates the direction of illumination laser.

artifacts are due to the inability of the AFM to track the abrupt height jumps between the substrate and effects of lateral cantilever deformations as the probe-tip interacts with vertical wall. Focusing on the flat portion of the line scan corresponding to the chromium film, which is indicated by the region between the dotted lines, we observe that the a-

NSOM intensity decreases almost monotonically from one film edge to the other, due to a combination of the asymmetric illumination and collection of the scattered light. The distance between the lines, which represents the a-NSOM estimate of the beam width is 293nm, which is larger than the estimated value from the SEM image by 23nm. The over-estimate in the width of the nanowire is due to the finite probe-tip radius, which is close to 20nm. Compared to the noise floor (distances of 0 to 0.2 μm in Fig. 3.9(c)), the maximum intensity on the nanowire (signal) is 50 times larger due a combination of enhanced scattering by local SPPs on the chromium film and suppression of background optical fields by demodulation of the a-NSOM intensity at the difference frequency. The mode shape of the fundamental resonance observed in the a-NSOM image follows the predictions by basic continuum theory, where the intensity (or displacement) is maximum close to the middle of the resonator and decreases to the noise floor at the clamps.

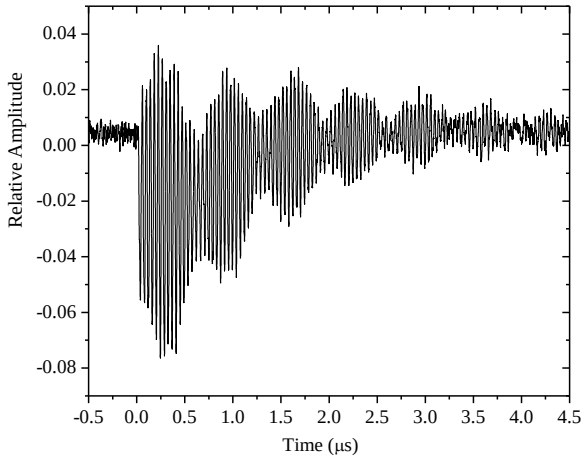
Relative Amplitude
0.04
0.02
0.00
-0.02
-0.04
-0.06
-0.08
-0.5
0.0
0.5
1.0
1.5
2.0
2.5
3.0
3.5
4.0
4.5
Time (μs)

(a)

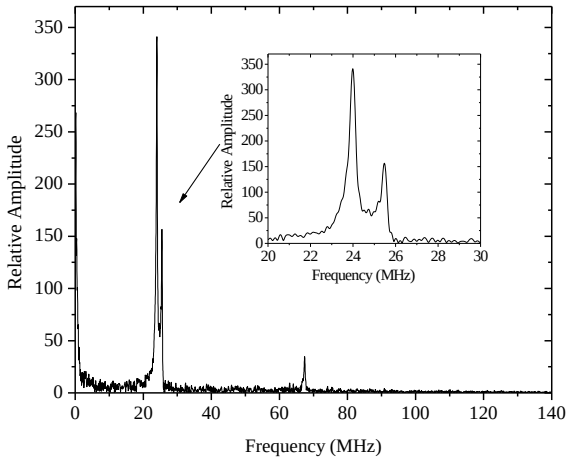
Relative Amplitude
350
300
250
200
150
100
50
0
0
20
40
60
80
100
120
140
Frequency (MHz)
Relative Amplitude
Frequency (MHz)

(b)

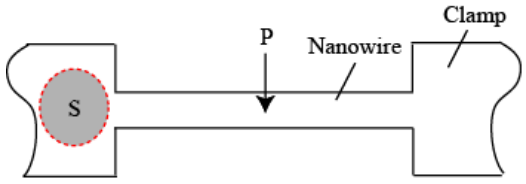
Clamp
P
Nanowire
S

(c)

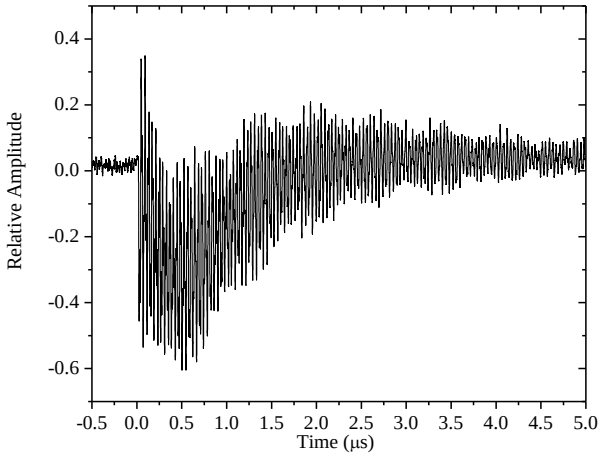
Relative Amplitude
0.4
0.2
0.0
-0.2
-0.4
-0.6
-0.5 0.0 0.5 1.0 1.5 2.0 2.5 3.0 3.5 4.0 4.5 5.0
Time (μs)

(d)

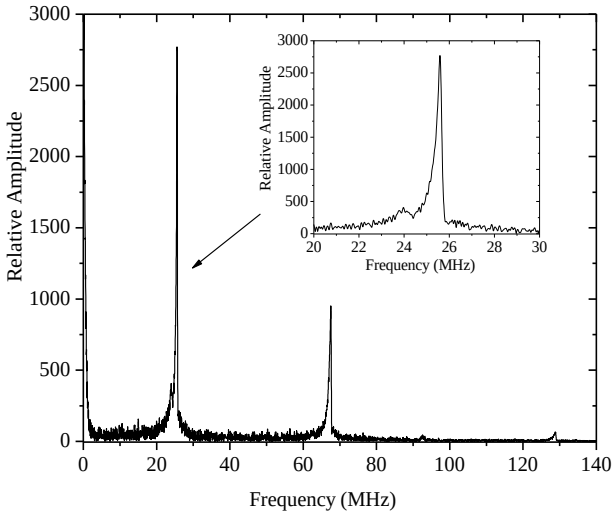
Relative Amplitude
3000
2500
2000
1500
1000
500
0
0 20 40 60 80 100 120 140
Frequency (MHz)
Relative Amplitude
3000
2500
2000
1500
1000
500
0
20 22 24 26 28 30
Frequency (MHz)

(e)

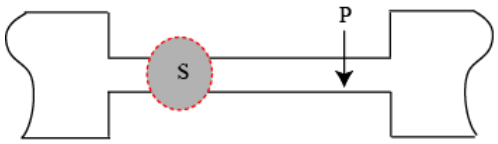
P
S

(f)

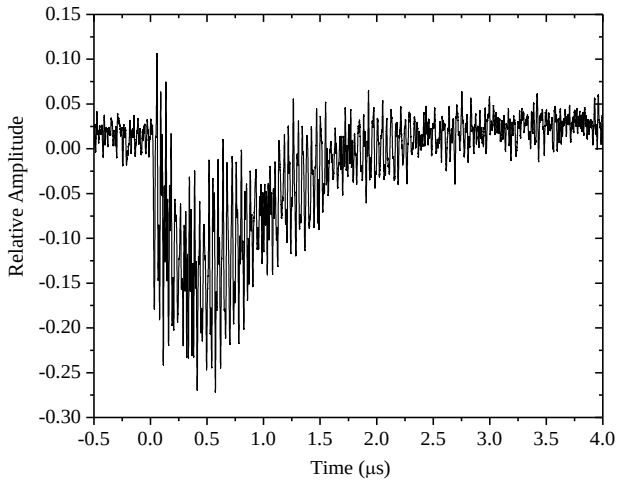
Relative Amplitude
Time (μs)
0.15
0.10
0.05
0.00
-0.05
-0.10
-0.15
-0.20
-0.25
-0.30
-0.5
0.0
0.5
1.0
1.5
2.0
2.5
3.0
3.5
4.0

(g)

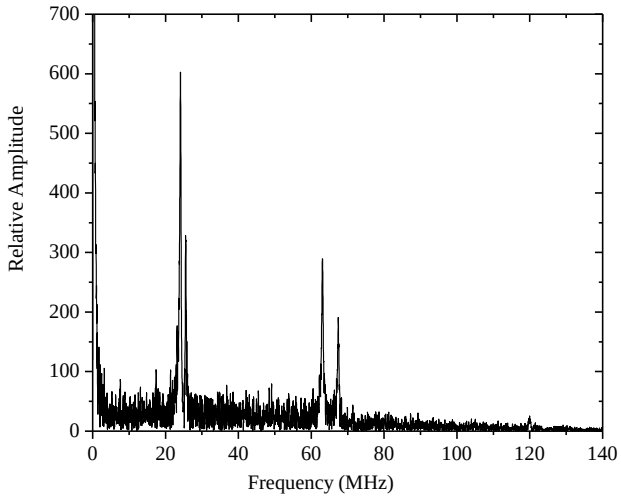
Relative Amplitude
Frequency (MHz)
700
600
500
400
300
200
100
0
0
20
40
60
80
100
120
140

(h)

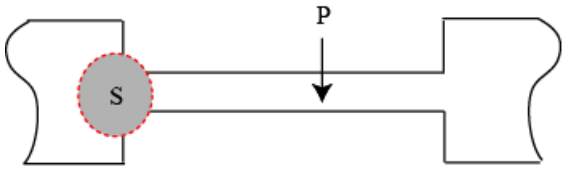
P
S

(i)

Figure 3.10 Time resolved vertical and horizontal flexural ring down vibrations measured at various locations on the coated silicon nanowire. (a), (d), and (g) shows the time domain data, (b), (e), and (h) shows their corresponding amplitude spectra, and (c), (f), and (i) show schematics of the experimental configuration and positions of photothermal source (S) relative to the a-NSOM probe (P).

3.7 Transient Vibration Measurement and Quantitative Characterization of Nanowire Elastic Properties

Next, we explore the use of the resonance frequencies for quantitative characterization of the elastic properties of the nanowire. For this purpose, we introduced a pulsed laser into the experimental setup to enable photothermal actuation of multiple mechanical resonances in the 270 nanowire. In the experiment, a pulsed Nd:YAG laser with a pulsed width of 1.0ns and wavelength of 1064nm is focused through a 20x microscope objective lens positioned directly above the a-NSOM cantilever and sample. The spot size of the pulsed laser on the sample is approximately 5μm. The absorption of the pulsed laser in the chromium film leads to local heating, transient thermal expansion, and dynamic actuation of flexural resonances in the nanowire. The motion of the nanowire is monitored by feeding the output of the APD into a 5GHz oscilloscope that is triggered in sequence with the repetitive firing of the pulsed laser. The measured data is averaged 1000 times in the oscilloscope to suppress incoherent noise. During the measurement, a small percentage of the APD output is fed into the lock-in amplifier, and the amplitude of the signal component

at the first harmonic frequency (2ω) of the AFM tapping mode frequency is monitored. Figure 3.10 shows representative waveforms and their corresponding amplitude spectra of the under-damped ring down

vibration of the nanowire obtained at three different positions. Cartoon illustrations of the sample showing representative positions of the pulsed laser and the a-NSOM probe during the experiments are also shown in the figure. The positions of the pulsed laser

and a-NSOM probe on the nanowire are separated in order to prevent direct laser heating of the AFM cantilever, which can degrade the detection sensitivity. The measured waveforms are correlated with the 2ω a-NSOM intensity measured in the lock-in amplifier. When the 2ω signal decreases to the noise floor, possibly due to misalignment of the incident light on the plasmonic grating on the AFM tip, the transient ring down waveform also reduces to the random noise background. A beat phenomenon is observed in the ring down vibration waveforms, which may result from decomposition of the nanowire deformation into two orthogonal vibration components with close frequencies along the horizontal and vertical directions. For the first waveform where the beat phenomenon is distinct, the frequencies of the amplitude peaks of the interfering fundamental vibration modes are separated by 1.2MHz in the amplitude spectrum. The quality factors of the resonance modes in air are high enough to spectrally resolve the frequency difference between the resonance modes. The small difference in the modal resonance frequencies stem from slight asymmetry of the cross-sectional geometry of the nanowire, which leads

Waveform #	Vertical Resonance Frequency (MHz)			Horizontal Resonance Frequency (MHz)		
	Fundamental	First Harmonic	Second Harmonic	Fundamental	First Harmonic	Second Harmonic
a	24			25.5	67.4	
d				25.6	67.5	128.8
g	24.1	63.1	120	25.5	67.4	

Table 3.1 Resonance frequencies extracted from the spectra of the measured waveforms

to close moment of inertia along the principal directions of the (110) nanowire, i.e., the [110] and [001] directions. In the nanowire geometry shown in Fig. 1(a), the *z* and *y* axes are parallel to the [001] and [110] directions of the nanowire. The sensitivity of the a-NSOM probe to the horizontal motion of the nanowire is due to the 25^0 mis-alignment of the vibration axes of the AFM cantilever and the nanowire. The angular mis-alignment is estimated from the AFM topography of the nanowire. A list of resonance frequencies extracted from the amplitude spectra of the measured waveforms are presented in Table 3.1. We observe a slight increase in the resonance frequencies with amplitude of the ring downs vibrations, particularly in the second waveform where the photothermal source is positioned close to the center of the nanowire. At this position, the horizontal flexural resonances are dominant and the shape of the amplitude spectrum deviates from the typical Lorentzian function, which is expected for a linear resonator. The nonlinear amplitude spectrum resembles the prediction from a duffing oscillator model [54], and the nonlinear vibration in this case may result from axial stretching of the nanowire. The disappearance of the vertical vibration modes is strange but may result from rotation of the displacement

polarization with increasing oscillation amplitude [55]. On the other hand, when the photothermal source is wholly off the nanowire (Fig. 3.10(a)) or partially on it (Fig. 3.10(g)), the amplitude of the vertical and horizontal modes are comparable. The slight increase in the resonance frequency of the modes with vibration amplitude may be due to operation of the resonator in the nonlinear regime, as a result of the increased bending-induced tension in the nanowire that accompanies large changes in its length. The length change can result from thermal expansion of the nanowire, which is pronounced in comparison to the oscillations in the second and third waveforms (Figs 3.10(d) and 3.10(e)). The transient thermal expansion of the nanowire in these cases appears as a low frequency envelope superimposed on the ring down vibration data, and it relaxes to the horizontal baseline within 1.5μs. It is unlikely that the transient thermal expansion of the nanowire can lead to significant shifts in resonance frequency since the time-scale of the thermal expansion is smaller than the ring down vibration time of the nanowire.

Finally, we fit the measured fundamental resonance frequencies of the vibration modes to the Euler Bernoulli beam theory to obtain the elastic moduli of silicon along the [001] and [110] symmetry directions and the processing induced tensile stress. We used the resonance frequencies obtained from amplitude spectra plotted in Fig. 3.10(b), where the amplitude of the vibrations are smallest and the spectrum of each mode is close to a Lorentzian

function. The resonance frequencies for a pre-stressed doubly clamped rectangular beam in either the vertical or horizontal directions can be shown to follow the relation,

$$f_n = \frac{1}{2\pi}\frac{\lambda_n}{l^2}\sqrt{\left(1+\frac{\sigma(A_{cr}+A_{si})l^2}{\lambda_n^2 EI}\right)\frac{EI}{\rho_{cr}A_{cr}+\rho_{si}A_{si}}} \quad (3.2)$$

In the equation above, the symbols ρ and A represent the density and cross sectional area and the subscripts *cr* and *si* are used for the copper and silicon layers. *EI* is the effective flexural rigidity of the silicon-chromium composite beam, which depends on the elastic moduli of the silicon E_{si} along the principal directions, the chromium film E_{cr}, and the second moment of area I^{31}. For the vertical vibration modes the moment of area about the *z* direction is used, and for the horizontal vibration modes, the moment of area about the *x* direction is used. The residual stress in the nanowire is represented by σ, l is the length, and λ_n corresponds to the eigenvalue for flexural mode n. For the first three resonance modes, $\lambda_1 = 4.73$, $\lambda_2 = 7.853$, and $\lambda_3 = 10.996$ for doubly clamped beam, such that the ratio of the resonance frequencies; $f_2/f_1 = 2.8$ and $f_3/f_1 = 5.4$, for the horizontal and vertical modes respectively. We assume the bulk value of 279GPa for the Young's modulus of chromium and fit the analytical model to the measured fundamental frequencies using the Young's moduli of silicon along the [100] and [110] symmetry directions and the built-in stress as free parameters. The model provides a best fit to the measured frequencies, for Young's moduli of 132GPa and 114GPa along the [100] and [110] directions and a tensile stress of 141MPa. The predicted modulus in the [100] direction is close to the bulk value of 130GPa for (100) silicon, however the predicted modulus in the [110] direction is

smaller than the bulk value of 169GPa. It is possible that the discrepancy in the estimated modulus is due to the non-uniform width of the nanowire. The beam width tapers down to 226nm close to the fixed ends of the nanowire. Reducing the beam width to 237nm yields an elastic modulus along the [110] direction that matches the bulk value for the same beam tensile stress. The large estimated stress may result from bending-induced tension, differential thermal expansion of the chromium film and silicon nanowire, and the residual tension in the layers introduced during the various processing steps. It is also important to remark that matching the analytical model to the combination of the measured fundamental and harmonic resonance frequencies for each of the modes can yield a more accurate estimate of the built-in stresses. However, this approach cannot be applied in this case since the ratio of the resonance frequencies for each mode do not match the predicted values from the Euler Bernoulli model for a doubly clamped beam. For example, the frequency ratios obtained from the experimental data are, f_2/f_1= 2.6 and f_3/f_1= 5.0 for either the vertical or horizontal modes. The discrepancy may result from deviations of the boundary conditions from ideal clamping at nanowire ends.

3.8 Conclusions

In summary, we have explored the a-NSOM technique for local measurement of mechanical vibrations in metallic nanostructures. We showed that light coupling to SPPs in the a-NSOM probe and the nanostructure leads to enhancement in the intensity of the

evanescent SPPs scattered from the interaction region between the sample and the probe-tip to the far-field. We explored the distance-dependence of the scattering intensity to detect local mechanical vibrations in metallic nanowire structures actuated by a piezoelectric transducer and a pulsed laser, and the measured resonance frequencies enabled the estimation of the nanowire elastic properties. The technique is versatile in that it allows for operation in the time- and frequency-domain with sub-wavelength lateral spatial resolution and exquisite temporal resolution. In particular, the time-domain actuation and detection approach may find use in tracking the dynamic evolution of processes, such as single protein binding events, or stochastic vibration of overdamped nanomechancial resonators, with extremely high spatial and temporal resolution. Furthermore, the sensitivity of the a-NSOM technique to SPPs and mechanical vibrations in metallic structures makes it an ideal approach for investigating interesting phenomena that leverage the interaction of propagating polaritons and acoustic phonons of comparable wavelengths confined a single cavity.

Chapter 4 Near-field Optical Detection of Photothermally Actuated Nanomechanical Vibrations using a Plasmonic Nanofocusing Probe

4.1 Introduction

In chapter 3, we explored a hybrid nanofocusing scheme that provided efficient coupling of free propagating light to LSPs at the probe-tip of a SPM. We used the plasmonic probe to detect and map the displacement profile of a chromium coated silicon nanomechanical resonator vibrating at its lowest eigen frequency (~ 18MHz) with lateral spatial resolution of 20 nm. However, the nanomechanical resonator was actuated by a narrowband thickness mode piezoelectric transducer, which limited the range of eigen frequency displacement profiles that could be mapped.

In this chapter, we incorporate an amplified electro-absorptive modulated laser into the optical detection system for photothermal actuation of the resonator at an arbitrary frequency in air under ambient conditions. The steady state harmonic displacement of the nanomechanical resonator is measured by recording the local modulation of the gap between the probe-tip and sample, by demodulating the scattered light intensity in the far-field into a RF lock-in amplifier at the difference between the SPM and sample vibration frequencies. We find that the optical signal at the difference frequency results from the coupled probe-tip and resonator structure, and we explore the signal for mapping the first two eigen vibration mode shapes of the resonator. The measured displacement profiles are

in qualitative agreement with the continuum mechanics calculations of the eigen mode shapes. Owing to the versatility of the measurement approach for narrowband actuation and detection of nanomechanical structures over a broad frequency range, the approach can find applications in characterization of elastic properties of nanostructures based measurement of their resonant vibration frequencies, and studies of nanoscale temperature fields in photothermally actuated structures.

4.2 Experimental Setup

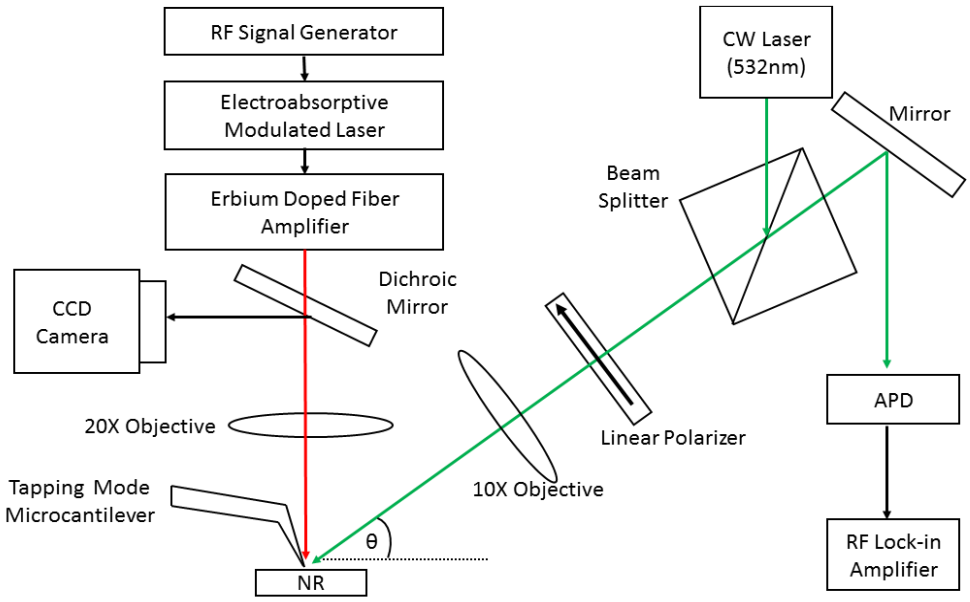

Figure 4.1 Experimental setup The nanomechanical resonator is actuated by a photothermal source (red arrow) and the displacement of the nanomechanical resonator is detected by the optical scattering (green arrow) from the probe-tip and sample gap. The following labels are used: NMR - nanomechanical resonator, CCD-charge coupled device, CW- continuous wave laser, APD- avalanche photodetector, and RF -radio frequency.

Figure 4.1 shows a schematic representation of the experimental setup. A C-band diode laser with wavelength near 1550nm is used for photothermal actuation of the nanomechanical resonator. The laser source (Fig 4.2), an integrated electroabsorptive intensity modulator with a 2.5 GHz bandwidth is driven by a radio frequency (RF) signal generator. The intensity modulated laser is amplified by a 5W erbium doped fiber amplifier (EDFA), and directed through a 20x long working distance microscope objective with a numerical

(a) (b)

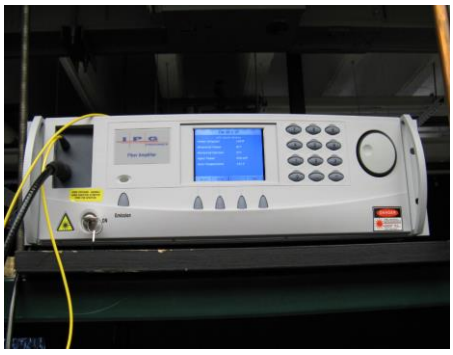

(c)

Figure 4.2 Intensity modulated laser source (a) laser diode controller (b) radio frequency signal generator (c) erbrium doped fiber amplifier

aperture of 0.42 that focuses the laser on the sample surface. The laser is absorbed on the sample surface leading to heating and a modulated thermal expansion. The sample consists of a doubly-clamped bilayer flexural resonator with the following nominal dimensions: length = 7 μm, width = 1.2 μm, thickness = 250 nm, comprised of 200 nm thick silicon and 50 nm chromium film. Due to differences in the thermal expansion coefficient of the silicon and chromium layers, the mismatched thermal expansion of the layers induce thermal bending stresses in the layers that are relieved by the flexural displacement of the resonator. The position of the photothermal source on the nanomechanical resonator can be monitored with a standard microscope objective in the experimental setup. In the microscope, a white light source is focused on the sample surface through the 20x microscope objective and the reflection from the sample is directed through a tube lens to a CCD camera, where the image of the sample is formed.

The flexural displacement of the nanomechanical resonator is detected by the plasmonic nanofocusing probe illustrated in the Figure 4.3. The plasmonic nanofocusing probe is a commercial silicon atomic force microscope (AFM) cantilever coated with 200 nm thick silver film. The probe-tip radius is about 10nm. A one-dimensional diffraction grating with period of 667 nm is written on the tapered portion of the probe to facilitate direct excitation of SPPs by far-field illumination. A continuous wave probe laser with wavelength of 532 nm is focused through a 10x microscope objective onto the diffraction grating, and the excited SPPs couple to LSPs at the probe tip. A *p*-polarized illumination source is used to

enhance the excitation of the SPPs. The AFM cantilever is operated in tapping mode, which

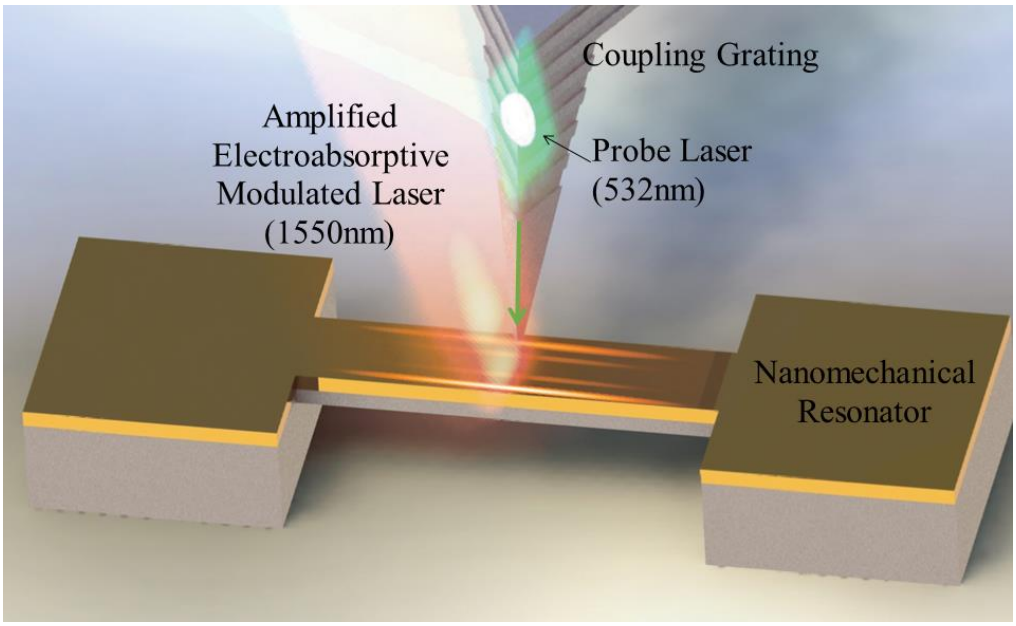

Figure 4.3 Illustration of the plasmonic nanofocusing probe positioned above a nanomechanical resonator.

allows for controlling the average gap between the probe-tip and sample during the modulation cycle, using an electronic feedback circuit. The light scattered from the gap region is collected by a 10x microscope objective at an oblique angle and detected by an avalanche photodetector (APD) with a 3-db bandwidth of 50 MHz. The output voltage of the APD is fed into the lock-in amplifier, where the optical signal is demodulated at the difference frequency $f = f_s - f_c$, where f_s *and* f_c = 330 kHz are the oscillation frequencies of the nanomechanical resonator and tapping mode AFM cantilever. In our previous work, we demonstrated that demodulating the optical signal at the difference frequency allows for elimination of unwanted background scattering [56]. The lock-in amplifier is operated

with an integration time of 300 μs, corresponding to a detection bandwidth of 0.78 KHz, which allows for rejection of electronic noise. Since the photothermal laser source irradiates the sample surface continuously over the integration time of the lock-in amplifier, the intensity of the amplified laser source is kept low to avoid ablating the sample. A small percentage of the AFM cantilever drive voltage and the output voltage from a high frequency (1 GHz) photodetector that samples a portion of the amplified intensity modulated laser, is combined in an electronic mixer, and the low frequency output at Δf is fed into the lock-in amplifier as a reference input. The in-phase and quadrature components of the lock-amplifier output at the difference frequency are recorded over the frequency range of interest and the data is delivered to a computer using a Labview computer program.

4.3 Tip Sample Interaction

The local detection of mechanical vibrations by the plasmonic nanofocusing probe relies on the modulation of the LSP enhancement in the gap between the probe-tip and the sample surface. However, in the far-field, other signal contributions such as the un-modulated background light scattering can also be recorded alongside the LSP scattering. We examine these contributions to the total measured signal by modifying an analytical model that describes the effect of vertical probe-tip modulation on the far-field optical signal recorded in near-field scanning optical microscopy (NSOM), developed previously by Walford et. al. [57]. In the model, the time dependent intensity of the evanescent LSP scattering recorded in the far-field is described by,

$$I_{nf} = I_0 \exp\big(-2z(t)\big)/D) \tag{4.1}$$

where, I_0 is the amplitude of evanescent optical signal, D is the decay length of the LSP within the tip-sample gap, t is the time variable, and z is the vertical gap width, which depends on relative displacements of the probe-tip and sample. Suppose the probe-tip modulation frequency and oscillation amplitude are f_c and A_c, $z(t)$ can be expressed as,

$$z(t) = A_0 + A_c \cos(2\pi f_c t) + A_s \cos(2\pi f_s t) \tag{4.2}$$

where, A_0 is a fixed offset distance, A_s and f_s are sample vibration amplitude and frequency. Typically, in a tapping mode AFM measurement, A_0 and A_c are equal to the AFM cantilever set-point. The oscillation amplitude of the nanomechanical resonator depends on the input power of the laser source, for our case, the amplitude is close to 0.1 nm, verified through interferometeric measurements and is in good agreement with existing photothermal measurements [58,59]. The diffracted light from the sample and the AFM cantilever provides a background electric field $E_b = |E_b|\exp(i\emptyset)$, where $\emptyset$ is a constant phase difference between the background and the evanescent LSPs scattered to the far-field. For convenience, we assume that the intensity and phase of the background is constant and independent of position on the sample. Using the expressions for the contributing fields, the total far-field intensity $I(t)$ is given by,

$$I(t) = \left|E_{nf} + E_g\right|^2 = I_0\left(\frac{I_g}{I_{nf}} + \exp\left(-\frac{2z(t)}{D}\right) + 2\sqrt{\frac{I_g}{I_{nf}}}\exp\left(-\frac{z(t)}{D}\right)cos\emptyset\right) \tag{4.3}$$

The amplitude of the optical signal S recorded in the lock-in amplifier corresponds to the time-averaged quadrature component of $I(t)$ given by,

$$S\big((f_s - f_c)\big) = \frac{1}{\tau_c}\int_0^{\tau_c} I(t)\cos(2\pi(f_s - f_c)t)\,dt \qquad (4.4)$$

Where τ_c is the integration time of lock-in amplifier. For simplicity, we obtain the lock-in amplifier signal from the amplitude of the fast Fourier transform of $I(t)$ at the difference frequency f_s- f_c. Figure 4.4 shows a comparison between experimental measurements of the optical signal and the numerical calculation of the tip-sample approach. In the

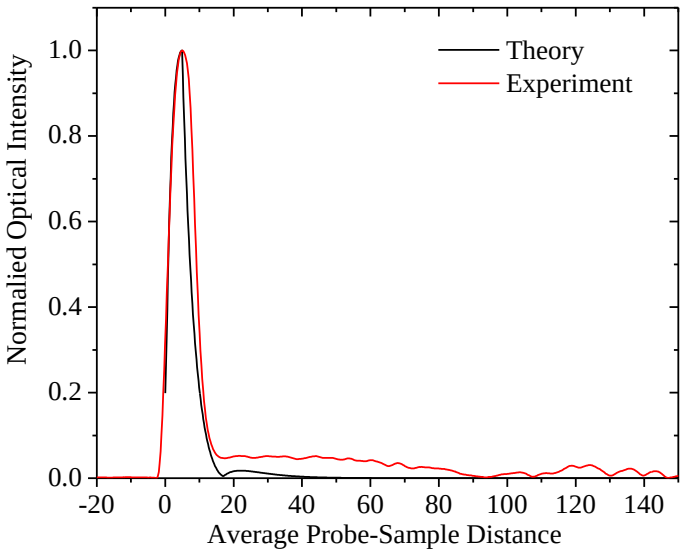

Figure 4.4 Probe-tip Approach Curve at Difference Frequency f = 20.2 MHz. The figure compares a measured and calculated probe-tip approach curves

measurement, the offset amplitude A_0 is varied from 1 μm down to 0 nm, where, A_0 = 5 nm corresponding to the beginning of the tapping mode regime at which point, A_0 is equal to A_c. In the calculation, the ratio I_g/I_{nf} and ϕ are used as free fitting parameters, D = 10 nm-

[1], estimated from the decay distance of the measured approach curve, and A_c = 5 nm, which is the AFM cantilever set point amplitude. The numerical and calculated approach curves are in good agreement, suggesting that the optical signal at the difference frequency results from the coupled probe-tip and sample interaction. The best fit parameters obtained for I_g/I_{nf} and ϕ are 0.1 and 150^0. The optical signal is enhanced close to the beginning of the tapping mode regime, and the sharp distance dependence close to the peak suggests a strong dependence of the signal on the gap distance between the sample and probe-tip and sample, within the LSP decay length of 10nm. In addition, the optical signal at the difference frequency varies linearly with the sample oscillation amplitude.

4.4 Experimental Results and Discussion

Figure 4.5(a) shows a representative measurement of the resonance spectrum of the nanomechanical resonator. In the measurement, the frequency of the photothermal source is swept in discrete steps of 0.5 MHz around the first two eigen frequencies of the resonator. The spectrum shows amplitude peaks at 20.5MHz and 56 MHz. Next, the displacement profiles at each of the frequencies are mapped with the probe-tip. The optical image of the mode shapes and a topographic image of the resonator surface are shown in Fig. 4.5(b). The data are obtained by recording horizontal line scans with 512 points per line along the sample. In the optical images, the signal is modulated by the vibration mode shape along the length of the nanomechanical resonator. Along the width of the resonator, a series of fringes are observed in the optical images with wavelengths of 230 nm and 128 nm. Using

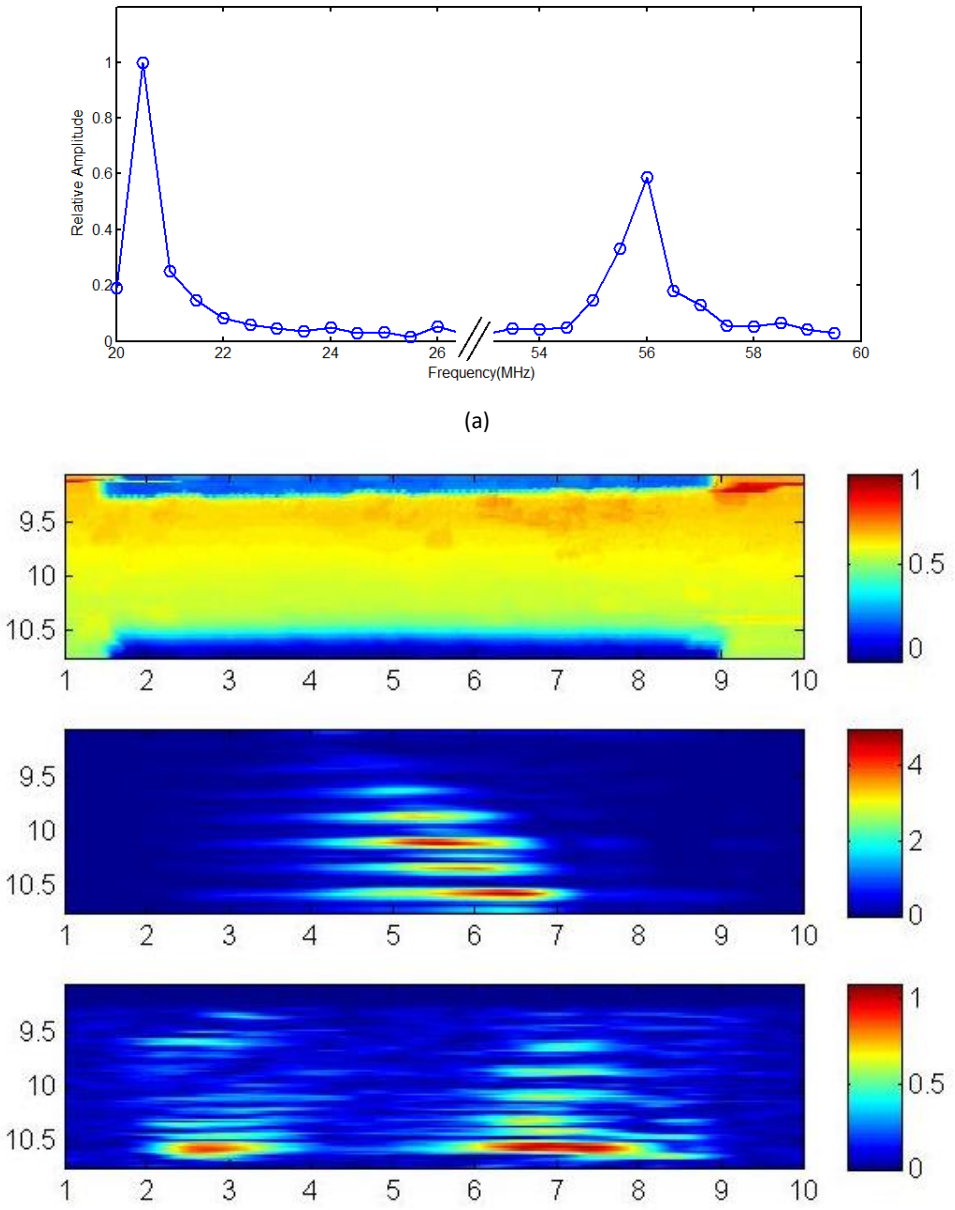

Figure 4.5 Near-field optical imaging of the probe-tip and sample interaction for a photothermally actuatued nanomechanical resonator. (a) Resonance spectrum of nanomechanical resonator measured by monitoring the modulated component of the probe-tip sample interaction at f_s-f_c, where f_c = 330 kHz, f_s is the modulation frequency of the photothermal source. (b) shows the sample topography (top), near-field optical image of the resonator displacement profile at f_s = 20.5 MHz (middle), and f_s = 56 MHz. Colorbar in the topography image is in units of micrometers. Colorbar in optical images represents a relative intensity change

an analytical model in our previous work [56], we determine that the dominate fringe pattern

is produced by interference of the incident light and the SPPs excited by diffraction of the illumination source from the sample edge. The corresponding fringe wavelength is given

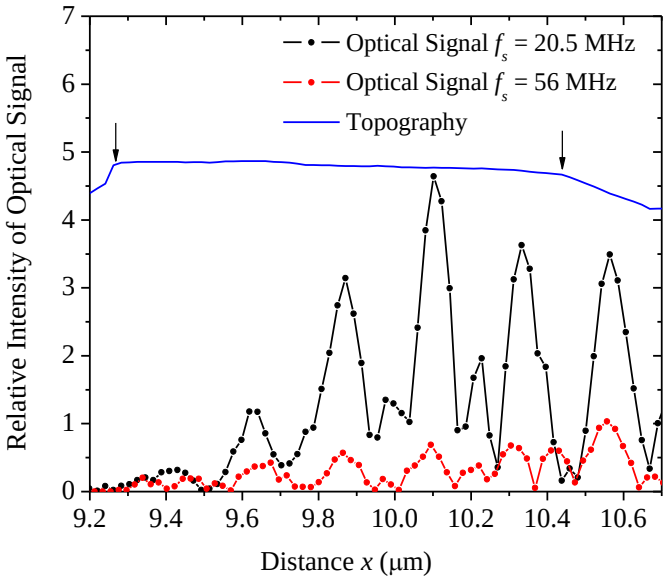

Figure 4.6 Comparison of line scans of the optical signal across the resonator to the topography. The space between the vertical arrows in the topography corresponds to the top surface of the resonator.

by the following expression, $\frac{2\pi}{(3k_{sp,y}-kcos\theta)}$ = 230 nm, being related to the wave vectors of the illumination source and SPPs propagating on the chromium film, k and k_{sp}, and θ = 39^0, which is the illumination angle with respect to the sample surface. The weaker fringe pattern is produced by interference of reflections of the probe-tip excited SPPs from the edges of the nanoechanical resonator, with wavelength of $\frac{\pi}{2k_{sp,y}}$ = 128 nm. The SPPs wave vector is obtained from the dispersion relation, $k_{sp} = \frac{w}{c}\sqrt{\frac{\varepsilon_m \varepsilon_d}{\varepsilon_m+\varepsilon_d}}$, where w is the illumination light frequency, c is free space phase velocity of light, ε_m and ε_d are the

electric permittivity's of the dielectric and the metal film. We remark that the fringes are not observed in the topography, and are consistent in the two optical images. We compare the average of several line scans taken across the width of the resonator in Figure 4.6, where the fringes in the optical images obtained at the two sample modulation frequencies are well correlated. The space between the two arrows in the topography line scan corresponds to the top surface of the resonator. The amplitude of the optical signal appears to be enhanced close to the side edge of the resonator, i.e., x = 10.6 μm, due to edge diffraction of the incident light to SPPs. In addition, the ratio of the maximum fringe amplitudes at 20.5 MHz and 56 MHz is approximately six, which is due in part to the efficient photothermal actuation of the fundamental vibration mode compared to the second mode, due to the large spot size (diameter ~ 6 μm) of the intensity modulator laser.

Finally, we compare several lines scans of the optical signal along the length of the resonator to the eigen mode shapes of a doubly clamped Euler-Bernoulli beam [20], in Fig. 4.7. Due to coupling of the incident light to SPPs, and the interference fringes on the sample surface, the optical signal along the resonator length is not uniform. We note the interference fringes are influenced by the surface roughness of the sample. In general, the optical signals agree qualitatively with the calculated mode shapes, however, the optical signals are distorted, particularly close to the side of the resonator where interference fringes have the largest intensity. The distortion also results from the complicated diffraction pattern around the sharp bottom corners of the resonators. At the center of the

nanomechanical resonator, we compare the ratio of maximum optical signals along the

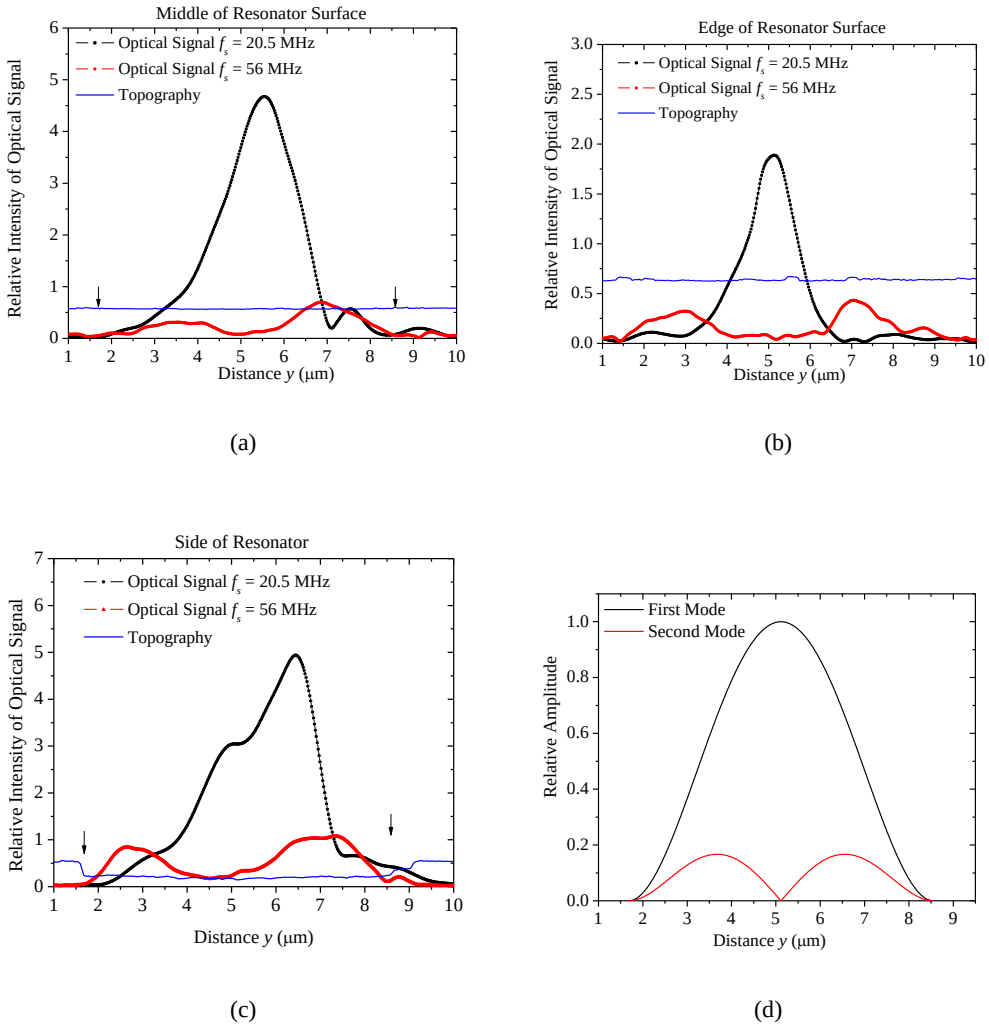

Figure 4.7 Optical profiles of the mode shapes of the nanomechanical resonator. Line scans of the sample displacement profiles at 20.5 MHz and 56 MHz obtained at the middle of the resonator (a), one edge on the resonator surface (b), and at the side of the resonator (c). The space between the arrows in the measured data corresponds to the position of the fixed supports or clamps. (d) shows the absolute value of the calculated mode shapes for the first two vibration modes based on the Euler-Bernoulli model for a doubly-clamped beam.

resonator and the pads (or fixed ends), and we obtain a signal-to-background ratio of 61

for the 20.5 MHz signal, and 9 for the 56 MHz signal. In both cases, the peak optical signals are stronger than the noise floor. While the presence of interference fringes may present a challenge to accurate profiling of the resonator mode shapes, we do not expect to find these fringes in nanomechanical resonators with widths that are smaller than the SPP wavelength.

4.5 Conclusion

We have integrated a harmonic modulated photothermal source with the plasmonic nanofocusing probe, allowing for an all optical actuation and transduction of the steady state vibration of a nanomechanical resonator in the frequency domain. In the measurement approach, the nanomechanical resonator is actuated at a fixed frequency f_s and the probe-tip is oscillated harmonically at frequency f_c. We track the local sample surface displacement by monitoring the nonlinear dependence of the local optical field enhancement with separation distance between the probe-tip and resonator surface, In particular, we demodulate the far-field optical scattering at the difference frequency f_s-f_c in a lock-in amplifier, and show that the measured signal is strongly correlated with the sample displacement. The operational frequencies of the measurement approach can be seamlessly extended to the GHz range, which is particularly attractive for probing motion in nanomechanical resonators with smaller widths compared to the SPP wavelength.

Chapter 5 Near-field Photothermal Heating with a Plasmonic Nanofocusing Probe

5.1 Introduction

The interaction of light with noble metal nanostructures can lead to strong confinement and enhancement of light in the near-field- within a distance of fractions of the optical wavelength from the structure. Local confinement of optical energy is achieved through resonant coupling of free-space propagating light to surface plasmon polaritons (SPPs) using various structural geometries including nano-rods, particles, pillars, etc. To explore plasmonic structures as nanoscale optical probes, it is crucial that the efficiency of the far-field to near-field coupling is optimized, and the influence of background scattering is minimized. Furthermore, the compatibility of the probe with existing scanning probe microscopy instrumentation is desirable. One approach to achieve these requirements is based on a hybrid nanofocusing scheme, where free space light is coupled to propagating SPPs on a tapered metallic scanning probe. Due to adiabatic tapering of the scanning probe, the SPPs propagate towards the probe tip with gradually decreasing group velocity, resulting in strong energy concentration and local field enhancement at the tip apex, with minimal non-ohmic losses [60-62]. Unlike the resonant coupling of light to plasmons, the use of propagating SPPs requires the use of spatial experimental geometries, such as Bragg diffraction grating couplers, to match the phase of far-field propagating light and the excited SPPs. If the probe-tip is positioned within the near-field of a sample, the plasmonic

nanofocusing probe can be used in the illumination or scattering mode. In the former, localized surface plasmons (LSPs) at the probe-tip apex provide a bright nanoscale optical source, and in the scattering mode, evanescent optical fields on a sample are scattered by the probe-tip to the far-field as propagating waves. The plasmonic nanofocusing probe has been explored in broad application areas including, background free super-resolution optical imaging [63,64], tip-enhanced Raman spectroscopy (TERS) [65], near-field photoelectron microscopy [66], spatial and temporal control of femtosecond optical sources for local second harmonic generation [67], and near-field optical transduction of nanomechanical motion [56], and ultrasonic waves [68].

The strong confinement of LSPs at the probe tip can lead to significant heating of the tip and a sample positioned in the optical near-field, which can serve as a local photothermal or photoacoustic source. Indeed, it has been shown that a directly illuminated metallic probe tip can induce considerable local sample temperature rise, of greater than 100 degrees at modest input laser energies [69]. Using the TERS geometry, the local sample temperature rise is quantified directly based on the ratio of the Stokes and anti-Stokes component of the near-field Raman scattering [69], or indirectly based on a calibrated curve of Stokes frequency shift with temperature [70]. The temperature dependence of the Raman scattering frequency is results from anharmonic terms in the vibration potential energy of material [71]. Interestingly, there is no reports in the literature that address local heating

effects induced by the plasmonic nanofocusing probe, although the optical field confinement and enhancement is expected to be stronger than the case of a directly illuminated metallic probe tip. In this chapter, we demonstrate that the plasmonic nanofocusing tip can be used as a local heat source. We perform a TERS experiment in multiwall carbon nanotubes and silicon substrates and use the frequency of the Stokes scattered light to quantify the magnitude of the temperature rise produced by absorption of LSPs coupled to the sample in the near-field. The TERS experimental configuration is ideal for several reasons; first, the Raman spectra in the samples have been widely studied in the literature [72,73], and, second, the intensity of the Stokes component of the near-field scattering is greatly enhanced by the strongly confined LSPs electric field at the probe-tip. In addition, we perform three dimensional (3D) finite element modeling of local sample heating under different probe-tip illumination conditions, and good qualitative agreement between the numerical and experimental results are obtained. Understanding the relative strengths of the sample heating obtained under different probe-tip illumination conditions would facilitate design of the plasmonic nanofocusing probe for fundamental studies of nanoscale heat transport in materials and related applications in nanoscale heat assisted fabrication.

5.2 Experimental Setup

Figure 5.1 shows the schematic of the reflection mode TERS experimental setup. The plasmonic nanofocusing probe is integrated with a commercial AFM (Innova AFM).

Details of the probe-tip fabrication and processing approaches, and the tapping mode operation in the AFM have been discussed before. In the TERS experiment, the AFM is

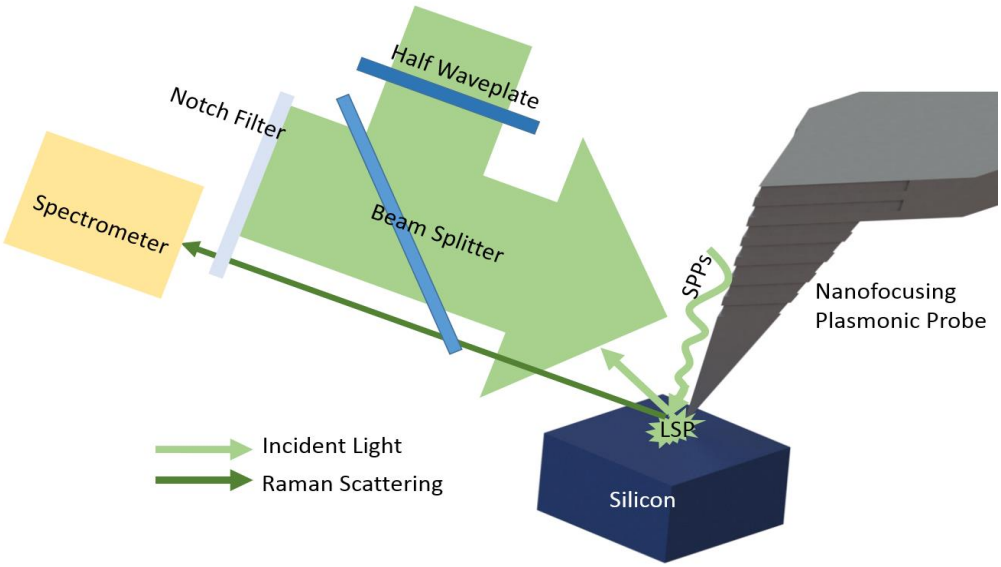

Figure 5.1 Schematic of experimental setup. The incident laser of 532nm wavelength passes through a beam splitter, and is focused on a diffraction grating on probe facets by 10 X microscope objective. The excited SPPs propagate towards tip apex, and are adiabatically converted to localized surface plasmons at the probe-tip, creating a nanoscale optical source. The excited Raman scattering and Rayleigh scattering signal both travel along the same optical path, while only the Raman scattering signal passes through the notch filter, and is detected by the spectrometer.

operated in contact mode. A *p* polarized continuous wave laser with a wavelength of 532 nm is focused on the diffraction grating on the probe facets by a 10x microscope objective with a numerical aperture of 0.3. An optical microscope that is integrated with the AFM is used to observe the position of the focused laser spot. The scattered light from the sample is collected by the 10x objective and directed through a notch filter designed to seperate the elastic and inelastic components of the light scattering. The output of the notch filter is

detected by a spectrometer equipped with a liquid nitrogen-cooled charge coupled device (CCD). The maximum resolution of the spectrometer is 1 cm^{-1}. The spectrometer is operated with an integration time of 300 s to reject broadband noise.

5.3 Tip Enhanced Raman Scattering in Multi-walled Carbon Nanotubes

First, we demonstrate an enhanced Raman scattering resulting from LSPs at the plasmonic nanofocusing probe tip. For this purpose, a dispersed MW-CNT film on glass substrate is used. The Raman spectrum of CNTs have been widely studied using the TERS. The radial breathing mode, which occurs in the range of 100-400 cm^{-1} depends on the diameter and chirality of the CNT [74]. The tangential stretching G band vibration mode close to 1590 cm^{-1} can be used to distinguish semiconducting and metallic singled walled CNTs [75], and the disorder-induced D band mode close to 1350 cm^{-1} depends on the presence of defects in the nanotube structure [76]. For the experiment, the power of the far-field illumination source is limited to 2 mW. The near-field and far-field Raman spectra are obtained by engaging the probe-tip in contact with the sample and disengaging it, respectively. By adjusting the polarization of incident light parallel to the axis of the probe-tip, a maximum Raman intensity is obtained due to strong coupling of far-field light to LSPs. The difference between the near-field and far-field illumination conditions stem from the local intensity and spot size of light at the incident frequency. Figure 5.2(a) shows

the measured spectra around the G band peak. The ratio of the near-field (I_{TERS}) and far-

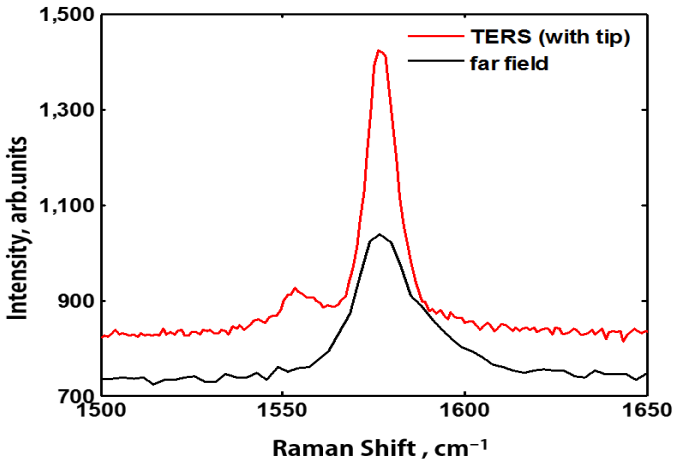

(a)

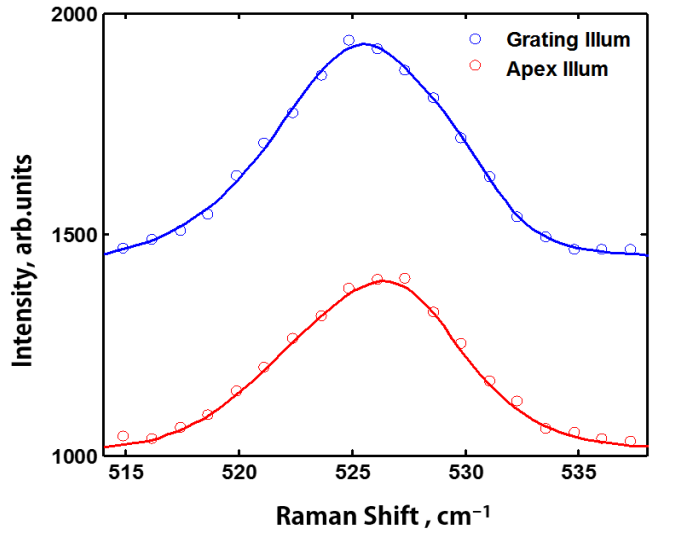

(b)

Figure 5.2 Tip Enhanced Raman Scattering in Multi-walled Carbon Nanotubes and silicon samples
(a)Raman spectra of MW-CNT film on glass substrate using the plasmonic nanofocusing probe tip.
(b)Raman spectra of silicon sample with different laser illumination conditions. The solid line are the Gaussian fittings for determination of the Raman peak position.

field (I_{FF}) Raman scattering intensity is approximately 1.4, which suggests a modest

enhancement in the Raman scattering when the probe-tip is in contact with the MW-CNTs. Furthermore, the G band spectrum from the TERS measurement is split into primary and secondary peaks, which is consistent with published measurements in the literature [74, 75]. The I_{TERS}/I_{FF} ratio depends on the enhancement of the incident and scattered electric fields by the probe-tip, and following established methods in the literature. [76], .we estimate the TERS enhancement *M* by the plasmonic nanofocusing probe as, $M = \frac{A_{FF}}{A_{NF}} \times \frac{I_{TERS}}{I_{FF}}$, where A_{FF} and A_{NF} are the areas of the far-field focus and the near-field enhancement region. A near-field localization of approximately 10nm is estimated from the tip-sample approach curve [56, 64], the far-field focus is assumed based on the diffraction limited focused spot size, and as such, we estimate $\frac{A_{FF}}{A_{NF}}$ to be approximately 10^4 and *M* is ~ 1.4×10^4. The corresponding electric field enhancement enabled by the plasmonic probe approximately $M^{1/4}$ = 11.

5.4 Local Heating of a Silicon Substrate

Next, we investigate the local heating of a silicon substrate for two different probe-tip illumination conditions. In one case, the probe-tip apex is directly illuminated and in the other, the SPP coupling grating is illuminated allowing for excitation of LSPs based on adiabatic nanofocusing. We chose the silicon substrate for this experiment because of its low thermal conductivity in comparison to MW-CNTs, allowing for local local heat buildup under the probe-tip that can induce large frequency shifts in the TERS spectrum. In addition,

the temperature dependence of the Raman spectra in silicon has been widely studied [70, 71], and for moderate sample temperatures in the range of 300-600 K, the magnitude of the frequency shift of the Stokes component of the Raman scattering decreases linearly with temperature, with a slope of between -0.02 to -0.03 cm^{-1}/K. Figure 5.2(b) shows the TERS spectra obtained in an undoped silicon sample for the two different probe illumination conditions. The measured spectra are fitted with Gaussian functions in order to accurately determine the frequency of Raman peaks. In both cases, the frequency of the Raman shift is close to 525 cm^{-1}. We remark that the Raman peak was not observed in the MW-CNT spectrum, which suggests that the TERS signal from the silver coated silicon AFM cantilever probe is below the noise floor of the measurement system. The peak positions of the TERS signals are slightly shifted by approximately 2.5 cm^{-1}, which corresponds to a temperature rise of between 83 to 125 degrees due to plasmonic nanofocusing in comparison to the direct probe-tip illumination.

5.5 Numerical Simulation

In order to better understand the local tip-sample heating using the plasmonic nanofocusing probe, we employ a 3D finite element method (FEM) to obtain numerical solution to Maxwell's equation for the electromagnetic field distribution at the probe-tip. The simulated optical near-field in the silicon sample can be used as input source to the classical heat equation in order to calculate the temperature rise in the sample. The plasmonic

nanofocusing probe is modeled as a silicon tetrahedron coated with a silver film. The tip apex is modeled as a hemisphere with a radius of curvature of approximately 20 nm. The thickness of the silver film is 200 nm at the beginning of the tip shaft and it is gradually reduced to 30 nm at the tip apex. A one-dimensional Bragg grating with a period of 667 nm is introduced at the upper portion of the probe to couple the incident light to SPPs. The distance between the end of the grating and the probe-tip is 7 μm. The grating is illuminated by a *p*-polarized plane wave with at an incident angle of 15° with respect to the normal line of tip shaft. The dielectric constants for the silver film and the silicon used in the numerical model are $\epsilon_{Ag} = -11.7 + 0.35i$, and $\epsilon_{Si} = 17.433 + 0.077i$ respectively. Scattering boundary conditions and perfectly-matched layers are applied to the external domain in order to obtain numerical solutions to the electromagnetic wave equations. In the numerical simulation, one side of the plasmonic probe is illuminated by the laser source. Figure 5.3(a) shows the electromagnetic field distribution along the tapered region of the probe and close to the probe-tip. A bright contour is observed along the illuminated side of the plasmonic probe due to the excited SPPs, and the close-up view of the probe-tip in Fig. 5.3(b) shows strong confinement and enhancement of optical field. The localized optical field irradiating the silicon substrate has a spatial extent of approximately 30 nm. To compare relative strengths of the optical field enhancement for the tip apex illumination and the grating illumination conditions, the illuminated region on the probe is moved from the tip apex to the diffraction grating. The spot size (diameter) of the illumination source

is 4 μm. Figure 5.3(c) shows the numerical estimates of the intensity at the center of the probe-tip, where the 0-2 μm region corresponds to the tip apex illumination configuration

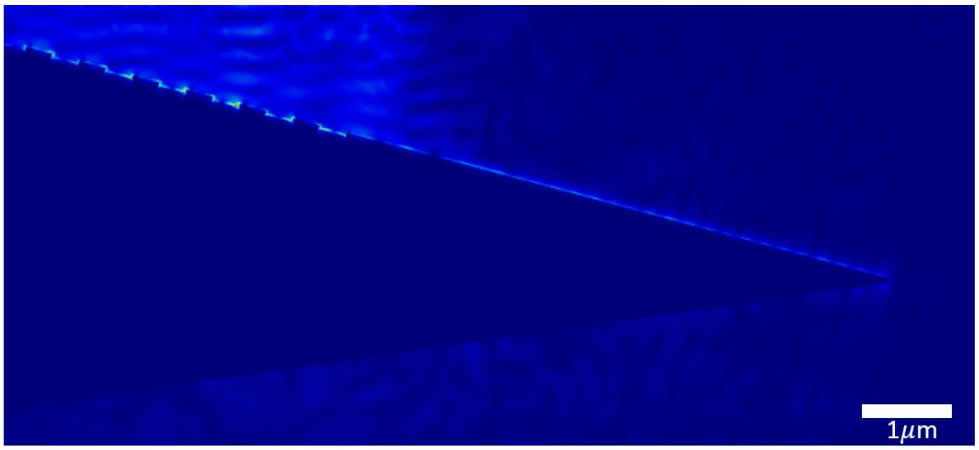

(a)

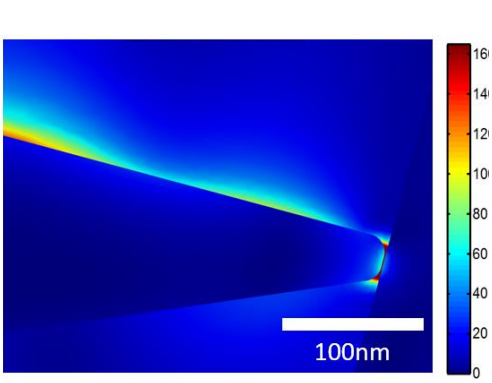

(b)

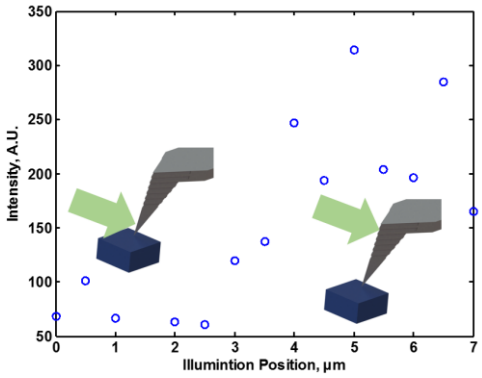

(c)

Figure 5.3 Numerical simulation of local tip-sample heating using the plasmonic nanofocusing probe
(a) Electromagnetic field distribution of the whole modeling structure.
(b) A zoomed view of the optical field in the vicinity of the probe-tip and the silicon sample.
(c) Comparison of the field enhancement between the tip apex illumination and the grating illumination. The 0-2 μm region corresponds to the tip apex illumination configuration and the 4-7 μm region represents the grating illumination, respectively.

and the 4-7 μm region the only the grating is illuminated, respectively. The ratio of the average LSPs at the probe-tip between the two regions in the figure is approximately 2.7,

suggesting that the grating illumination configurations is a more efficient approach to couple far-field illumination to LSPs. Finally, the coupling between the local optical field and the temperature rise in the sample can be addressed using the heat equation. Considering the case optical absorption near the surface of the silicon substrate, the solution to the classical heat equation for a continuous heat source is trivial, $T(r) = \frac{\int \alpha I dV}{4\pi k \mathrm{r}}$, where T is the temperature rise, r is the distance variable in spherical coordinates, α and k are the sample absorption coefficient and thermal conductivity, and I is the local optical intensity distribution within the volume V in the sample. Since the local sample temperature is directly proportional to the absorbed intensity, one can expect the grating illuminated probe will produce a larger sample temperature rise. We remark the true nature of the sample heating may be more complicated than the simple model considered here, particularly in the case of an ultrafast laser source. Other effects such as heat conduction between the Joule heated plasmonic nanofocusing probe and the substrate, and nonlocal ballistic effects [78] may also be contributing factors.

5.6 Conclusion

In summary, we have performed preliminary studies on near-field photothermal heating using a plasmonic nanofocusing probe. We explored the TERS experimental configuration to correlate the shift of the Stokes frequency for the inelastic scattered light from a silicon substrate, with local sample heating. By comparing two excitation conditions, i.e., direct

probe-tip apex illumination, and grating coupled LSPs, we observed a larger shift in the Stokes frequency for the grating illuminated probe. We estimate that the difference between the local sample temperature rise for the two illumination conditions is between 83 to 125 degrees. Furthermore, we confirmed the measured results using finite element modeling to obtain numerical solutions to the electromagnetic wave equation for far-field optical excitation of LSPs. Further work is needed to understand complex multiphysics involved in local heating of the sample by the proximal nanofocusing probe. Nevertheless, the experimental results suggests if these physics of the heating process can be well understood and controlled, the plasmonic nanofocusing probe can be a promising tool for local photothermal heating of nanostructures, fundamental studies of nanoscale heat transport in materials, and heat assisted nanofabrication.

Chapter 6 Near-field Optical Detection of Ultrafast Acoustic Vibrations of Individual Gold Nanodisks

6.1 Introduction

Metallic nanostructures are characterized by strongly confined and enhanced near-field optical energy and they have the ability to mediate fast conversion of light to phonons on picosecond time scales [79-84]. These characteristics have significant implications on broad fields including, photodynamic therapy [84-86], photoacoustic and photothermal sensing [87, 88], energy conversion [89-91], optofluidics [92, 93], etc. Furthermore, the possibly of tuning the optical field enhancements in metallic nanostructures through geometric and mechanical degrees of freedom makes them ideal candidates for reconfigurable nano-optomechanical metamaterials [94]. In this case, the local electromagnetic fields between individual nanostructures in a metamaterial can be independently controlled in space and time, leading to ultrafast switchable optical metamaterials [95], GHz acousto-optical modulators [96], and coupled nano-plasmonic and phononic sensors and filters [97-99]. To facilitate these developments, advanced sensing methods that provide access to extreme time (picoseconds) and spatial (nanometer) scales are needed to facilitate unprecedented understanding of various phenomena- optical confinement, local heating, mechanical deformation, and energy dissipation, in the metallic nanostructures.

Ultrafast pump and probe techniques like the transient absorption spectroscopy [100] and picoseconds ultrasonic methods [101] have been extensively used to investigate the dynamics of laser excited metallic nanostructures. In these techniques, optical excitation of the localized plasmon resonance (LSP) – collective oscillation of conduction band electrons, with an ultrafast pump laser leads to a large absorption cross section, impulsive generation of hot electrons. The electrons couple their energy to the lattice through electron-phonon collisions leading to thermoelastic generation of coherent acoustic vibrations that modulate the geometry of the nanostructure on a picoseconds time scale. The mechanical strain induced by the lattice vibrations and the change in the size of the nanostructure leads to a shift in the LSP frequency. Thus, the lattice vibration is monitored by monitoring the intensity change of a probe-laser whose wavelength is close to the LSP resonance, in the transmission or reflection modes. The transient absorption spectroscopy and picoseconds ultrasonic methods have used to explore to advance the general understanding of hot electron dynamics, and acoustic phonon vibrations of metallic nanostructures, from which size dependent elastic properties and energy exchange with the environment have been elucidated. Majority of these studies have been performed on ensembles of nanoscale objects [102, 103] or lithographically fabricated nanostructures separated from each other by distances larger than the optical diffraction limit [104-106]. However, recently there is significant interest in understanding the local interactions between coupled plasmonic nanostructures separated by nanoscale gaps [97-99, 107, 108]

for enhanced sensing applications, and by extension their opto-mechanical coupling, while avoiding ensemble averaging effects. Herein is where majority of the ultrafast pump probe methods are limited due to their large optical footprint stemming from the optical diffraction limit.

In this work, we incorporate a sharp metallic probe-tip in contact with the sample into a picoseconds ultrasonic setup to make spatially and temporally resolved measurements of the transient reflectivity changes on a plasmonic nanodisk array. The metallic tip is employed to channel evanescent electromagnetic waves in a nanometer sized gap between the tip and sample to the far-field. In a recent work, we demonstrated the ability to resolve local acoustic vibrations in nanomechanical resonators in the MHz range with a displacement sensitivity of 0.5 pm/Hz1/2 , a lateral spatial resolution of the order of 20 nm, and free of unwanted background scattering [56], using a related approach. Here, we obtain what is to the best of our knowledge, the first experimental demonstration of time resolved transient thermoreflectance measurements showing the acoustic phonon vibrations of plasmonic nanoscale disks at frequencies in the tens of GHz range. The spatial measurement of the transient thermoreflectance response on individual nanodisks is strongly correlated with the locally enhanced electric field distribution close to the sample boundary. These measurements suggest that the experimental approach can enable accurate mapping of local plasmon and phonon modes of individual and coupled metallic

nanostructures, thus enabling further studies of optomechanical interactions in nanoscale metallic objects.

6.2 Sample Fabrication and Characterization

The sample consists of a periodic array of gold nanodisks on a glass substrate, fabricated by electron-beam lithography. The geometry of the fabricated nanodisks were determined from scanning electron microscopy images of the sample shown in Fig. 6.1 The disks have a nominal diameter and spacing of 130 nm and 600 nm, and the height of each disk is 50 nm. The transmission spectrum of sample was characterized in an index matched environment that consists of an oil layer with refractive index n = 1.52, covering the gold nanodisks. The refractive index of the oil layer is matched to the glass substrate. The spectrum in figure 6.2 shows a broad localized surface Plasmon resonance (LSP) trough at $\lambda_{LSP} = 730$ nm, a lattice Plasmon resonance trough at $\lambda_{L} = 900$ nm, and a small Rayleigh anomaly peak at $\lambda_{RA} = 631$ nm, which are in agreement with recent observations in two dimensional arrays of gold nanodisks on glass [109]. For the aNSOM experiments, we use a sharp gold coated silicon scanning probe tip as a near-field transducer as illustrated in Fig. 6.3(a). The aNSOM used in our experiment is based on a contact mode atomic force microscope (AFM), and the probe-tip and nanodisk are both illuminated an oblique angle with a p-polarized probe laser. Figure 6.3(b) and (c) shows finite element numerical simulations (COMSOL Multiphysics) of the electric field distribution on top of a 130 nm

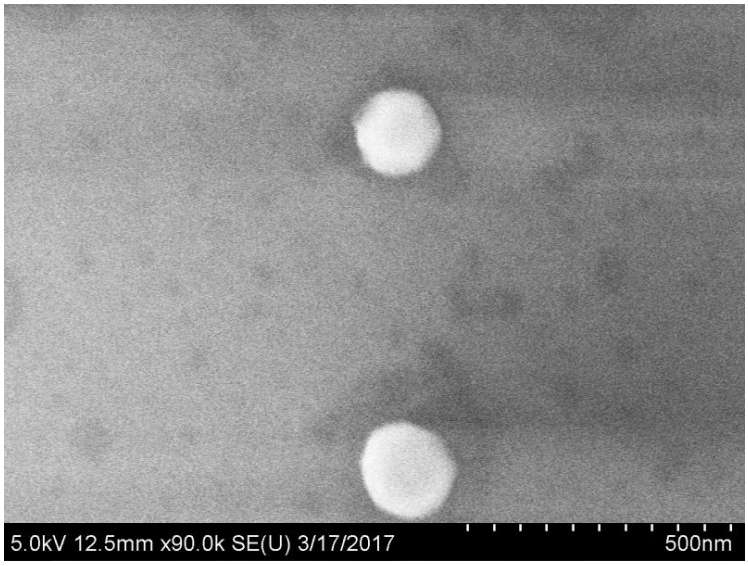

(a)

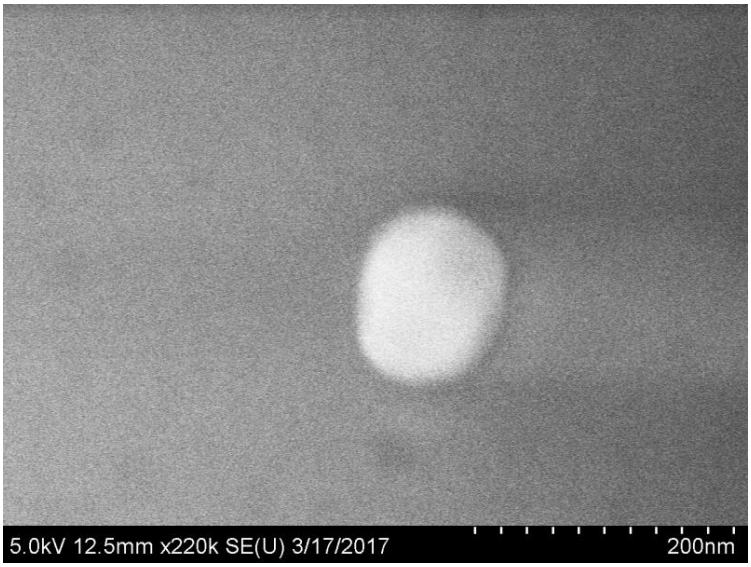

(b)

Figure 6.1 Scanning electron microscopy picture of the gold nanodisks (a) Low magnification picture (b) High magnification picture

diameter gold nanodisk on a glass substrate, in the absence and presence of the probe tip

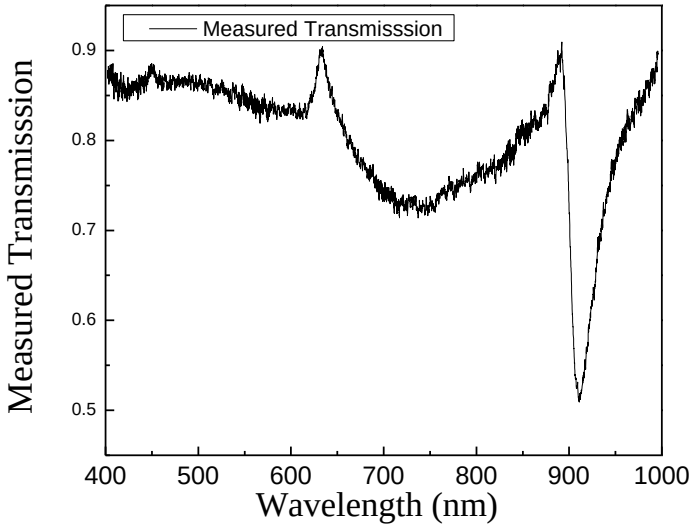

(a)

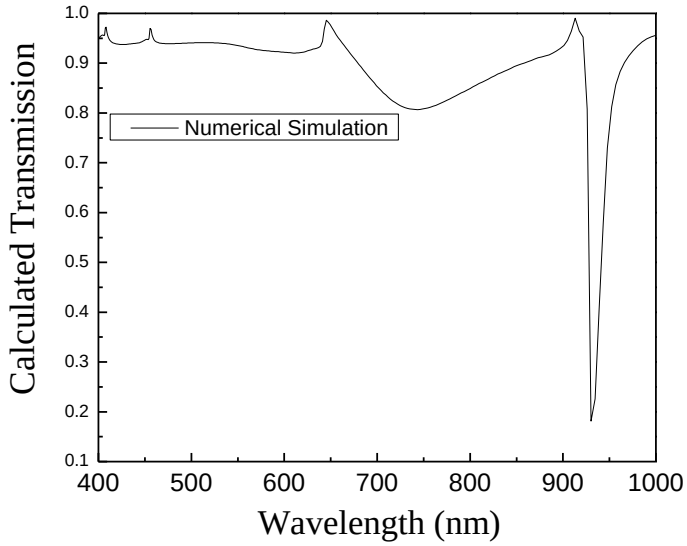

(b)

Figure 6.2 Optical characterization of the gold nanodisks. (a) Measured transmission spectrum (b) Simulated transmission spectrum of gold nanodisks having the same dimensions.

for an illumination wavelength of 780 nm, which is close to the LSP resonance. In Figs 6.3

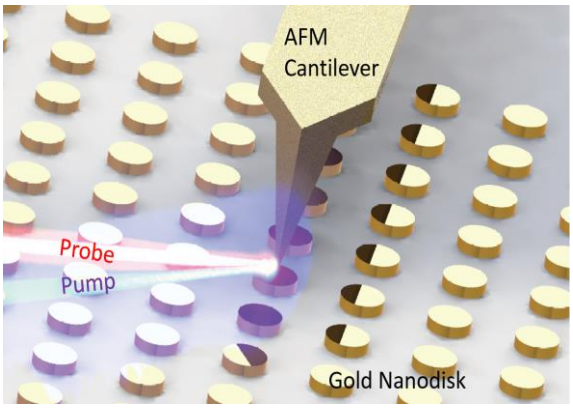

(a)

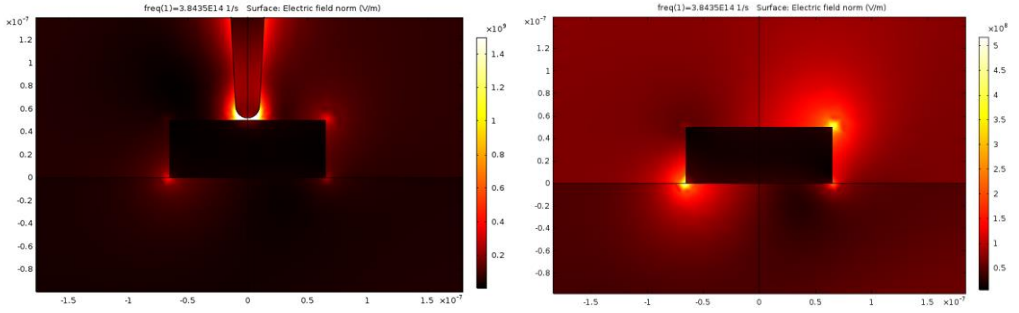

(b) (c)

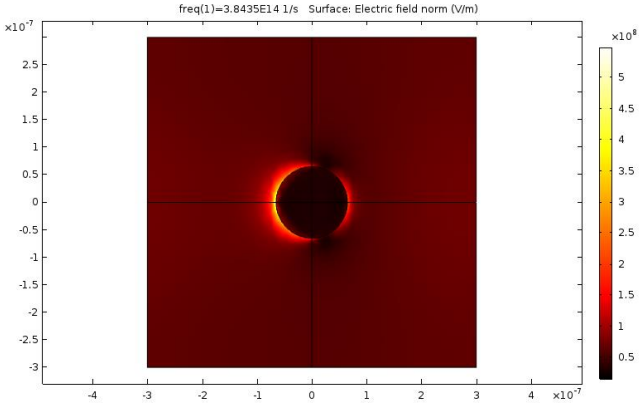

(d)

Figure 6.3 (a)Artistic picture of the two color pump probe scattering type near-field microscopy. Both pump (purple color) and probe (red color) beams are focused on the apex of an aNSOM probe. (b), (c) Finite element numerical simulations of the electric field distribution on top of a 130 nm diameter gold nanodisk on a glass substrate, in the absence and presence of the probe tip for an illumination wavelength of 780 nm. (d) Top view of the electric field distribution of a 130nm diameter gold disk.

(d), the dipolar localized plasmon resonance mode is observed [110]. However, the presence of the probe-tip above the sample creates a stronger localized field between the probe-tip and the disk, than the near-field intensity at the edges of the disk [111]. The asymmetry in the electric field intensity around the disk is due to the oblique illumination angle of the input electric field. The near-field coupling between the probe-tip and the disk and the localized plasmon field around the disk edges will be modulated by the acoustic vibration of the disk. Our measurement consists of monitoring the scattered light from the tip-disk interaction in the far-field as the probe-tip scans over the disk. Since the transient acoustic response of a nanodisk, resulting from illumination with an ultrafast pump laser is much faster than response time of commercial detection methods, the sample response is recorded by the time-domain spectroscopy approach.

6.3 Experimental Setup

6.3.1 Near-field Detection

A schematic of the experimental setup is shown in Fig. 6.4(a). A two color pump and probe technique is used to excite and detect the acoustic vibrations of the gold nanodisks. In the setup, a Ti:sapphire mode locked laser with a central wavelength of 780 nm and pulse duration of 150 fs and pulse-to-pulse repetition frequency of 80 MHz, is split into pump and probe beams by a combination of a half wave plate and a polarizing beam splitter. The frequency of the pump laser is doubled by transmission through a Barium Borate (BBO) second harmonic generation (SHG) crystal, such that the output wavelength of the pump

laser is 390 nm. The pump laser is directed through an acousto-optic modulator (AOM)

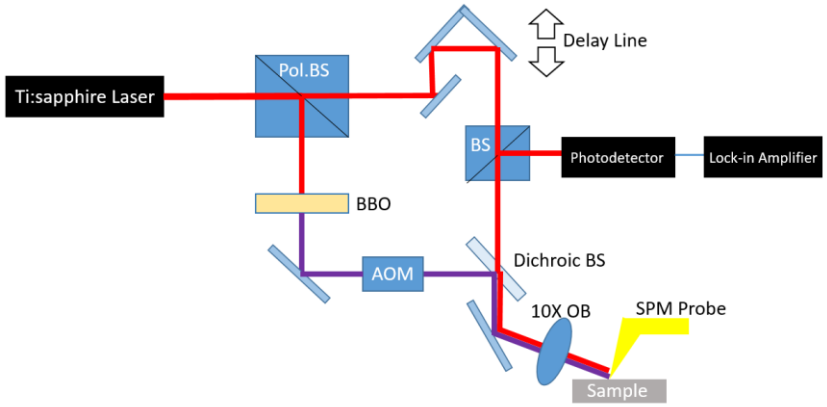

(a)

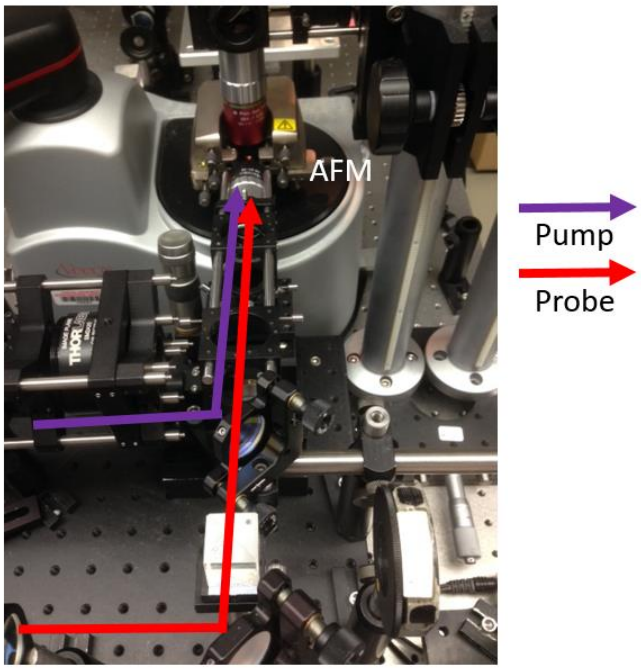

(b)

Figure 6.4 Experimental Setup (a) Schematic of the experimental setup (b) picture of the optics and AFM head.

and the transmitted intensity is modulated at a frequency fAOM = 0.3 MHz. The probe laser at 780 nm is reflected from a retroreflector mirror mounted on a linear motorized

translation stage for controlling the time delay between the probe and probe lasers. The reflected probe and the pump lasers are focused at oblique incidence angle of 18 degrees through a 10x microscope objective with a numerical aperture of 0.3 to small spot sizes on the sample surface. The spot sizes of the pump and probe lasers on the sample are approximately 32μm and 6 μm. A gold coated contact mode AFM probe-tip is positioned directly over the illuminated pump and probe lasers. As such, the probe-tip and sample surface are partially illuminated by the pump and probe lasers. The contact mode AFM cantilever has a spring constant of 0.3 N/m and a free resonance frequency of 16 kHz. In order to avoid potential damage to the AFM cantilever, the average power of the pump and probe lasers are limited to 6 mW and 1 mW. The scattered probe light from the probe-tip and sample interaction is collected by the 10x microscope objective and directed to a low noise photodetector with bandwidth of 150 MHz. A notch filter with a transmission peak around 780 nm is placed in front of the photodetector to reject the scattered pump light. The voltage output of the photodetector is demodulated in a radio frequency lock-in amplifier at the pump laser modulation frequency f_{AOM}. The reference input voltage to the lock-in amplifier is obtained from the function generation used to excite AOM. In order to record the thermal and acoustic response of the sample response following the ultrafast pump laser illumination, the time delay between the pump and probe beams illuminating the sample surface is changed by adjusting the path length of the two beams using the linear translation stage as shown in Fig. 6.4 For each value of time delay, the in-phase and

quadrature components of the photodetector voltage is recorded by averaging the photodetector output from multiple pump laser firing events. To optimize the signal-to-noise ratio of the measurement, an integration time of 3s was chosen. In addition, the input polarization of the probe laser is adjusted to optimize the signal strength by installing a half wave plate after the beam linear translation stage.

6.3.2Far-field Detection

We compared the transient response of the sample obtained with the near-field probe to far-field measurements. For these measurements, the sample is illuminated at normal incidence through a 20x microscope objective with a numerical aperture of 0.42. The pump and probe lasers have a spot sizes at the full-width-at-half maximum intensity of about 10 μm and 2 μm. The power of the incident pump and probe lasers is 16 mW and 1 mW. The illuminating pump laser is intentionally defocused to ensure that several nanodisks are simultaneously excited by the pump laser, and facilitates the excitation of a wide range of acoustic modes including the local vibration modes of each nanodisk, and extended surface acoustic wave resonant modes from the array [105]. The reflected probe light from the sample surface is collected by 20x microscope objective and recorded at the photodetector. The output of the photodetector is fed into the lock-in amplifier and the time-resolved measurement of the sample reflectivity is recorded at different pump-probe time delays, as in the near-field detection case.

6.4 Results

6.4.1 GHz acoustic vibration of individual and ensembles of nanodisks

Far-field Measurements: Figure 6.5(a) shows the transient thermoreflectance change at different positions on the sample. The measured signal results from the perturbation of the electronic state of the gold disks by a combination of temperature changes and mechanical strain. At a pump-probe time delay close to t = 0, the pump laser excites the free electrons in the gold nanodisks leading to a sharp change in the sample reflectivity. The electrons thermalize within a short time scale (less than 1 ps), and their energy is transferred to the lattice by electron-phonon collisions, leading to heating and thermal expansion of the gold nanodisks and the glass substrate. The heating process produces a corresponding change in the refractive index of the gold disks and a time dependent change in the sample optical reflectivity. Furthermore, the transient thermal expansion of the gold disks lead to excitation of their vibrations modes, which lead to a strain induced change in the optical reflectivity of the sample. The vibration modes perturb the band structure of the plasmonic nanoantennas leading to modulation of the LSP resonance frequency, which for a fixed probe laser wavelength, results in a corresponding modulation of the probe laser intensity. The relative reflectivity change $\Delta R/R$ for the measured waveforms is on the order of 10-4. Since the pump and probe beams are larger than the size of an individual nanodisk, the

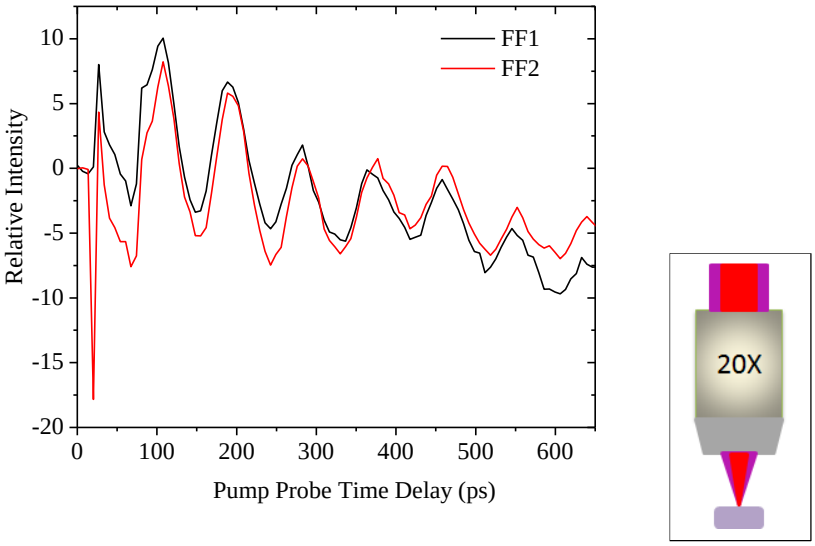

(a)

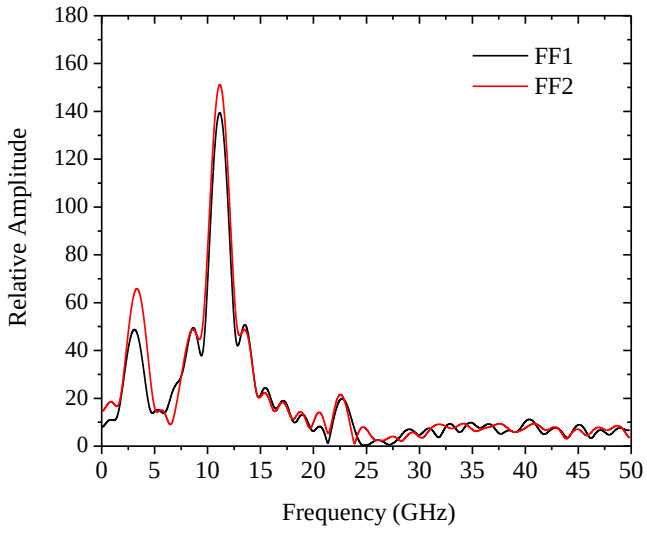

(b)

Figure 6.5 Far field measurements (a) Changes in the reflectivity as a function of delay time from far field ensemble measurements at two different positions. (b) The fast Fourier transform of the measured waveforms.

waveforms represent average the response of several nanodisks. The waveforms obtained

with the far-field detection approach on two different locations on the sample surface show a damped oscillatory response with the same period. The red curve shows a prominent spike with negative polarity at short time delays due to a large temperature difference the electrons and the lattice in the gold nanodisk. The fast Fourier transform of the measured waveforms shown in Fig. 6.5(b) has three prominent amplitude peaks at 3.3 GHz, 11.2 GHz, and 22.6 GHz, for the red curve. The 3.3 GHz peak corresponds to a surface

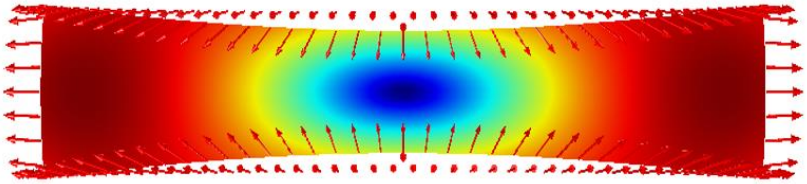

(a)

(b)

Figure 6.6 The acoustic vibration mode of single gold nanodisk. (a)The calculated displacement and (b) volumetric strain for a single gold nanodisk on a glass substrate

acoustic wave with a characteristic wavelength that is associated with the lattice spacing of the plasmonic nanodisks. The 22.6 GHz peak is remarkably close to a harmonic of the 11.2 GHz, and the existence of these pair is not unexpected, since the oscillatory thermoreflectance signal exhibits a saw-tooth profile. The 11.2 GHz peak is associated with the two-dimensional in-plane radial breathing mode, verified by a numerical solution of

the elastodynamic wave equations in COMSOL Multiphysics for the sample geometry. The calculated displacement and volumetric strain for a single gold nanodisk on a glass substrate are shown in Figs. 6.6(a) and (b). The numerical model yields the best match to the measured resonance frequency of 11.2 GHz, for disk diameter of 128 nm, assuming the bulk values for the film and substrate elastic properties. The best-fit result for the nanodisk diameter is in close agreement with estimates from SEM images. The calculated displacement has a node at the center of the disk and it increases along the radial direction to the maximum values at the edges of the disk. Furthermore, experimental measurements of the in-plane radial breathing mode frequency for gold nanodisks of comparable sizes on a glass substrate in the literature [93] are close to our measurement.

Near-field Measurements: Figure 6.7(a) and (b) shows waveforms obtained by positioning the probe-tip on four different nanodisks, and their corresponding amplitude spectra. The time resolved thermoreflectance waveforms are plotted with a vertical offset for ease of viewing. The amplitude of the thermoreflectance waveforms are of the order of 10-5 to 10-6, which is smaller than the far-field measurements. The waveforms show a similar trend that consists of a sharp transient close to the pump and probe time delay t = 0, followed by decaying underdamped oscillations with smaller amplitudes compared to the far-field measurements. The frequency of the in-plane radial breathing mode is prominent in the amplitude spectrum of each waveform, and it varies between 10.8 GHz and 12.8 GHz as

shown in Table 6.1. The measured resonance frequencies are within 14% of the

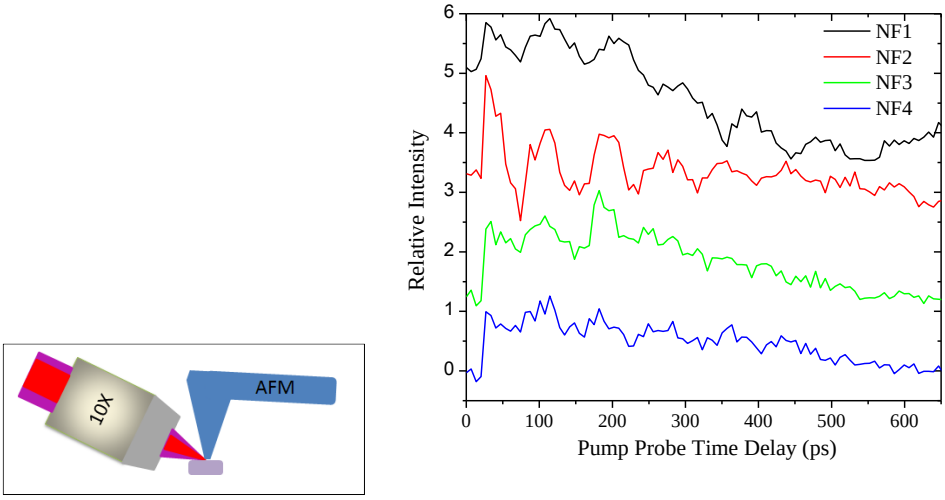

(a)

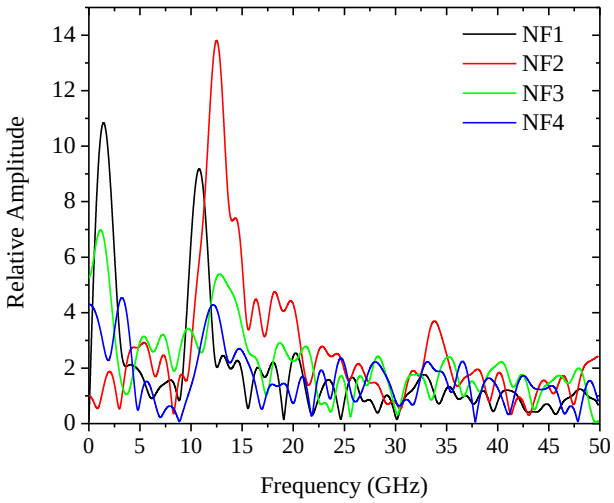

(b)

Figure 6.7 Near field measurements (a) Transient resolved waveforms obtained by positioning the probe-tip on four different nanodisks, and (b) their corresponding amplitude spectra.

corresponding far-field measurements. The table also shows the estimated nanodisk

diameters in the range of 110 nm to132 nm, which is consistent with size variability

Waveform #	Resonance Frequeny (GHz)	Nanodisk Diameter (nm)
FF1	11.2	128
FF2	11.2	128
NF1	10.8	132
NF2	12.5	112
NF3	12.8	110
NF4	12.2	116

Table 1 The frequencies of the in-plane radial breathing mode in the amplitude spectrum of near-field waveform, and the corresponding calculated diameters of gold nanodisks

observed in the SEM images of the sample. A small and distinct amplitude peak at 34 GHz corresponding to the out-of-plane extensional mode of the nanodisk is observed in spectrum of one of the waveforms (i.e. NF1 in Fig. 6.7(a)). Using the fundamental out-of-plane extension mode frequency, fextension = cl/2d, where cl is bulk compressional wave speed in gold and d is the disk thickness, we estimate the thickness of the gold disk to be 47 nm, which is close to the nominal value of 50 nm. The literature value for cl = 3200 m/s for bulk gold is assumed. In order to verify that the measured waveforms results from the probe-tip and sample interaction, we retracted the probe-tip by a vertical distance of approximately 1μm and repeated the measurement. Figure 6.8 shows a comparison of the measured waveform and one of the near-field measurements. With the probe-tip in its retracted position, the measured waveform reduces to the background noise floor. In addition, the peak-to-peak amplitude of the first oscillation cycle in near-field data is 35

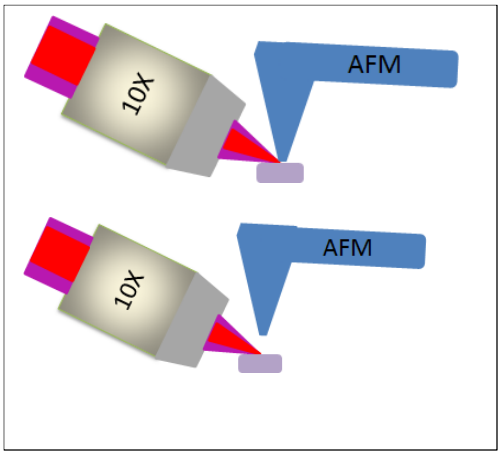

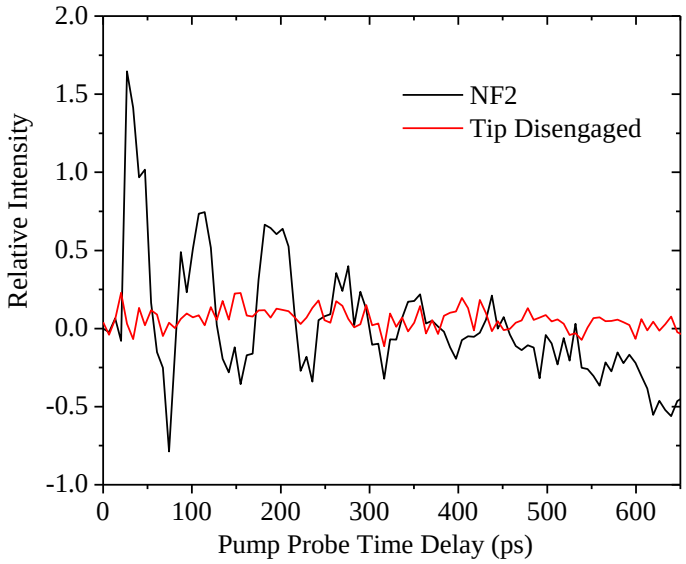

Figure 6.8 Comparison of the measured waveform with probe-tip in retract position and one of the near-field measurements.

times larger than the root-mean square amplitude of noise floor within the time window of the measurement. We remark that with multiple bursts of pump laser pulses modulated at f_{AOM}, the fast thermal and acoustic response of the sample is modulated at the same frequency. We rule out the possibility of probing the sample response based on direct

mechanical modulation of the AFM cantilever deflection by the nanodisk at f_{AOM} due to the small AFM cantilever resonance frequency compared to the f_{AOM}. In addition, direction illumination of the top cantilever with the probe laser yielded an unmodulated background noise.

6.4.2 Spatial Variation of the Near-field Thermoreflectance Measurement

(a)

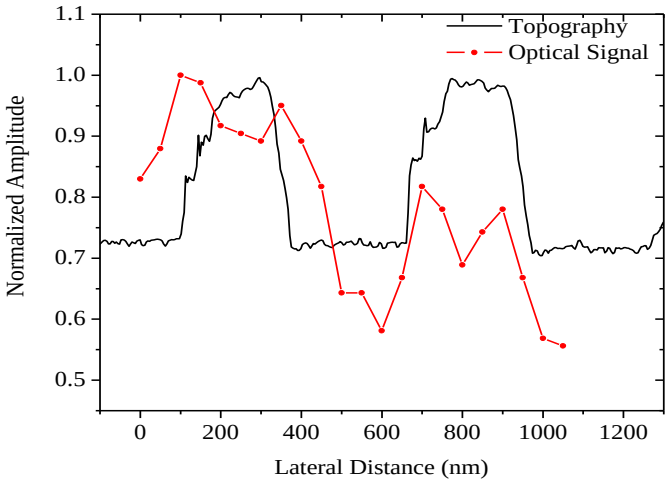

(b)

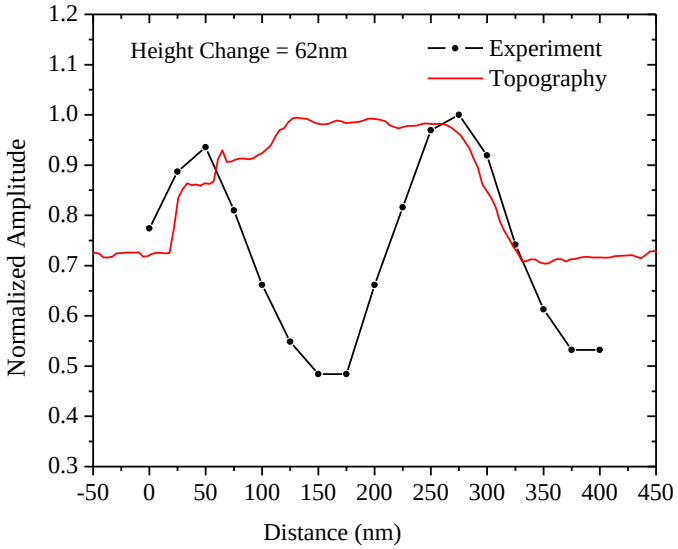

(c)

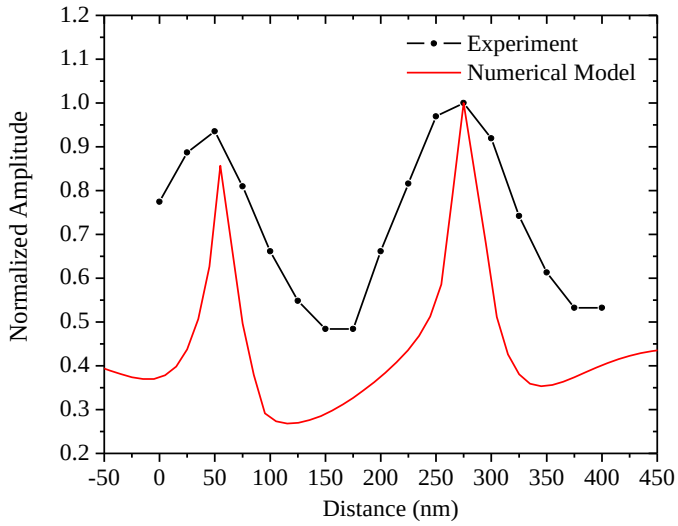

(d)

Figure 6.5 Spatial variation of near-field thermoreflectance signals. (a) contact mode AFM topographic image of sample. Measurements of the thermoreflectance signal is obtained along the dotted lines in the picture. Scale bar in picture is 550 nm. (b) comparison of normalized thermoreflectance intensity to the topography along the measurement line. (c) comparison of the simulated near-field intensity and measured thermoreflectance signal across the diameter of a single gold nanodisk, (d) AFM image of single isolated nanodisks used for the experiment in (c). Scale bar in (d) is 200 nm.

To further elucidate the local origin of near-field measurements, we performed point-to-point measurements of the local thermoreflectance at a fixed time delay of 128 ps between the pump and probe lasers, by the scanning sample along on direction, while keeping the position of the focused pump and probe lasers relative to sample and probe-tip stationary. During the measurement, the probe-tip probed the vibration of two gold nanodisks. The pump-probe time delay of 128 ps was chosen because it coincides with the second

oscillatory cycle in the transient thermoreflectance measurements in Fig. 6.5(a). To avoid artifacts from the vertical motion of the sample scanning stages as the probe tip moves over a nanodisk, each theromoreflectance measurement was taken after a lock-in integration time of 3s, which is much longer than the response time of the AFM feedback control system. The topography of the scanned area on the sample is shown in Fig. 6.9(a) and the thermoreflectance measurements were taken on highlighted dash line in the picture. We compare the thermoreflectance measurement to the AFM cantilever feedback voltage in Fig. 6.9(b) in order to interpret the features in the optical signal with respect to the position of the gold disks. The amplitude peak and trough in the topography correspond to the locations of the gold nanodisk and glass substrate. The height contrast in the topography is close to 62 nm, corresponding to the gold thickness. At the beginning of the thermoreflectance measurement, the probe-tip is positioned over the glass substrate close a nanodisk. The thermoreflectance measurement shows distinct features that are different from the topography, particularly close to the edges of the nanodisk, where the signal has two lobes. The decreasing amplitude of the thermoreflectance measurement with distance may be due to slight misalignment of the probe laser relative to the probe-tip and sample interaction region. The position dependent thermoreflectance intensity may result from the local strain induced modulation of the electric field distribution around the disks, in which case, the probe-tip strictly acts as local scatterer that couples the near-field optical signal to the far-field. We investigate this hypothesis using a finite element numerical calculation

of the electric field intensity distribution around a single gold disk, for the probe laser illumination angle and polarization used in our experiments. To account for the size of the probe-tip and sample interaction, the intensity of the total electric field vector $|E_{tot}|^2$ is integrated over a volume V, such that the measured optical signal is represented by S,

$$S = \int_V |E_{tot}|^2 \, dV.$$

The calculated intensity across the disk is shown in Fig. 6.5(d), and is normalized to allow for comparison with the measured thermoreflectance intensity across a single disk. A comparison of the topography and the measured thermoreflectance signal is shown in Fig. 6.5(c). We remark that the topography may over estimates the diameter of the gold disk due to the probe-tip geometry (apex sharpness and side-wall angle). The thermoreflectance measurements was obtained with a step size of 25 nm per point. In the numerical calculation, the component of the incident electric-field in the plane of the sample is aligned parallel to the direction of the lattice vector and the averaged probe excitation voxel is a sphere with a radius of 20 nm. The distance between the intensity peaks of the two lobes is 225 nm, and the numerical model yields the best agreement with experiment for a disk diameter of 190 nm. A modest agreement between the relative intensities in the experimental and numerical data is obtained. The light intensity decreases to a minimum close to the center of the disk, and it is concentrated near the edges. The extinction ratio of the thermoreflectance data is smaller than the numerical measurement because of background noise. The width of the edge lobes which in the numerical model is controlled

by voxel size of the probe-tip excitation volume is smaller than the measured data, suggesting a more complicated probe-tip interaction dynamics. Ultimately, what we can conclude from the numerical simulation is that the localized optical field around the disk is modulated by the local strain or displacement profile along the disk radius, which leads to the thermoreflectance profile measured in the experiment. The spatial variation of the thermoreflectance measurements is on the order of the step size, which is much smaller than the spot size of the focused probe laser (6μm).

6.5 Discussion

This work raises a number of interesting questions. For example, how is the near-field coupling of plasmons between the probe-tip and sample modified by dynamic changes in the dielectric properties of the nanodisk and probe [111]? Can one map the eigen vibration mode shapes of the nanodisk in the presence of non-uniform near-field plasmon distribution around the nanodisk? How does unwanted background scattering, which is expected in our measurements, affect the local transient thermoreflectance signal measured in the far-field and can these effects be eliminated by interferometeric detection methods [112]? What is the minimum detectable local sample strain that be resolved with this technique? How is the damping of in-plane acoustic phonon vibrations in the sample influenced by the contacting probe-tip? To address these questions, further experiments and numerical studies in carefully designed samples need to be conducted in order to understand the near-field interaction in the various regimes, such as, (1) the strong coupling

regime, comprised of a sharp-plasmonic metal tip and plasmonic nano-objects, and (2) the weak coupling regime, where a dielectric probe-tip is used. Perhaps, access to the amplitude and phase of the plasmon modes, by an interferometric detection of the scattered light from the probe-tip and sample interaction, may further elucidate the coupling between the plasmonic and phononic fields in nanoscale structures.

6.6 Conclusion

We report the time-resolved measurement of acoustic phonon vibrations on individual gold nanodisks illuminated in reflection mode near the localized surface plasmon resonance wavelength LSP = 730 nm. To facilitate the measurement, we incorporated a sharp metallic probe tip in contact with the sample into a picosecond ultrasonic setup. Time resolved near-field thermoreflectance measurements on individual nanodisks are compared to far-field measurements, and the results are in good agreement. The far-field measurements, sampled the thermoreflectance of several nanostructures in the sample, and the amplitude spectra of the measured data had peaks at the average in-plane radial breathing mode oscillation frequency of the gold nanodisks, and a surface acoustic wave resonant oscillation resulting from impulsive thermal grating produced by the disk array. On the other hand, the near-field measurements only yielded amplitude peaks in the frequency range between 10 to 13 GHz, corresponding to the in-plane radial breathing mode, and an out-of-plane extensional mode at 34 GHz. By the resonance frequencies obtained from the solution to elastodynamic

wave equation for the sample geometry, the diameter and thickness of the nanodisk were predicted. The range of predicted nanodisk diameters are in good agreement with estimates from SEM images of the fabricated sample. We observed that the near-field thermoreflectance measurements showed an enhanced reflectivity contrast with a lobed pattern near the edge of each nanodisk that obscured the spatial strain or displacement pattern of the in-plane phonon vibration mode. From our numerical calculations of the electric field distribution around each nanodisk, we found the measurement to be correlated with the dipolar plasmon mode of the disk. Furthermore, the spatial-temporal behavior of the thermoreflectance measurements depends on the sample dynamics close to the probe-tip. The experimental approach will provide a new tool to facilitate investigation of nanoscale phonon transport [113] and ultrafast optomechanical interactions in coupled plasmonic and phononic nanoscale devices with complex geometries. The latter have important implications in the development of, high speed opto-acoustic modulators, reconfigurable nanomechanical plasmonic metastructures, and transducers for detection of acoustic vibrations using confined nano-optical cavities.

Chapter 7 Ultrafast Acousto-plasmonic Sensing in Plasmonic Nanoantennas Array

7.1 Introduction

Plasmonic nanostructures have played an important role in the advancement of nanotechnology due to their unique abilities to convert far field light to surface plasmon polaritons. The deep subwavelength confinement and strong enhancement of optical field, high sensitivity to changes of geometry and refractive index distribution in the surrounding environment enable plasmonic nanostructures to find extensive applications ranging from ultrasensitive gas sensors, solar energy technology, to advanced optical manipulation. Recently, a new class of elevated plasmonic nanostructures have been developed that show promise for sensing, where by their larger available surface area enhances sensing capabilities compared with substrate-bond structures [115]. One particular case is pillar nanoantennas (p-NA), which have found tremendous application in areas as diverse as data strorage [116], photography [117], plasmonic nanotweezers [118], and audio recording [116]. For sensing application, when placed close to a sample surface, each element of the p-NAs can serve as a nanosized optical sensor, similar to metallic probes used in near field scanning optical microscopy (NSOM). A large array of pillar nanoantennas will allow for high throughput measurement, overcoming the disadvantage of serial point-by-point scanning which is major limitation of scanning probe microscopy methods including the NSOM techniques.

Another advantage to be gained for isolated plasmonic nanoantennas is the possibility of amplifying optical fields around small sized nanostructures, thus allowing for enhancement in the detection of ultrafast acoustic vibrations from these objects. For example, Thorsten et al. [83] demonstrated enhanced detection sensitivity to the acoustic vibrations of a single gold nanoparticle by placing in the near-field a larger plasmonic nanoantenna. Kevin et al. [82] demonstrated the possibility of achieving probe polarization based selective detection of orthogonal acoustic vibration modes of lithographically patterned gold nanostars, at frequencies in the GHz range. Furthermore, Thijssen et. al. [119] explored coupled gap mode plasmons in a metal-insulator-metal structure to detect the thermal motion of doubly clamped nanomechanical resonators with a displacement sensitivity of 1.11 x 10^{-13} m/$Hz^{1/2}$. In this chapter, I explore the localized Plasmon resonances of a pair of nanoparticles

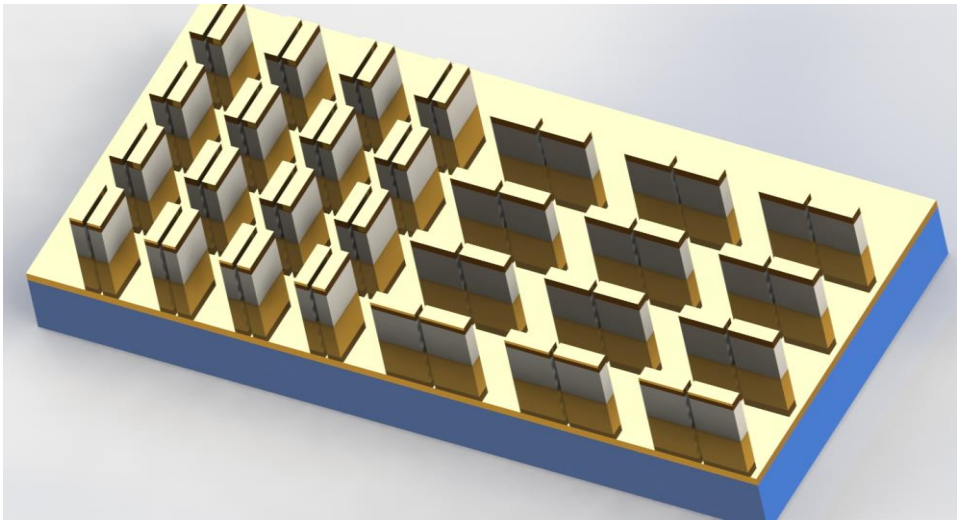

Figure 7.1 Schematic Illustration of the pillar Plasmon-nanomechanical resonators

separated by narrow air gaps to create local optical probes with subwavelength volume for sensing nanomechanical vibrations. To demonstrate the capabilities for nanomechanical detection, the nanoparticles are supported by polymer pillars to optically isolate the nanoparticles from the substrate. The polymer pillar also provide a large thermal expansion mismatch with the gold nanoparticles, which allows for enhanced generation of acoustic vibrations in the nanoparticles when illuminated by a probe laser. Figure 1 shows a schematic illustration of the array of pillar Plasmon-nanomechanical resonators, where gold caps act as ultrafast nanomechanical resonators.

7.2 Methods

7.2.1 Sample Fabrication

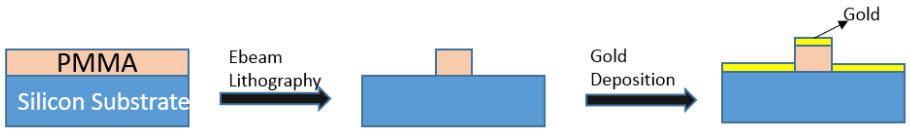

Figure 7.2 Schematic illustrating the fabrication procedure for pillar plasmonic nanoantenna.

The sample consists of a two dimensional array of elliptical gold caps dimers supported by polymer pillars on a silicon substrate. The sample is fabricated by electron-beam lithography. The fabrication procedure is schematically shown in Fig. 7.2. First, a single crystal silicon wafer is sonicated in acetone for 5 min and subsequently rinsed in an isopropyl alcohol (IPA) solution. Next, a thin film of polymethyl methacrylate photoresist (PMMA 950 A4) with thickness of approximately 200 nm is spin-coated on the substrate

at 4000 revolutions per minute for 45s. Consequently, the PMMA film was treated on a hot plate at 180 ℃ for 2 min. The sample is patterned with an electron beam using the Electron Beam Lithography System: JEOL 9300, operated at a voltage level of 100 kV and with a beam current of 1 nA. After the sample is exposed to the electron beam and removed

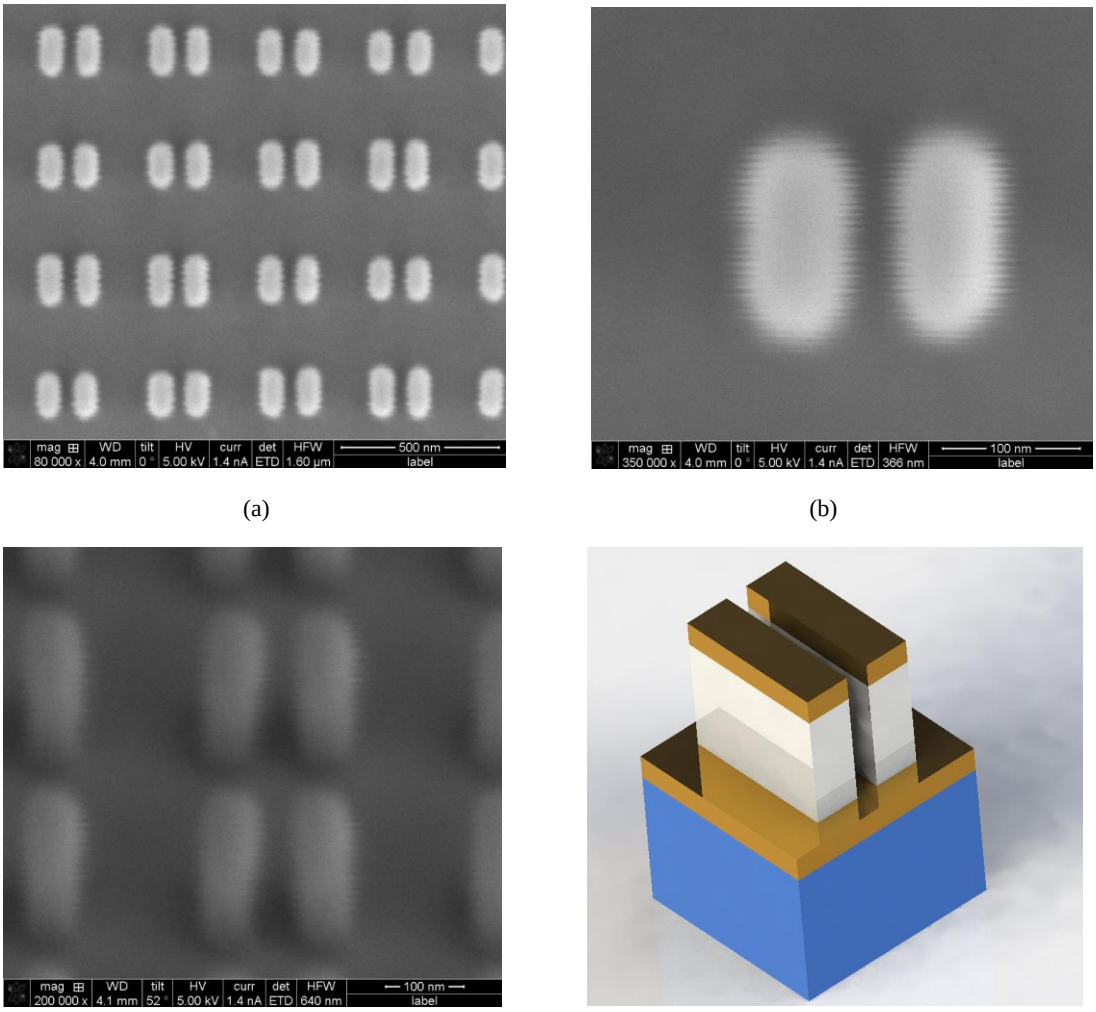

(a) (b)

(c) (d)

Figure 7.3 Side-to-side pillar plasmonic nanoantenna (a) (b) scanning electron micrograph of pillar plasmonic nanoantenna (c) 52 degree tilted view to show the height of the structure. (d) artistic representation of pillar plasmonic nanoantenna.

from the chamber, it is immersed in a mixture of IPA and water having a ratio of 21 to 9 at 0℃ for 35s. The sample is further rinsed with IPA, and cleaned by an oxygen Plasma descum. The final step involved deposition of a 3 nm thick chromium adhesion layer followed by a 35 nm thick gold layer, by the electron beam deposition. The thickness of

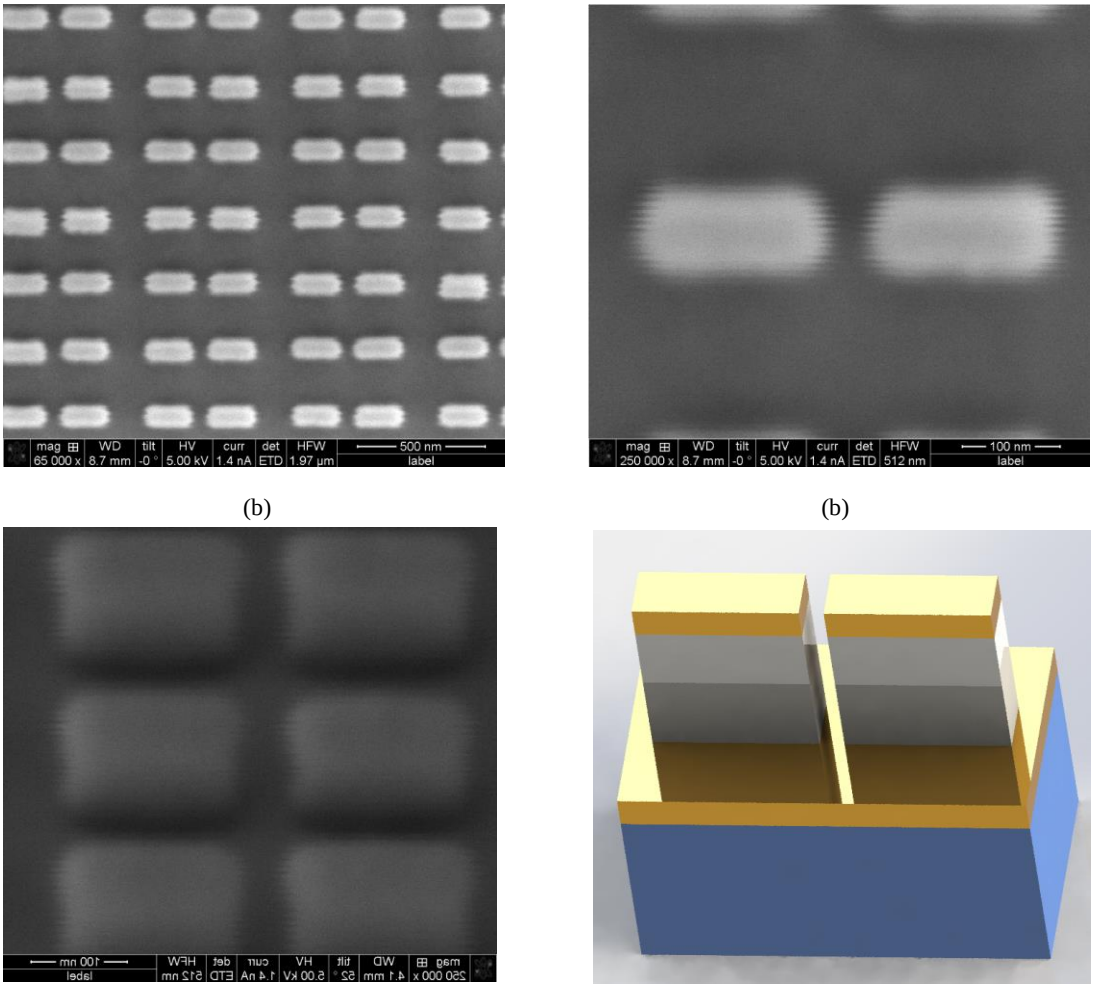

(b) (b)

(d) (d)

Figure 7.4 Tail-to-tail pillar plasmonic nanoantenna (a) (b) scanning electron micrograph of pillar plasmonic nanoantenna with slow and high magnification. (c) 52 degree tilted view to show the height of the structure. (d) artistic representation of pillar plasmonic nanoantenna.

the deposited films was monitored by a quartz crystal microbalance and further confirmed by profilometer measurements. The geometry of the fabricated samples is shown in Figs.7.3 and 7.4 for the different sample configurations namely, the side-to-side and tail-to-tail dimers. The fabricated pillars have a lattice spacing of 400 nm and a dimer spacing of between 10 to 60 nm. Scanning electron microscopy (SEM) images were also taken at a tilt angle of 52 degrees. The nominal size of the dimers are about 140 nm along the long axis by 70 nm along the short axis. The SEM images of the samples show great uniformity and regularity.

7.2.2 Optical Characterization of Localized Cap and Gap Plasmon Resonances

7.2.2.1 Tail-to-tail pillar plasmonic dimers

The optical reflectivity spectrum of the fabricated samples was characterized by illuminating the sample surface with a super-continuum laser source spanning the wavelength range between 400 and 900 nm, and the wavelength spectrum of the reflected light is monitored in a free space spectrometer (Jobin Yvon CP140-103 grating, Ausor DU 420A camera). The experiments were performed in the laboratory of Professor Kimani Toussiant in the Mechanical Science and Engineering Department at the University of Illinois at Urbana Champagne. The measured spectra for the side-to-side and tail-to-tail sample configurations are shown in Figs.7.5 and 7.6. The spectrum of the tail-to-tail sample shows a broad localized surface Plasmon resonance (LSP) peak close to a wavelength of

770 nm for a vertically polarized illumination probe light, due to collective oscillation of electrons along the long axis of the gold cap. For the horizontally polarized probe, the measured spectrum shows a small through around the same wavelength. A numerical calculation of the expected spectrum obtained from the solution of the electromagnetic wave equations in the COMSOL finite element software, using a plane wave input electric field. Periodic boundary conditions are applied to the simulation box. For a vertically

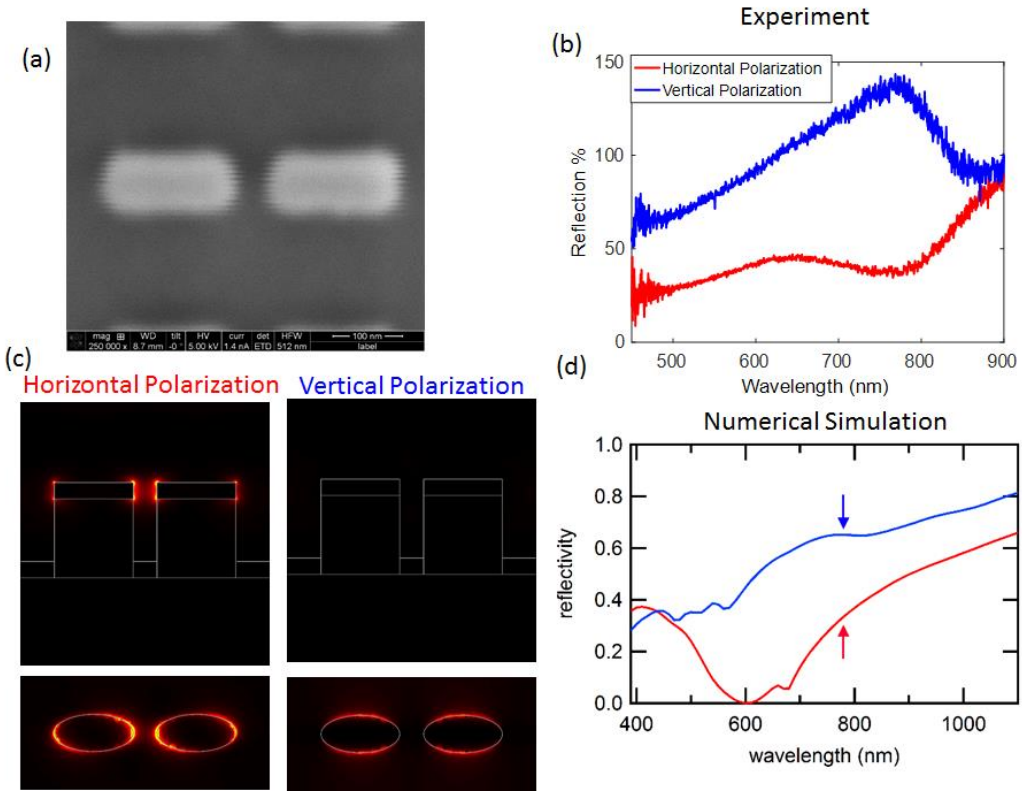

Figure 7.5 Tail-to-tail pillar plasmonic nanoantenna (a) (b) scanning electron micrograph of pillar plasmonic nanoantenna with slow and high magnification. (c) 52 degree tilted view to show the height of the structure. (d) artistic representation of pillar plasmonic nanoantenna.

polarized input, the calculated spectrum has a small broad peak at 770 nm marching the experimental data. However, for the horizontal polarized input, the calculated spectrum shows a prominent trough at 600 nm corresponding to the gap Plasmon resonance. At the gap resonance, the electric field at the edges of the gold cap interacts to create a strongly confined field in the narrow gap between the gold caps. For the probe laser wavelength of 780 nm used in my experiments, Fig. 7.5(c) shows the electric field distribution two near neighbor gold disks at the probe laser wavelength, for the two different polarizations. The electric field is confined in the gap between the gold caps for the horizontal polarization, and at the vertical edges of the sample for the vertical polarization. It is possible that in the experiment, the gap Plasmon resonance is weakly excited due to the large gap of 55 nm between the gold caps. The source of the discrepancy between the measured and calculated spectra is unclear at the moment, although, it is important to note that the sample geometry and dielectric properties are sufficient captured in the numerical model.

7.2.2.2 Side-to-side pillar plasmonic dimmers

The measured optical reflectivity spectra for the side-to-side gold dimmer samples are shown in Fig. 7.6(b). It is important to note that the gap spacing for this case is close to 20 nm, as seen in the SEM image in Fig. 7.6(a). The plots show have trough close to 600 nm, corresponding to the gap Plasmon resonance. For the horizontally polarized illumination laser, the gap Plasmon resonance is blue shifted to close to 550 nm, although the resonance

spectrum around this wavelength is very broad. Unlike the tail-to-tail dimmers, there is no discernible LSP resonance peak for the gold cap in the measured spectra. The numerical

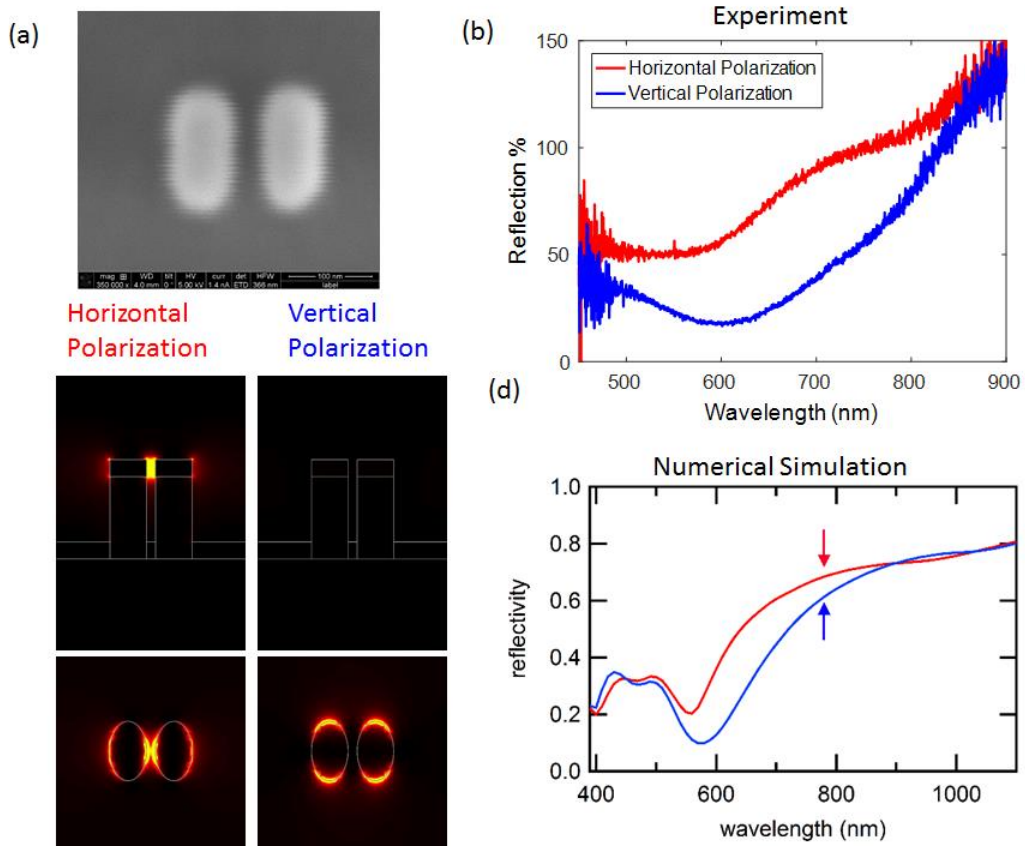

Figure 7.6 Side-to-side pillar plasmonic nanoantenna (a) (b) scanning electron micrograph of pillar plasmonic nanoantenna with slow and high magnification. (c) 52 degree tilted view to show the height of the structure. (d) artistic representation of pillar plasmonic nanoantenna.

calculation of the reflectivity spectrum has closer agreement with the measurement than with the tail-to-tail dimmers. The calculated spectrum shows a prominent through at the gap Plasmon resonance wavelength of 590 nm for the vertical polarization, which is close to the measurement. For the vertical polarization, the resonance is slightly blue shifted to

550 nm. Figure 7.6(d) compares the electric field concentration within the gap and around the edges of the dimers for the horizontally and vertically polarized input electric fields. For the vertical polarization case, where the electric field vector is aligned with the long axis of gold dimer, a dipolar electric field distribution at the end tip of the gold caps. On the other hand, when the electric field is polarized along the vertical direction connecting the short axis of the gold caps, the electric field is localized within the gap, leading to strong coupling between neighboring gold caps. The side-to-side and tail-to-tail configurations of the gold dimers provide a suitable testbed to investigate the interaction of acoustic vibrations and plasmons in the weakly and strongly confined plasmonic cavities. In the weakly confined cavity, which corresponds to the tail-to-tail dimers with a large gap distance, the LSP resonance dominates the acousto-plasmonic interaction.

7.2.3 Experimental Setup

A schematic of the experimental setup is shown in Fig. 7.7. A two color pump and probe technique is used to excite and detect the acoustic vibrations of the samples. In the setup, a Ti:sapphire mode locked laser with a central wavelength of 780 nm and pulse duration of 150 fs and pulse-to-pulse repetition frequency of 80 MHz, is split into pump and probe beams by a combination of a half wave plate and a polarizing beam splitter. The frequency of the pump laser is doubled by transmission through a Barium Borate (BBO) second harmonic generation (SHG) crystal, such that the output wavelength of the pump laser is 390 nm. The pump laser is directed through an acousto-optic modulator (AOM) and the

transmitted intensity is modulated at a frequency f_{AOM} = 0.3 MHz. The probe laser at 780 nm is reflected from a retroreflector mirror mounted on a linear motorized translation stage

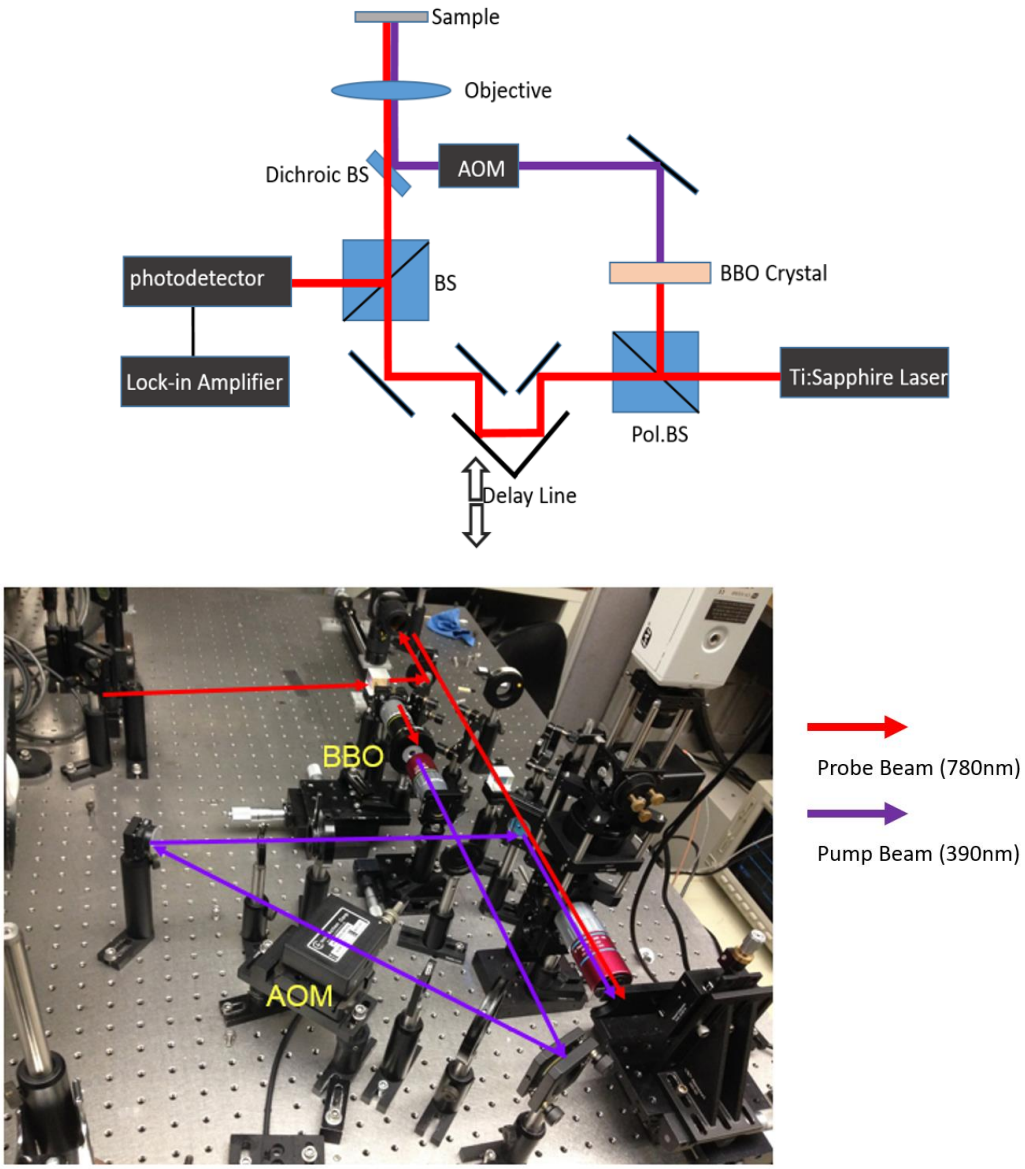

Figure 7.7 Schematic illustrating the fabrication procedure for pillar plasmonic nanoantenna.

for controlling the time delay between the probe and probe lasers. The reflected probe and

the pump lasers are recombined in a dichroic mirror and focused through a 20x microscope objective with a numerical aperture of 0.42 to small spot sizes on the sample surface. The spot sizes of the pump and probe lasers on the sample are approximately 5 μm and 1 μm. The scattered probe light from sample surface is collected by the 20x microscope objective and directed to a low noise photodetector with bandwidth of 150 MHz. A transmission filter with a transmission peak around 780 nm is placed in front of the photodetector to reject the scattered pump light. The voltage output of the photodetector is demodulated in a radio frequency lock-in amplifier at the pump laser modulation frequency f_{AOM}. The reference input voltage to the lock-in amplifier is obtained from the function generation used to excite AOM. In order to record the thermal and acoustic response of the sample response following the ultrafast pump laser illumination, the time delay between the pump and probe beams illuminating the sample surface is changed by adjusting the path length of the two beams using the linear translation stage. For each value of time delay, the in-phase and quadrature components of the photodetector voltage is recorded by averaging the photodetector output from multiple pump laser firing events. To optimize the signal-to-noise ratio of the measurement, an integration time of 100 ms was chosen. In addition, the input polarization of the probe laser is adjusted to align the input probe electric field in the plane of the sample along the long or short axis of the elliptical gold caps.

7.3 Time Domain Thermoreflectance Measurements

7.3.1 Tail-to-tail pillar plasmonic dimers

Figure 7.8(a) shows two waveforms obtained by illuminating the sample with the pump

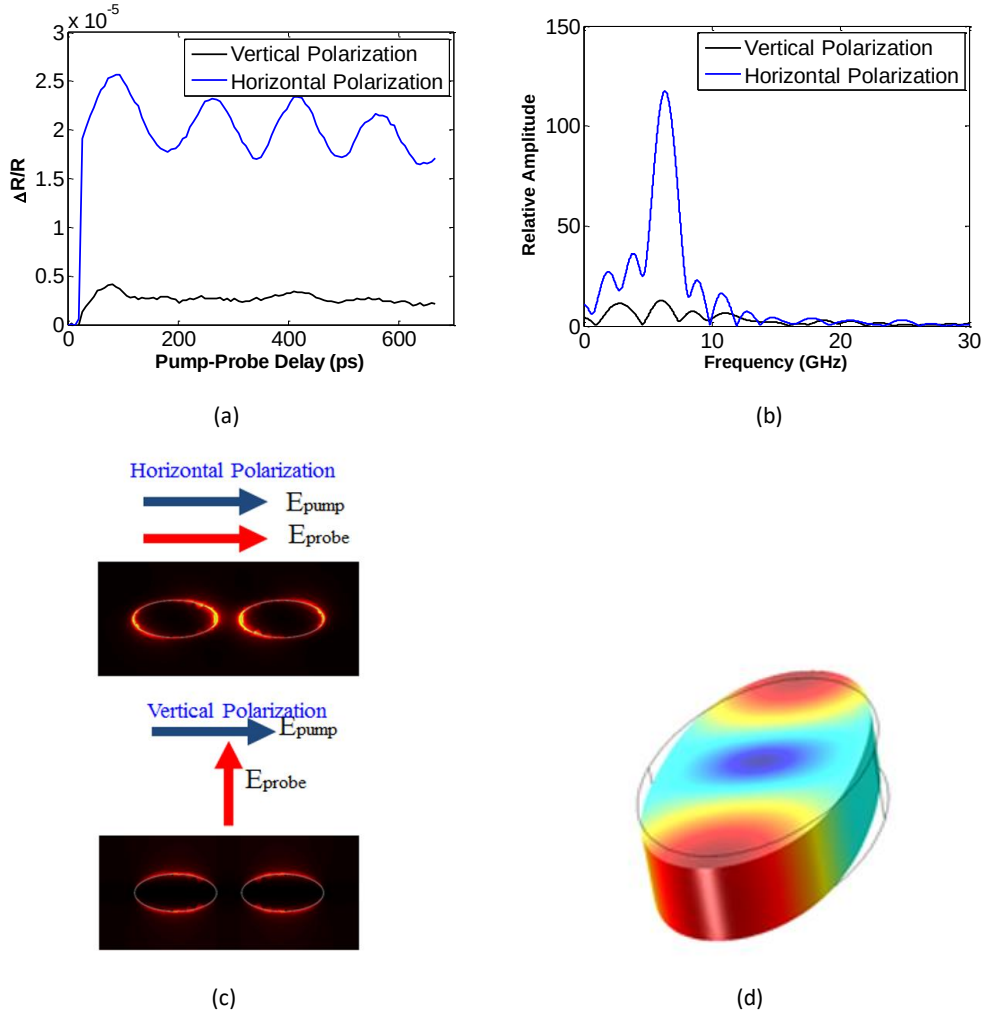

Figure 7.8 Transient Thermoreflectance Waveforms on the tail-to-tail dimmers (a) two waveforms obtained by illuminating the Tail-to-tail pillar plasmonic dimers sample with the pump laser and detecting the resulting transient reflectivity change (b) corresponding FFT spectra (c) simulated electric field in the top plane of the tail-to-tail dimmers when the polarization of the probe light is parallel and perpendicular to the center-to-center axis (d) the longitudinal in-plane extensional mode of the gold cap.

laser and detecting the resulting transient reflectivity change. In the two measurements, the polarization of the pump laser is aligned along the long axis between of the gold caps, and

measurements of the sample reflectivity change were taken for the parallel and orthogonal probe polarization directions. Two noticeable features are observed in the measurement. The transient reflectivity change close to a pump probe time delay of zero is about 20 times larger for the horizontally polarized probe, and the signal results from the local heating of the conduction band electrons and resulting modulation of the dielectric properties of the gold cap. The electronic system thermalizes within a timescale of about 1 ps, through electron-electron collisions, and electron-phonon collisions. The temporal resolution of the measurement, which is about 5 ps, was not sufficient to adequately resolve the electronic heating induced change in the sample reflectivity. Beyond 1 ps, the lattice temperature increases leading to a transient thermal expansion and the resulting thermal confined stresses in gold caps, are relieved by coherent excitation of acoustic vibrations. The large thermal expansion mismatch between the PMMA pillar and the gold cap facilitates the generation of large thermal stresses resulting large vibration amplitudes. The acoustic vibration of the gold cap modulates the cap size and the gap size between neighboring caps. It is important to note that in the case of the tail-to-tail plasmonic dimers, the transient modulation of the reflected probe intensity is due to the shift in the longitudinal LSP resonance frequency (or wavelength) that follows the change in the size of the gold cap. The longitudinal LSP resonance is excited by aligning the polarization of the probe light with the long axis of the elliptical cap. The Fourier amplitude spectrum of the measured waveforms shown in Fig. 7.8(b) has a dominant peak at 6.3 GHz for horizontal probe

polarization and no discernible resonant peak for the vertical polarization. The mode shape of the 6.3 GHz resonant mode corresponds to the longitudinal in-plane extensional mode of the gold cap. A numerical calculation of the mode shape of the resonance is shown in Fig. 7.8 (d), obtained by solving the elastodynamic equations for the sample geometry in the COMSOL Multiphysics software. The resonance frequency of the extensional mode depends on the thickness, and the long and short axis diameters of the gold disk and its elastic properties (Young's modulus and Poisson's ratio0. Surprisingly, the resonance frequency does not change with the elastic properties of the PMMA pillar. The results shows that the anisotropic nature of the LSP resonant allows for selective detection of the longitudinal extensional resonance by switching the probe laser polarization between the long and short axis of the gold cap. Furthermore, the amplitude of the resonant oscillations increases linearly with the average pump laser power between 1 and 12 mW, while the resonance frequency remains constant at 6.7 GHz.

7.3.2 Side-to-side pillar plasmonic dimers

Figure 7.9 shows the measured thermoreflectance measurements for the sample with side-to-side dimers. In this case, the gap plasmon resonance dominates the LSP resonance of the gold cap due to the strong near-field optical coupling between neighboring gold caps, as discussed in section 2.2. The thermoreflectance waveforms for the case of horizontal and vertical probe laser polarizations are markedly different. The directions of the probe laser polarizations with respect to the axis of the gold cap are shown in Fig. 7.9 (d). The

pump laser polarization is kept constant. Figure 7.9(a) and (b) are measuments taken on the same location over a long time scale of 700 ps and a short time scale of 350 ps. For the

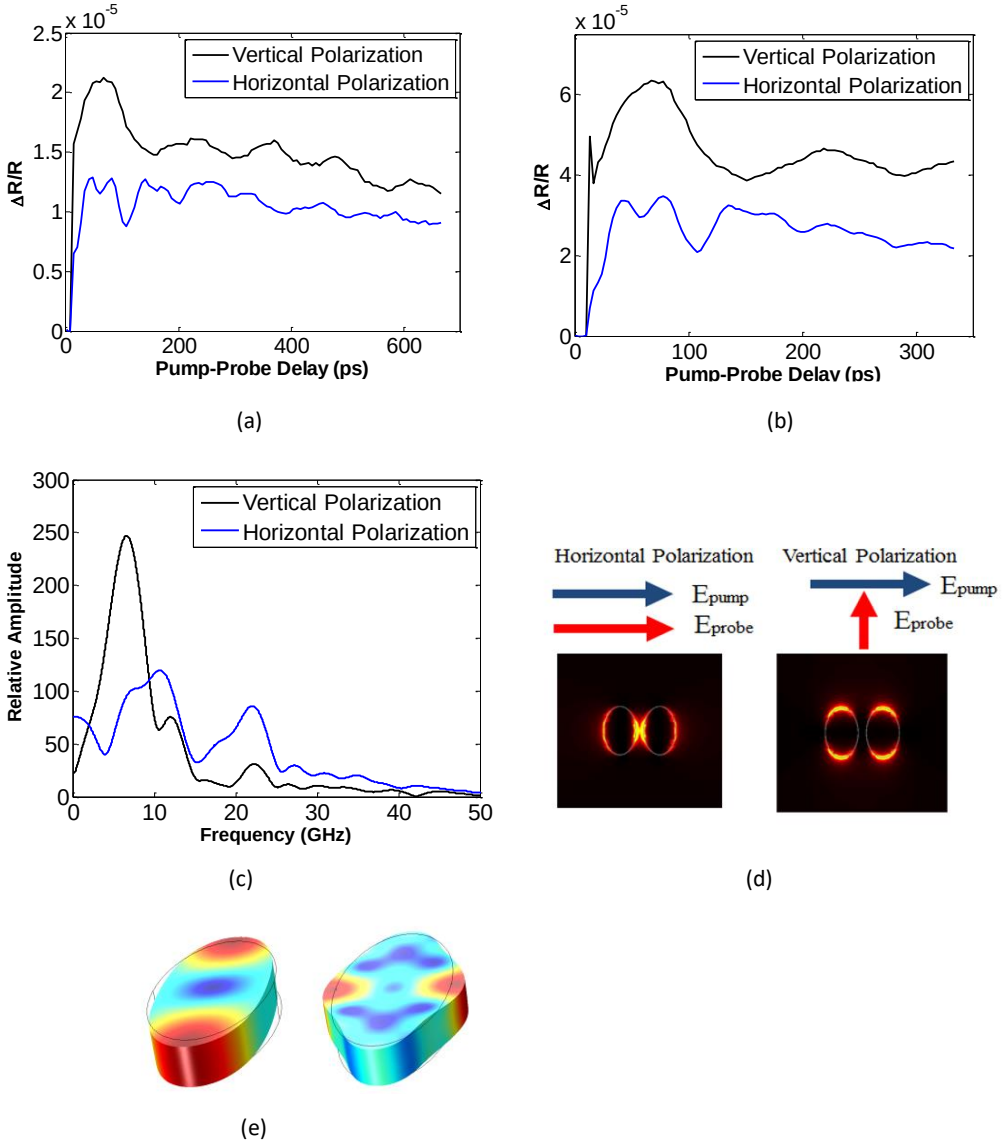

Figure 7.9 Transient Thermoreflectance Waveforms on the side-to-side dimmers. (a) and (b) Transient Thermoreflectance Waveforms with different time scale (c) corresponding FFT spectra for waveforms(b), (d) simulated electric field in the top plane of the side-to-side dimmers with different polarization of the probe light (e) two in-plane extensional modes of the gold cap.

case of the vertical polarization, the measured waveform shows the oscillatory reflectivity change close to 6.6 GHz, corresponding to the longitudinal in-plane extensional resonance mode. For the case of the horizontal polarization, the waveform shows a series of decaying dips, and the amplitude spectrum of the waveform has peaks at 10 GHz and 21 GHz. The second peak frequency is remarkably close to the second harmonic of the first peak, and

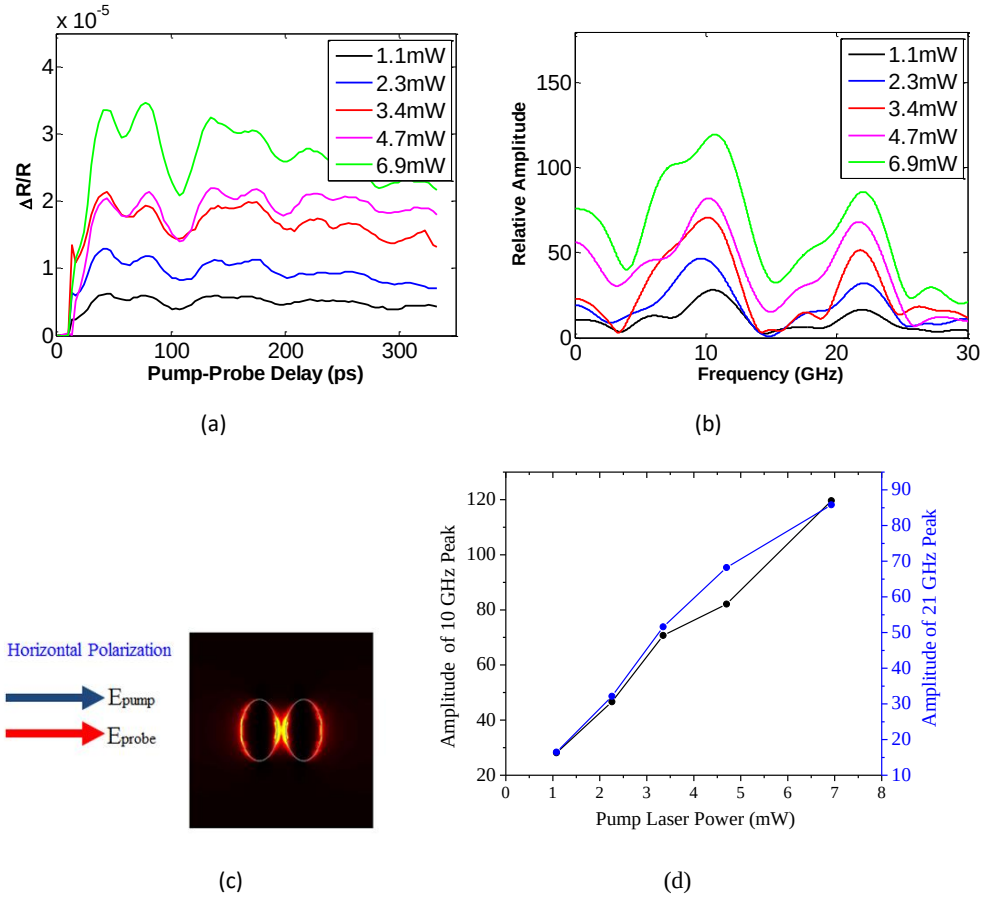

Figure 7.10 Nonlinear modulation of probe light intensity with gap width (a) a series of waveforms obtained for a range of pump powers between 1 and 6 mW. (b) corresponding FFT (c) electric field of the side-to-side dimmers with horizontal probe polarization (d) amplitude of peaks in (b) vs pump powers

the resonance spectrum for the waveform obtained with horizontal probe polarization does

not show the peak amplitude at 6.6 GHz. The 10 GHz resonance peak corresponds to the resonance frequency of in-plane extensional mode predominantly along the short axis of the gold cap. The mode shape for this resonance mode obtained using the COMSOL Multiphysics finite element numerical model is shown in Fig. 7.9(e) displays a strong stretch displacement along the transverse direction and a small displacement along the longitudinal axis. The stretch displacement of the short axis of the gold disk directly modulates the gap width of the dimers leading to modulation of the gap plasmon resonance frequency. It is important to note that the amplitude of the in-plane short axis resonance is typically much smaller than the long axis resonance. However, the resonance mode is detected as a result of the strong near-field confinement of the probe light within the narrow gap. Furthermore, due to the strongly confined field, the modulation of the scattered light intensity appears to be nonlinear in the gap distance. We verify this hypothesis by collecting thermoreflectance measurements at different pump probe powers leading to a range of gold disk displacements and gap widths. Figure 7.10(a) and (b) shows a series of waveforms obtained for a range of pump powers between 1 and 6 mW. The probe laser intensity and polarization are held constant for each measurement. The time domain waveforms shows a nonlinear increase in the amplitude of the thermoreflectance close to 100 ps with increasing pump laser power. The Fourier spectrum of the waveform shows consistent peaks at 10 GHz and 22 GHz, and the amplitudes at these frequencies increase monotonically with pump laser power as seen in Fig. 7.10(d). The amplitude of the 21 GHz

peak matches well to a quadratic functional dependence on the pump laser power as shown in figure 7.11.

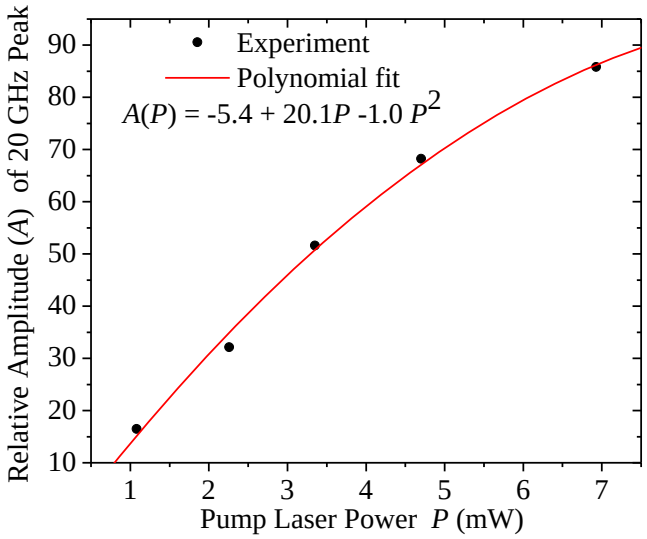

Figure 7.11 The amplitude of the 21 GHz peaks in figure 7.10 (b) matches to a quadratic function

7.4 Conclusions

The pillar plasmonic nanoantennas facilitate the funneling of electromagnetic energy from free propagating light into gap plasmons, without sophisticated coupling optics like Bragg gratings or near field optics. The gap plasmons allow for monitoring the acoustic vibrations in the gold caps through the modulation of the gap resonance wavelength as the separation distance between gold caps change with time. Owing to the elliptical geometry, which leads to anisotropic optical properties, selecting the probe polarization allows one to isolate the

acoustic vibration mode that is detected. In particular, the longitudinal or transverse in-plane extensional resonance frequency is detected by aligning the probe polarization along the corresponding direction, this allow for acoustic mode selectivity with high contrast. Finally, the side-to-side dimers, where electromagnetic energy is strongly confined within the gap, oscillatory modulation of the gap width led to oscillations in the scattered light intensity at the fundamental frequency of 10 GHz and a frequency, 21 GHz, which is remarkably close to its harmonic. It is possible that the combination of the change in size of the gold caps and the gap spacing is responsible for this nonlinear behavior. However, the harmonic frequency can be employed to eliminate background light scattering contributions that are not directly associated with the modulation of the gap width, thus providing a pure near-field detection channel in the far-field.

Chapter 8 Conclusion

8.1 Summary of Achievements

In this thesis, we explore the interaction between light, confined to the nanoscale in the form of localized plasmon polaritons, and the motion of nanoantennas oscillating at the frequencies on the order of hundreds of kHz to tens of GHz. The strong field confinement and local field enhancement around plasmonic nanoantennas make them extremely sensitive transducers of mechanical motion to scattered optical fields. Owing to this unique advantage, two types of nanoantennas are investigated for sensing application: 1.an a-NSOM probe and a vibrational sample system 2 arrays of pillar plasmonic nanoantennas oscillating at GHz frequencies.

We first explored the a-NSOM technique for local measurement of mechanical vibrations in metallic nanostructures. We showed that light coupling to SPPs in the a-NSOM probe and the nanostructure leads to enhancement in the intensity of the evanescent SPPs scattered from the interaction region between the sample and the probe-tip to the far-field. We explored the distance-dependence of the scattering intensity to detect local mechanical vibrations in metallic nanowire structures actuated by a piezoelectric transducer and a pulsed laser, and the measured resonance frequencies enabled the estimation of the nanowire elastic properties. The technique is versatile in that it allows for operation in the time- and frequency-domain with sub-wavelength lateral spatial resolution and exquisite temporal resolution. In particular, the time-domain actuation and detection approach may

find use in tracking the dynamic evolution of processes, such as single protein binding events, or stochastic vibration of overdamped nanomechancial resonators, with extremely high spatial and temporal resolution.

Next, we integrated a harmonic modulated photothermal source with the plasmonic nanofocusing probe, allowing for an all optical actuation and transduction of the steady state vibration of a nanomechanical resonator in the frequency domain. Fundamental and harmonics of bending flexural resonance mode shapes of nanomehcnical resonator were mapped within nanoscale resolution. Due to the broad bandwidth of the intensity modulated light source, the operational frequencies of this technique can be seamlessly extended to the GHz range, which is particularly attractive for probing motion in nanomechanical resonators with smaller widths compared to the SPP wavelength.

Besides sensing application, a plasmonic nanofocusing probe can be used as a nanoscale photothermal heat source when placing close to samples. We explored the TERS experimental configuration to correlate the shift of the Stokes frequency for the inelastic scattered light from a silicon substrate, with local sample heating. By comparing two excitation conditions, i.e., direct probe-tip apex illumination, and grating coupled LSPs, we observed a larger shift in the Stokes frequency for the grating illuminated probe. We estimate that the difference between the local sample temperature rise for the two illumination conditions is between 83 to 125 degrees. Furthermore, we confirmed the measured results using finite element modeling to obtain numerical solutions to the

electromagnetic wave equation for far-field optical excitation of LSPs. Further work is needed to understand complex multiphysics involved in local heating of the sample by the proximal nanofocusing probe. Nevertheless, the experimental results suggests if these physics of the heating process can be well understood and controlled, the plasmonic nanofocusing probe can be a promising tool for local photothermal heating of nanostructures, fundamental studies of nanoscale heat transport in materials, and heat assisted nanofabrication.

To measurement gigahertz frequency vibrations in nanostructure, pump probe technique was incorporated with a-NSOM probe, allow for achieving extremely high spatial and temporal resolution. The acoustic vibrations of individual gold nanodots was then investigated using pump probe near field scattering-type scanning optical microscopy. Comparison of the results with the measurements done in the far-field revealed that even though there is optical background due to tip-sample interaction, the optical response still reveals the ultrafast vibrations in nanodots followed by ultrashort pulse excitation.

Even though individual probe-sample system has tremendous application in sensing mechanical motions in samples with frequencies ranging from kHz to GHz, low throughput is a disadvantage of this optomechanical system. For high yield request, a pair of plasmonic pillar nanoantennas are designed. We explored optical detection of ultrafast mechanical motion of multimodal nanostructures by coupling between plasmon and phonon modes. We were able to distinguish complex mechanical modes in nanoantennas through optical

field concentration in their feed gap and the polarization sensitivity.

8.2 Suggestion for Future Work

In chapter five, we developed a new photoacoustic technique: Picosecond Ultrasonic Near-Field Optical Microscopy (PUNOM) for nanoelectronics defect and dimensional metrology, and explore this technique for nanomechanical characterization of individual plasmonic nanostructures. To explore the full potential of the PUNOM developed in this study, a few suggestions for future improvement are provided.

Firstly, the probes used in our PUNOM techniques are metal coated silicon probe. Absorption of pump light on the probe shaft and apex will produce a large thermal mismatch between metal layer and silicon substrate, which may cause the metal coating on the probe-tip to ablate. In addition, pump light induced ultrafast acoustic wave propagating in coated metal layer possibly add additional signal, which is detrimental to the detection and generation mechanism of the pump probe technique, making it difficult to extract the useful sample response. To overcome the disadvantage of metal coated silicon probes, single metal nanowires such as gold or silver wires can be integrated with scanning probes at the probe tip. Alternatively, commercialized tip enhanced Raman spectroscopy (TERS) probes are small gold wires attached to a tuning fork, which can be used in our PUNOM system to suppress the unwanted background signal coming from probe-tip response with

light illumination.

Secondly, the 10 X long working distance objective used in our measurements created a large illumination spot covering not only the probe apex, but also parts of the probe shaft. Both light induced photon force and thermal expansion of the metal in probe shaft make the AFM system instable, which will affect the data acquisition with a long time scale. For these experiments to be properly executed, it is crucial that the various quirks and instabilities related to the AFM system and the alignment optics have to be improved. For example, 50 X long working distance objective will provide better light concentration capability. Additionally, integrating a CCD camera with focusing objective will help focus light directly on tip apex, not on probe shaft. This improvement can be easily fulfilled with commercialized TERS system (such as Bruker TERS-AFM or Bruker TERS-STM system）. Furthermore, in our study, an open loop three-axis translation stage was used for alignment of the optics. The implementation of a more sensitive closed-loop translation stage will be able to minimize the hysteresis and the slow relaxation of the alignment stage, allowing it to make more sensitive and robust measurements.

Thirdly, usually the pump probe setup is built in a way that laser pulses of a common source are split into pump and probe pulses and the different optical path lengths are realized with a moving translation stage. In our system, the 780 nm wavelength output was used for the probe beam while the second harmonic at 390 nm wavelength was used for the pump beam, generated by feeding part of the laser beam into a BBO crystal. Unfortunately, the

efficiency of the second harmonic generation from BBO crystal is low and the collimated beam starts to diffract when passing through BBO crystal. Even though a highly focused pump light is not necessary in conventional pump probe technique, a large illumination spot will make the AFM probe instable. An alternative way would be two exactly synchronized ultrashort pulse lasers. The pump laser pulse is used for excitation, the probe pulse for measuring the experimental response. Both the pump beam and the probe beam can be concentrated in a nanoscale volume through high NA objective.

Chapter six induces an array of plasmonic pillar plasmonic nanoantennas, an exciting platform to investigate the coupling of plasmon modes to phonon modes. Owing to their large absorption cross-sections and high sensitivities, plasmonic nanostructures are used to generate coherent phonons up to terahertz frequencies. Generating, detecting and controlling such ultrahigh frequency phonons has been a topic of intense research. In this chapter we report that by manipulating decoupled and coupled plasmon resonance in pillar nanoantennas, we can detect the spatial properties of complex phonon modes below the optical wavelength through the interplay between plasmons and phonons. The results are very promising compared to others' work so far. If each element of pillar nanoantennas serves as an NSOM probe when placing in the near field optical region of the sample, an array of p-NAs can be utilized as an optical sensor for mapping the optical properties of the sample with a large area. Several improvement will be addressed here. The polymer used as pillar material is easily to be damaged since it has a large thermal expansion

coefficient. Glass pillar can be fabricated instead of PMMA pillar to increase the sample life span. Also, high frequency intensity modulated laser can be integrated as light source instead of femtosecond pulse laser to trigger the phonon vibrations of the nanostructure. Any perturbation such as absorption of external protein can be detected by measuring the frequency change of the nanostructure.

Reference

1. Isabelle, F., Cynthia, A. C. and Jean, P. C. “Multigate transistors as the future of classical metal-oxide-semiconductor field-effect transistors”, Nature 479, 310-316, (2011).
2. Feifei, Z., Sridhar K. and Carmen, M. L., “Bulk-wave and guided-wave photoacoustic evaluation of the mechanical properties of aluminum/silicon nitride double-layer thin films”, Ultrasonics 45, 66-76, (2006).
3. Chigarev, N., Rossignol, C. and Audoin, B., “ Surface displacement measured by beam distortion detection technique: Application to picosecond ultrasonics”, Rev. Sci. Instrum. 77, 114901, (2006).
4. Otto, L. M., Natalia, D. F. and Fabrice V., “Femtosecond response of a single metal nanoparticle”, Nano Letter 6, 3, 552-556, (2006).
5. Kelf, T. A., Tanaka, T., Matsuda, O., Larsson, E. M., Sutherland, D. S. and Wright O. B., “Ultrafast vibrations of gold nanorings”, Nano Letter 11, 3893-3898, (2011).
6. Antonelli, G. A. and Maris H. J., “Picosecond ultrasonics study of the vibrational modes of a nanostructure”, J. Appl. Phys 91, 3261, (2002).
7. Rief, M., et al., “Single Molecule Force Spectroscopy on polysaccharides by atomic force microscopy”, Science. 275(5304): p. 1295-7, (1997)
8. Neuman, K.C. and A. Nagy., “Single-molecule force spectroscopy: optical tweezers, magnetic tweezers and atomic force microscopy”, Nature Methods. 5(6): p. 491-505, (2008)
9. Rabe, U. and W. Arnold., “Acoustic Microscopy by Atomic-Force Microscopy”, Applied Physics Letters. 64(12),1493-1495, (1994)
10. Rabe, U., et al., “Imaging and measurement of local mechanical material properties by atomic force acoustic microscopy”, Surface and Interface Analysis 33(2), 65-70, (2002)
11. Yamanaka, K., H. Ogiso, and O. Kolosov, “Ultrasonic Force Microscopy for Nanometer Resolution Subsurface Imaging”, Applied Physics Letters, 1994. 64(2): p. 178-180.
12. Kolosov, O., et al., “Nanoscale imaging of mechanical properties by ultrasonic force microscopy (UFM)”, Acoustical Imaging, Vol 22, 1996. 22: p. 665-668.
13. Huey, B.D., et al., “Characterisation of the nanometer-scale mechanical compliance of semiconductors by Ultrasonic Force Microscopy”, Microscopy of Semiconducting Materials 2001, 2001(169): p. 531-534.
14. Knoll, B. and F. Keilmann, “Enhanced dielectric contrast in scattering-type scanning near-field optical microscopy”, Optics Communications, 2000. 182(4-6): p. 321-328.
15. Frey, H.G., et al., “Enhancing the resolution of scanning near-field optical microscopy by a metal tip grown on an aperture probe”, Applied Physics Letters, 2002. 81(26): p. 5030-5032.
16. Bouhelier, A., et al., “Plasmon-coupled tip-enhanced near-field optical microscopy”, Journal of Microscopy-Oxford, 2003. 210: p. 220-224.
17. N. J. Halas, S. Lal,W.-S. Chang, S. Link, and P. Nordlander, “Plasmonics in strongly coupled metallic nanostructures”, Chem. Rev. 111, 3913–3961 (2011).
18. A. N. Grigorenko, A. K. Geim, H. F. Gleeson, Y. Zhang, A. A. Firsov, I. Y. Khrushchev, and J. Petrovic, “Nanofabricated media with negative permeability at visible frequencies”, Nature 438,

335–338 (2005).

19. X. Dang, J. Qi, M. T. Klug, P.-Y. Chen, D. S. Yun, N. X. Fang, P. T. Hammond, and A. M. Belcher, "Tunable localized surface plasmon-enabled broadband light-harvesting enhancement for high-efficiency panchromatic dye-sensitized solar cells", Nano Lett. 13, 637–642 (2013).
20. D. J. Barber and I. C. Freestone, "An investigation of the origin of the colour of the Lycurgus cup by analytical transmission electron microscopy", Archaeometry 32, 33–45 (1990).
21. A. E. Cetin, A. F. Coskun, B. C. Galarreta, M. Huang, D. Herman, A. Ozcan, and H. Altug, "Handheld high-throughput plasmonic biosensor using computational on-chip imaging", Light Sci. App. 3, e133 (2014).
22. C. Rosman, J. Prasad, A. Neiser, A. Henkel, J. Edgar, and C. Sonnichsen, "Multiplexed plasmon sensor for rapid label-free analyte detection", Nano Lett. 13, 3243–3247 (2013).
23. M. Righini, P. Ghenuche, S. Cherukulappurath, V. Myroshnychenko, F. J. Garcia de Abajo, and R. Quidant, "Nano-optical trapping of Rayleigh particles and Escherichia coli bacteria with resonant optical antennas", Nano Lett. 9, 3387–3391 (2009).
24. M. Fleischmann, P. J. Hendra, and A. J.McQuillan, "Raman spectra of pyridine adsorbed at a silver electrode", Chem. Phys. Lett. 26, 163–166 (1974).
25. M.Moskovits, "Surface-enhanced spectroscopy", Rev.Mod. Phys. 57, 783–826 (1985).
26. N. Yu and F. Capasso, "Flat optics with desinger metasurfaces", Nature Mater. 13, 139–150 (2014).
27. B. J. Roxworthy, K. D. Ko, A. Kumar, K.-H. Fung, G. L. Liu, N. X. Fang, and K. C. Toussaint Jr., "Application of plasmonic bowtie nanoantenna arrays for optical trapping, stacking, and sorting", Nano Lett. 12, 796–801 (2012).
28. P. Jain andM. El-Sayed, "Plasmonic coupling in noble metal nanostructures", Chem. Phys. Lett. 487, 153–164 (2010).
29. K. D. Ko, A. Kumar, K. H. Fung, R. Ambekar, G. L. Liu, N. X. Fang., and K. C. Toussaint Jr., "Nonlinear optical response fromarrays of Au bowtie nanoantennas", Nano Lett. 11, 61–65 (2011).
30. X. Miao and L. Y. Lin, "Trapping and manipulation of biological particles through a plasmonic platform", IEEE J. Sel. Top. Quant. Electron. 13, 1655–1662 (2007).
31. W. Zhang, L. Huang, C. Santschi, and O. J. F. Martin, "Trapping and sensing 10 nm metal nanoparticles using plasmonic dipole antennas", Nano Lett. 10, 1006–1011 (2010).
32. M. Righini, A. S. Zelenina, C. Girard, and R. Quidant, "Parallel and selective trapping in a patterned plasmonic landscape", Nature Phys. 3, 477–480 (2007).
33. Balogun, O., Murry T. W. and Prada, C., "Simulation and measurement of the optical excitation of the SI zero group velocity Lamb wave resonance in plates", J. Appl. Phys. 102, 6, (2007).
34. Rogers, J. A. and Nelson, K. A., "Study of Lamb acoustic waveguide modes in unsupported polymide thin films using real-time impulsive stimulated thermal scattering", J. Appl. Phys., 73, 3, 1534-1556, (1994).
35. Rogers, J. A., Maznev, A. A., Banet, M. J. and Nelson, K. A., "Optical generation and characterization of acoustic waves in thin films", Annu. Rev. Mater. Sci., 30, 117-157, (2000).
36. Dmitri, K. G. and Sergey, I. B., "Nanofocusing of electromagnetic radiation", Nature Photonics, 8, 13-22, (2014).

37. Babadjanyan, A. J., Margaryan, N. L. and Nerkararyan, K. V., "Superfocusing of surface polaritons in the conical structure", J Appl Phys 87, 3785,(2000).
38. Stockman, M.I. "Nanofocusing of optical energy in tapered plasmonic waveguides", Phys. Rev. Lett. 93, 137404, (2004).
39. Diyar, S., Javid, S., Jae, S. L., Elena, S., Namkyoo P. and Christoph L., "Adiabatic nanofocusing scattering-Type optical nanoscopy of individual gold nanoparticles", Nano Letters 11, 1609-1613, (2011).
40. Jan, V., Jorg, R., Benedek, J. N., Peter, D., Daniel, R., Maniela, S., Petra, G. and Christoph, L., "Ultrafast electron emission from a sharp metal nanotaper driven by adiabatic nanofocusing of surface plasmons". Nano Letter 15, 4685-4691, (2015).
41. Samuel, B., Joanna, M. A., Robert, L. O. and Markus B. R., "Adiabatic tip-plasmon focusing for nano-raman spectroscopy", J. Phys. Chem. Lett. 1, 3427-3432, (2010).
42. Samuel, B., Joanna, M. A., Xiaoji, G., Robert, L. O. and Markus, B. R., "Femtosecond nanofocusing with full optical waveform control", Nano Lett. 11, 4309-4313, (2011).
43. L.Novotny and B.Hecht, Principles ofNano-Optics, CambridgeUniversity Press, (2006).
44. Ekinci, K. L.; Roukes, M. L., "Nanoelectromechanical systems", Rev Sci Instrum. 76, (6), (2005)
45. Eom, K.; Park, H. S.; Yoon, D. S.; Kwon, T., "Nanomechanical resonators and their applications in biological/chemical detection: nanomechanics principles", Phys Rep, 503, (4-5), 115-163, (2011)
46. Schwab, K. C.; Roukes, M. L., "Putting mechanics into quantum mechanics", Phys Today, 58, (7), 36-42, (2005)
47. Wang, W. H.; Yang, Q.; Fan, F. R.; Xu, H. X.; Wang, Z. L., "Light propagation in curved silver nanowire plasmonic waveguides", Nano Lett, 11, (4), 1603-1608, (2011)
48. Staleva, H.; Skrabalak, S. E.; Carey, C. R.; Kosel, T.; Xia, Y. N.; Hartland, G. V., "Coupling to light, and transport and dissipation of energy in silver nanowires", Phys Chem Chem Phys, 11, (28), 5889-5896, (2009)
49. Hartland, G. V.; Carey, C. R.; Staleva, H., "Ultrafast transient absorption studies of single metal and semiconductor nanowires ", Ultrafast Phenomena in Semiconductors and Nanostructure Materials Xiv, 7600, (2010)
50. Baffou, G.; Quidant, R., "Thermo-plasmonics: using metallic nanostructures as nano-sources of heat", Laser Photonics Rev, 7, (2), 171-187, (2013)
51. Coppens, Z. J.; Li, W.; Walker, D. G.; Valentine, J. G., "Probing and controlling photothermal heat generation in plasmonic nanostructures", Nano Lett, 13, (3), 1023-1028, (2013)
52. Mante, P. A.; Wu, Y. C.; Lin, Y. T.; Ho, C. Y.; Tu, L. W.; Sun, C. K., "Gigahertz coherent guided acoustic phonons in AlN/GaN nanowire superlattices", Nano Lett, 13, (3), 1139-1144, (2013)
53. Aubert, S.; Bruyant, A.; Blaize, S.; Bachelot, R.; Lerondel, G.; Hudlet, S.; Royer, P., "Analysis of the interferometric effect of the background light in apertureless scanning near-field optical microscopy", J Opt Soc Am B, 20, (10), 2117-2124, (2003)
54. Meirovitch, L., Fundamentals of Vibrations. McGraw-Hill Higher Education: New York, NY, 10020, 2001.
55. Truitt, P. A.; Hertzberg, J. B.; Altunkaya, E.; Schwab, K. C. J Appl Phys 2013, 114, (11).

56. Ahn, P., Chen, X., Zhang, Z., Ford, M., Rosenmann, D., Jung, I. W., Sun, C. & Balogun, O., “Dynamic near-field optical interaction between oscillating nanomechanical structures”, Sci. Rep. 5, 10058 (2015).
57. Walford J.N., Porto J.A., Carminati R., Greffet J.J., and Adam P.M., , Journal of Applied Physics, 89(9), 5159, (2001)
58. Sampathkumar, A., Murray, T. W. & Ekinci, K. L., “Photothermal operation of high frequency nanoelectromechanical systems”, Appl. Phys. Lett. 88, 223104 (2006).
59. Sampathkumar, A., Ekinci, K. L. & Murray, T. W., “Multiplexed Optical Operation of Distributed Nanoelectromechanical Systems Arrays”, Nano Lett. 11, 1014–1019 (2011).
60. A. J. Babadjanyan, N. L. Margaryan, Kh. V. Nerkararyan, “Superfocusing of surface polaritons in the conical structure”, J Appl Phys. 87, 3785 (2000)
61. M.I. Stockman, “Nanofocusing of Optical Energy in Tapered Plasmonic Waveguides”, Phys. Rev. Lett. 93, 137404 (2004)
62. R. Ruppin, “Effect of non-locality on nanofocusing of surface plasmon field intensity in a conical tip”, Phys. Lett. A 340, 299 (2005)
63. D. Sadiq, J. Shirdel, J. S. Lee, E. Selishcheva, N. Park, C. Lienau, “Adiabatic nanofocusing scattering-Type optical nanoscopy of individual gold nanoparticles”, Nano Lett. 11, 1609-1613 (2011)
64. Z. Zhang, P. Ahn, B. Q. Dong, O. Balogun, C. Sun, “Quantitative imaging of rapidly decaying evanescent fields using plasmonic near-field scanning optical microscopy”, Sci. Rep. 3, 2803 (2013)
65. S. Berweger, J. M. Atkin, R. L. Olmon, M. B. Raschke, “Adiabatic tip-plasmon focusing for nano-raman spectroscopy”, J. Phys. Chem. Lett. 1, 3427-3432 (2010)
66. J. Vogelsang, J. Robin, B. J. Nagy, P. Dombi, D. Rosenkranz. M. Schiek, P. Groß, C. Lienau, “Ultrafast electron emission from a sharp metal nanotaper driven by adiabatic nanofocusing of surface plasmons”, Nano Lett. 15, 4685-4691 (2015)
67. S. Berweger, J. M. Atkin, X. G. Xu, R. L. Olmon, M. B. Raschke, “Femtosecond nanofocusing with full optical waveform control”, Nano Lett. 11, 4309-4313 (2011)
68. P. Ahn, Z. Zhang, C. Sun, O. Balogun, “Ultrasonic near-field optical microscopy using a plasmonic nanofocusing probe”, J. Appl. Phys. 113, 234903 (2013)
69. A. V. Malkovskiy, V. I. Malkovsky, A. M. Kisliuk, C. A. Barrios, M. D. Foster, A. P. Sokolov, “Tip induced heating in apertureless near-field optics”, J. Raman Spectrosc. 40, 1349-1354 (2009)
70. Y. Yue, X. Chen, X. Wang, “Noncontact sub-10 nm temperature measurement in near-field laser heating”, Acs Nano 5, 6, 4466-4475 (2011)
71. M. Balkanski, R. F. Wallis, E. Haro, “Anharmonic effects in light scattering due to optical phonons in silicon”, Phys. Rev. B 28, 1928-1934 (1983)
72. M. Zdrojek, W. Gebicki, C. Jastrzebski, T. Melin, A. Huczko, “Studies of multiwall carbon nanotubes using Raman spectroscopy and atomic force microscopy”, Solid State Phenomena, Vols. 99-100, 265-268 (2004)
73. T. R. Hart, R. L. Aggarwal, B. Lax, “Temperature dependence of raman scattering in silicon”, Phys. Rev. B 1, 638-642 (1970)

74. J. Maultzsch, H. Telg, S. Reich, C. Thomsen, “Radial breathing mode of single-walled carbon nanotubes: Optical transition energies and chiral-index assignment”, Phys. Rev. B 72, 205438 (2005)
75. P. C. Eklund, J. M. Holden, R. A. Jishi, “Vibrational modes of carbon nanotubes; Spectroscopy and theory”, Carbon, 33, 7, 959-972 (1995)
76. S. D. M. Brown, A. Jorio, M. S. Dresselhaus, G. Dresselhaus, “Observations of the D-band feature in the Raman spectra of carbon nanotubes”, Phys. Rev. B 64, 073403 (2001)
77. P. B. Johnson, R. W. Christy, “Optical constants of the nobel metals”, Phys. Rev. B 6, 4370-4379 (1972)
78. B. A. Sellitto, D. Jou, J. Bafaluy, “Non-local effects in radial heat transport in silicon thin layers and graphene sheets”, Proc. R. Soc. A 0584 (2011)
79. G. Baffou, and R. Quidant, “Thermo-plasmonics:using metallic nanostructures as nano-sources of heat”, Laser Photonics Rev. pp. 1-17, (2012)
80. G. V. Hartland “Optical Studies of Dynamics in Noble Metal Nanostructures”, Chemical Reviews, 111, pp. 3858-3887, (2011)
81. F.D. Picca, R. Berte, M. Rahmani, P. Albella, J.M. Bujjamer, M. Poblet, E. Cortesm S.A. Maier, and A.V. Bragas, “Tailored Hypersound Generation in Single Plasmonic Nanoantennas”, Nano Letters, 16, pp. 1428-1434, (2016)
82. K. O’Brien, N.D. Lanzillotti-Kimura, Junsuk Rho, H. Suchowski, X. Yin, and X. Zhang, “Ultrafast acousto-plasmonic control and sensing in complex nanostructures”, Nature Communications, 5:4042, pp. 1-6, (2014)
83. T. Schumacher, K. Kratzer, D. Molnar, M. Hentschel, H. Giessen, and M. Lippitz, “Nanoantenna-enhanced ultrafast nonlinear spectroscopy of a single gold nanoparticle”, Nature Communications, 2:333, pp. 1-5, (2011)
84. S. Lal, S.E. Clare, and N.J. Halas, “Nanoshell-enabled phothermal cancer therapy: Impending clinical impact”, Acc. Chem. Res., 41, pp. 1842-1451, (2008)
85. P. Cherukuri, E.S. Glazer, and S.A. Curley, ‘Targeted Hyperthermia using metal nanoparticles” Adv. Drug Deliv. Rev., 62, 339, (2010)
86. X. Huang, P.K. Jian, I.H. E-Sayed, and M.A El-Sayed, “Plasmonic photothermal therapy (PPTT) using gold nanoparticles”, Lasers Med. Sci. 22(3), pp. 217-228, (2008)
87. J.A. Copland, M. Eghtedari, V.L. Popov, N. Kotov, N. Mamedova, M. Motamedi, A.A. Oraevsky, “Bioconjugated gold nanoparticles as molecular based contrast agent: Implications for imaging of deep tumours using optoacoustic tomography”, Mol. Imaging Biol. 6(5), pp. 341-349, (2004)
88. Q. Zhang, N. Iwakuma, P. Sharma, B.M. Moudgil, C. Wu, J. McNeill, H. Jiang, and S.R. Grobmyer, “Gold nanoparticles as constrast agents for in vivo tumor imaging with photoacoustic tomography”, Nanotechnology, 20(390, pp. 395102-1-8, (2009)
89. W. Ye, R. Long, H. Huang, and Y. Xiong, “Plasmonic nanostructures in solar energy conversion”, J. Mater. Chem. C. 5, pp. 1008-1021, (2017)

90. J. Li, S.K. Cushing, F. Meng, T.R. Senty, A.D. Bristow, and N. Wu, 'Plasmon-induced resonance energy transfer for solar energy conversion", Nature Photonics 9, pp. 601-607, (2015)
91. S.K. Cushing and W. Wu, "Progress and perspectives of plasmon-enhanced solar energy conversion", J. Phys. Chem. Lett. 7(4), pp. 666-675, (2016)
92. G.L. Liu, J. Kim, Y. Lu, and L.P. Pee,"Optofluidic control using photothermal nanoparticles" Nature Mater.5, pp. 27-32, (2006).
93. J. Donner, G .Baffou, D. McCloskey, and R. Quidant, "Plasmon-assisted optofluidics", ACS Nano 5, pp. 5457–5462 (2011).
94. N.I. Zheludev and E. Plum, "Reconfigurable nanomechanical photonic metamaterials", Nature Nano., 11, pp. 16-22, (2016)
95. X. Fang, M.L. Tseung, J.Y. Qu, K.F. McDonald, D.P. Tsai, and N.I. Zheludev., "Ultrafast all-optical switching via coherent modulation of metamaterial absorption", Appl. Phys. Lett., 104, pp. 141102-1-4, (2014)
96. R. Ulbricht, H. Sakuma, Y. Imade, P.H. Otsuka, m. Tomoda, O. Matsuda, H. Kim, G.W. Park, and O.B. Wright, "Elucidating gigahertz acoustic modulation of extraordinary optical transmission through a two-dimensional array of nano-holes", Appl. Phys. Lett., 110, 091910-1-5, (2017)
97. R. Thijssen, E. Verhagen, T.J. Kippenberg, and A. Polman, "Plasmo nanomechanical coupling for nanoscale transduction", Nano. Lett. 13, pp. 3293-3297, (2013)
98. R. Thijssen, T.J. Kippenberg, A. Polman, and E. Verhagen, "Parallel transduction of nanomechanical motion using plasmonic resonators", ACS Photon. 1, pp. 1181-1188, (2014)
99. R. Thijssen, T.J. Kippenberg, A. Polman, and E. Verhagen, "Plasmomechanical resonators based on dimer nanoantennas", Nano Letter. 15, pp. 3971-3976, (2015)
100. C. Burda and M.A. El-Sayed, "High-density femtosecond transient absorption spectroscopy of semiconductor nanoparticles. A tool to investigate surface quality", PAC, 72(1), pp. 165-177, (2000)
101. O. Matsuda, M.C. Larciprete, R.L. Voti, O.B. Wright, "Fundamentals of picosecond laser ultrasonics", Ultrasonics, 56, pp. 3-20, (2015)
102. J, Margueritat, J. Gonzalo, C.N. Afonso, A. Mlayah, D.B. Murray, and L. Saviot, "Surface plasmons and vibrations of self-assembled silver nanocolumns", Nano. Lett., pp. 2037-2042, (2006)
103. T.A. Keif, Y. Tanaka, O. Matsuda, E.M. Larsson, D.S. Sutherland, and O.B. Wright, "Ultrafast vibrations of gold nanorings", 11(9), pp. 3893-3898, (2011)
104. P. Zhjstram A.L. Tchebotareva, J.W.M. Chon, M. Gu, and M. Orrit, "Acoustic oscillations and elastic moduliof single gold nanorods", Nano Latt., 8(1), pp. 3493-3497, (2008)
105. T.A. Kelf, W. Hosii, P.H. Otsuka, H. Sakuma, I.A. Veres, R.M. Cole, S. Mahajan, J.J. Baumberg, M. Tomoda, O. Matsuda, and O.B. Wright, "Mapping gigahertz vibrations in a plasmonic-phononic crystal", New. J. Phys.,15, 023013, pp. 1-14, (2013)

106. R. Marty, A. Arbouet, C. Girard, A. Mlayah, V. Paillard, V.K. Lin, S.L. Teo, and S. Tripathy, “Damping of the acoustic vibrations of individual gold nanoparticles”, Nano Lett., 11, pp. 3301-3306, (2011)
107. P.K. Jain and M.A. El-Sayed, “Plasmonic coupling in noble metal nanostructures”, Chemical Physics Letters, 487, pp. 153-164, (2010)
108. N.J. Halas, S. Lal, W.S. Chang, S. Link, and P. Nordlander, “Plasmons in strongly coupled metallic nanostructures”, Chem. Rev. 111, pp. 3913- 3961, (2011)
109. D. Wang, A. yang, A.J. Hryn, G.C. Schatz, and T.W. Odom, “Surperlattice plasmons in hierarchical Au nanoparticle arrays”, ACS Photonics, 2, pp. 1789-1794, (2015)
110. L. Aigouy, P. Prieto, A. Vitrey, J. Anguita, A. Cebollada, M.U. Gonzalev, A. Garcia-Martin, J. Labegueirie-Egea, and M. Mortier, “Strong near-field optical localization on an array of gold nanodisks”, J. Appl. Phys., 110, pp. 044308-1-5, (2011)
111. A. Garcia-Etxarri, I. Romero, F.J. Garcier de Abajo, R. Hillenbrand, and J. Aizpurua, “Influence of the tip in near-field imaging of nanoparticle plasmonic modes: weak and strong coupling regimes”, Phy. Rev. B. 79, 125439, pp. 1-5, (2009)
112. F. Keilmann and R. Hillenbrand, “Near-field microscopy by elastic light scattering from a tip”, Phil. Trans. R. Soc. Lond. A,, 362, pp. 787-805, (2004)
113. K.M. Hoogeboom-Pot, J.N. Hermandez-Charpak, Xiaokum Gu, t.D. Frazier, E.H. Anderson, W. Chao, R.W. Falcone, R. Yang, M.M. Murmane, H.C. Kapteyn, and D. Nardi, “A new regime of nanoscale thermal transport: collective diffusion increases dissipation efficiency”, PNAS, 112(16), 4846-4851, (2015)
114. W.S. Chang, F. Wen, D. Chakraborty, M.N. Su, Y. Zhang. B. Shuang, P. Nordlander, J.E. Sader, H.J. Halas, S. Link, “Tuning the acoustic frequency of a gold nanodisk through its adhesion layer”, Nature Comm. 6:7022, pp. 1-8, (2015)
115. Yang, S., Jianhua, Z., Tianran, L., Yuting, Tao., Ruibin, J., Mingxuan, L., Guohui, X., Jinhao, Z., Zhang-Kai, Z., Xuehua, W., Chongjun, J. and Jianfang, W. Plasmonic gold mushroom arrays with refractive index sensing figures of merit approaching the theoretical limit. Nature Communication 4, 2381, (2013)
116. Chen, H., Bhuiya, A.M., Ding, Q. and Toussaint, K.C. Plasmon-Assisted Audio Recording. Sci. Rep. 5, 9125, (2015).
117. Roxworthy, B. J. et al. Reconfigurable nanoantennas using electron-beam manipulation. Nat. Commun. 5, 4427, (2014).
118. B. J. Roxworthy and K. C. Toussaint Jr., “Plasmonic nanotweezers: strong influence of adhesion layer and nanostructure orientation on trapping performance,” Opt. Express 20, 9591–9603 (2012).
119. Rutger Thijssen, Tobias J. Kippenberg, Albert Polman, and Ewold Verhagen, "Plasmomechanical Resonators Based on Dimer Nanoantennas", Nano Letter., 15(6), 3971-3976 (2015)